Rapid expansion of Greenland's low-permeability ice slabs in a warming climate

by

MICHAEL JOHN MACFERRIN

B.S.E., University of Michigan, 2001

M.S., University of Colorado, 2012

A thesis submitted to the University of Colorado at Boulder

in fulfillment of the requirement for the degree of

Doctor of Philosophy

Department of Geography

2018

This thesis entitled:

RAPID EXPANSION OF GREENLAND'S LOW-PERMEABILITY ICE SLABS IN A WARMING CLIMATE

written by Michael John MacFerrin
has been approved for the Department of Geography

_____
Dr. Waleed Abdalati (committee chair)

_____
Dr. Theodore Scambos

Date: _____

The final copy of this thesis has been examined by the signatories, and we find that both the content and the form meet acceptable presentation standards of scholarly work in the above mentioned discipline.

MacFerrin, Michael J. (Ph.D., Geography)

RAPID EXPANSION OF GREENLAND'S LOW-PERMEABILITY ICE SLABS IN A WARMING CLIMATE

Thesis directed by Professor Waleed Abdalati

Recent increases in Greenland's glacial melt have accelerated runoff and become Greenland's dominant mechanism of ice loss. More meltwater is being generated in the ice sheet's lower accumulation zone, which has begun to anneal ice lenses found within the porous firn and form continuous low-permeability ice slabs (LPISs). LPISs are layers of ice meters thick that inhibit water percolating beneath them, extend horizontally for tens of kilometers, and can cause runoff from regions where water previously refroze. LPISs form on decadal timescales and have the potential to quickly increase the extent of Greenland's runoff zone. I present multiple lines of evidence that show LPISs have already increased runoff in recent above-average melt summers, including the record-breaking 2012 summer in Greenland. I use NASA's Operation IceBridge radar to map LPISs across Greenland's ice sheet and peripheral glaciers and show that LPISs already cover approximately 5% of Greenland's total glaciated area. I combine radar observations with regional climate models to show that Greenland's LPISs will likely be 130-850% more extensive by 2100 depending upon 21st century CO_2 emissions scenarios. LPISs under a high emissions future span more than a 250% greater area in 2100 than under moderate emissions, suggesting that ongoing emissions this century play a vital role in controlling melt and determining the size of Greenland's runoff zone.

DEDICATION

This work is dedicated to my children: Thomas, Leslie and Adella.

It has always been important, because of you.

ACKNOWLEDGEMENTS

I have many to thank.

To those who have devoted months of their lives working on the SPLAZ, ACT and FirnCover field campaigns in Greenland, thank you. Five expeditions, nearly 1.5 years of combined prep-work and four more solid months camped on the ice, your devotion and shared vision made it possible: Karen Alley, Dirk van As, Charalampos Charalampidis, Alex Crawford, Liam Colgan, Sam Doyle, Mark Eijkelboom, Leander Gamble, Bastian Gerling, Shane Grigsby, Achim Heilig, Darren Hill, Alun Hubbard, Katrin Lindback, Horst Machguth, Shawn Marshall, Andreas Mikkelsen, Rickard Pettersen, Samira Samimi, Tasha Snow, Aleah Sommers, Max Stevens and Baptiste Vandecrux. Thanks to Kathy Young, Tracy Sheeley, Jessy Jenkins, Susan Zager, Tom Quinn and many others at Polar Field Services who made our countless flights, camps, traverses and stays in Greenland safe and successful. There were more cargo manifests than I can count.

To the NASA Cryospheric Sciences program, for Awards NNX10AR76G and NNX15AC62G, which funded the majority of this work.

To Mahsa Moussavi, our long conversations and late-night laments over coursework got me through the early years of this PhD. Additionally to the long talks with Tasha Snow, Richard Bateman, Jessica Hedge-Balkin and others. The value of your honest companionship cannot be overstated.

To the unbelievable staff at CIRES, handling my countless questions, press releases, interviews, grant proposals, budgets, equipment requests, and field cargo shipments. Lornay Hansen, Katy Human, Sarah McCoy, Ted de Maria, Rob Schubert and many others, you have amplified this journey immensely.

To Glenda Russell and Leslie Blood, your time and investments in my success buoyed me through many struggles and got me across the finish line. The struggles were real, your help was unbelievably important.

To Waleed, you rescued me at a time when I felt ready to give up and leave. You kept with me, and you gave me the freedom to pursue the questions I wanted, which means the world. Your support through it all has been unwavering and invaluable.

An incredible thank you to my mother, Mary MacFerrin. Your help caring for my children when I was a single dad in the office or away in the field made this possible. I could never have done it without you.

Most extraordinarily, to my wife Barbara. You are my rock, my support, my inspiration, the love of my life and the best friend I have ever had. You believed in me even when I didn't. Every day I try to deserve it.

Table of Contents

List of Tables

List of Figures

1 INTRODUCTION

The Greenland Ice Sheet (GrIS) contains approximately 2.85 million gigatons (Gt) of ice, enough to raise sea levels by more than seven meters if it were to disappear entirely (IPCC, 2013; Morlighem et al., 2017). During the 20th century the GrIS lost ~60 Gt of ice per year due to millennial-scale dynamic processes (Kjeldsen et al., 2015). It has since accelerated losses to 280 Gt of ice per year in 2011-14 (McMillan et al., 2016), supplying approximately 25% of the global total annual sea level rise (http://climate.nasa.gov/vital-signs). The GrIS has experienced an increasingly negative mass balance since the early 2000s, with a current annual mass loss of 0.46-0.78 mm of sea-level equivalent (SLE) per year (van den Broeke et al., 2009, Shepherd et al., 2012, McMillan et al., 2016). Prior to approximately 2006, the primary mechanism for mass loss in Greenland was from dynamic losses, with dramatic ice drawdowns from particular outlet glaciers like Jakobshavn Isbræ (Holland, et al., 2008), Helheim (Price, et al., 2011) and Zachariæ Isstrom (Mouginot et al., 2015). Since then, the primary mechanism of Greenland's mass loss has changed, with the majority of annual ice loss now coming from surface mass balance processes, driven primarily by increases in melt and runoff (Van den Broeke et al., 2009, 2016; Fettweis et al., 2013). The year 2012 proved an "extreme" melt year in Greenland with a record single-year loss of 570 Gt (1.59 mm SLE), owing in part to a negative surface mass balance that was three standard deviations below the long-term mean (Tedesco et al., 2013).

The ablation area is the warmest and lowest-elevation "facies", or melt zone, of the GrIS. In the ablation area melt exceeds snow accumulation (Benson, 1962, Figure 1) exposing bare ice annually. A majority of melt from the ablation zone typically runs off the ice sheet, with a small portion of it refreezing on the surface or in cracks (Rennermalm et al., 2013; Smith et al., 2017).

As melt increases in the ablation zone, runoff increases accordingly, and there is little evidence of major feedbacks that would amplify or restrict this melt-runoff coupling in the ablation zone in a warming climate. In the ice sheet's higher-elevation accumulation area, water is partially or wholly refrozen in layers of snow and firn. As melt increases across the accumulation area, it is hypothesized that many of the lower-elevation facies (such as the wet-snow facies) will eventually saturate, transitioning to an ablation area and contributing to runoff (Pfeffer, et al., 1991; Braithwaite, et al., 1994), which would increase the size of Greenland's runoff zone. The speed and mechanisms of the accumulation zone transitioning to runoff is poorly understood at this time. Since the accumulation zone comprises approximately 80% of the modern GrIS (Benson, 1962; Box et al., 2006), knowing the speed at which the accumulation zone can transition to ablation is key to predicting Greenland's future contributions to sea level in a warming world. How fast can the runoff zone expand?

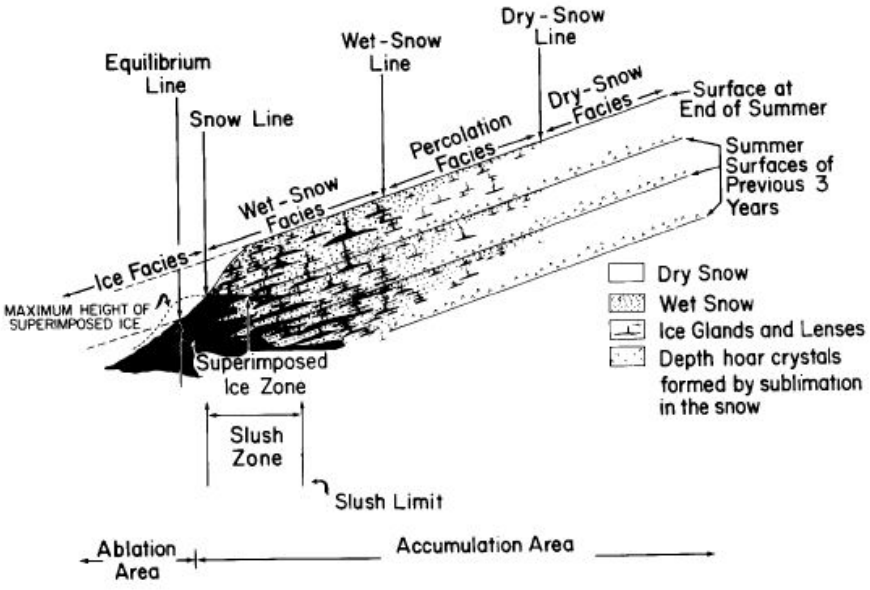

Figure 1 | The facies of an ice sheet (Benson, 1962).

In this work I present evidence to support and quantify a rapid feedback process by which Greenland's accumulation facies can transition to an ablation zone quickly, on the scale of a decade, and rapidly expand the size of Greenland's runoff zone. The specific questions being addressed are outlined herein.

1.1 Dissertation Structure

The primary goal of this dissertation is to identify and investigate a feedback happening in Greenland's accumulation zone in which melt has increased runoff from high elevation regions of the ice sheet. This melt-runoff feedback, explained in detail throughout this text, has the possibility to rapidly expand the size of Greenland's runoff zone faster than has been previously hypothesized. If expanding the size of the runoff zone results in more total runoff, this feedback has potentially large implications for the present and future mass balance of the ice sheet.

The remainder of **Chapter 1** outlines the state of literature and past work in Greenland's surface mass balance and sets the context for my contributions to the field. Original authors and manuscript references are noted in the captions accompanying each figure in this chapter.

Chapter 2 investigates the question *"Is refrozen meltwater in Greenland's accumulation zone capable of forming impermeable perched layers over porous firn that can enhance runoff?"* Previous work hypothesized this to be unlikely (Harper et al., 2012; Humphrey et al., 2012; Pfeffer & Humphrey, 1998), but I present new evidence to show that it is possible and is already happening. Field observations, remote sensing and modeling show how increasing melt water in cold polar firn can anneal ice layers to form thick low-permeability ice "slabs" (LPISs). LPISs

enhance runoff in high-elevation areas of the ice sheet where runoff has not previously been observed. I outline the process by which they form, illustrate how quickly runoff can occur above them, and how they have already begun to enhance runoff in southwest Greenland in today's warming climate.

Chapter 3 investigates the question *"What is the extent of the Greenland ice sheet that has already been affected by low-permeability ice slabs?"* I use cores and *in situ* ground-penetrating radar (GPR) from a field campaign to identify LPISs in southwest Greenland, and link them with coincident airborne radar from NASA's Operation IceBridge (OIB). I develop an automated workflow to identify LPISs in OIB radar, and use ground measurements to determine necessary cutoffs and thresholds used in processing. The map of LPISs produced by this work are the first wide-area map of buried ice slabs in firn over any large glaciated region on Earth.

Chapter 4 investigates two related questions: *"What are the key climate variables which have formed LPISs in Greenland?"* and using the variables identified, *"What are the expected future extent of LPISs on the Greenland ice sheet?"* Building upon previous work (Pfeffer et al., 1991) I use regional climate models (RCMs) to quantify the melt and accumulation conditions under which LPISs have formed in Greenland. I create a calculation of "excess melt" based upon this relationship to generate maps of current LPIS extent across the entire Greenland ice sheet and peripheral ice caps. These maps help fill coverage gaps where present-day LPIS extent is missed by observational gaps in OIB radar returns. I use the same RCMs to predict the extent of LPISs into the future under different climate scenarios, and quantify how present and future emissions scenarios determine the future extent of Greenland's runoff zone.

Chapter 5 summarizes the scope of work within this dissertation and its importance for assessing and predicting runoff from the Greenland ice sheet. It also discusses several future research directions this work could take, to help guide future efforts on the topic.

1.2 Studies of Greenland's Facies and Firn Structure

1.2.1 Defining and Mapping Greenland's Facies

The GrIS is classically separated into distinct snow and ice facies, ranging from bare ice at low elevations, wet snow and percolation zones at mid-elevations, to dry snow at high elevations where no melt occurs, illustrated in **Figure 1** above (Benson, 1962).

After the 1951 US-Danish "Defense of Greenland" treaty, the North American Treaty Organization (NATO), the US Army Corps of Engineers (USACE) and the Cold Regions Research and Engineering Laboratory (CRREL) established an extensive research program on the GrIS. As part of this effort, the Benson traverse spent four years mapping the facies of the Greenland ice sheet (Benson, 1962). Using snow pits, firn cores and penetrometers, they classified and created the first maps of the stratigraphy of the Greenland ice sheet (**Figure 2**), although large uncertainties existed in southeast Greenland.

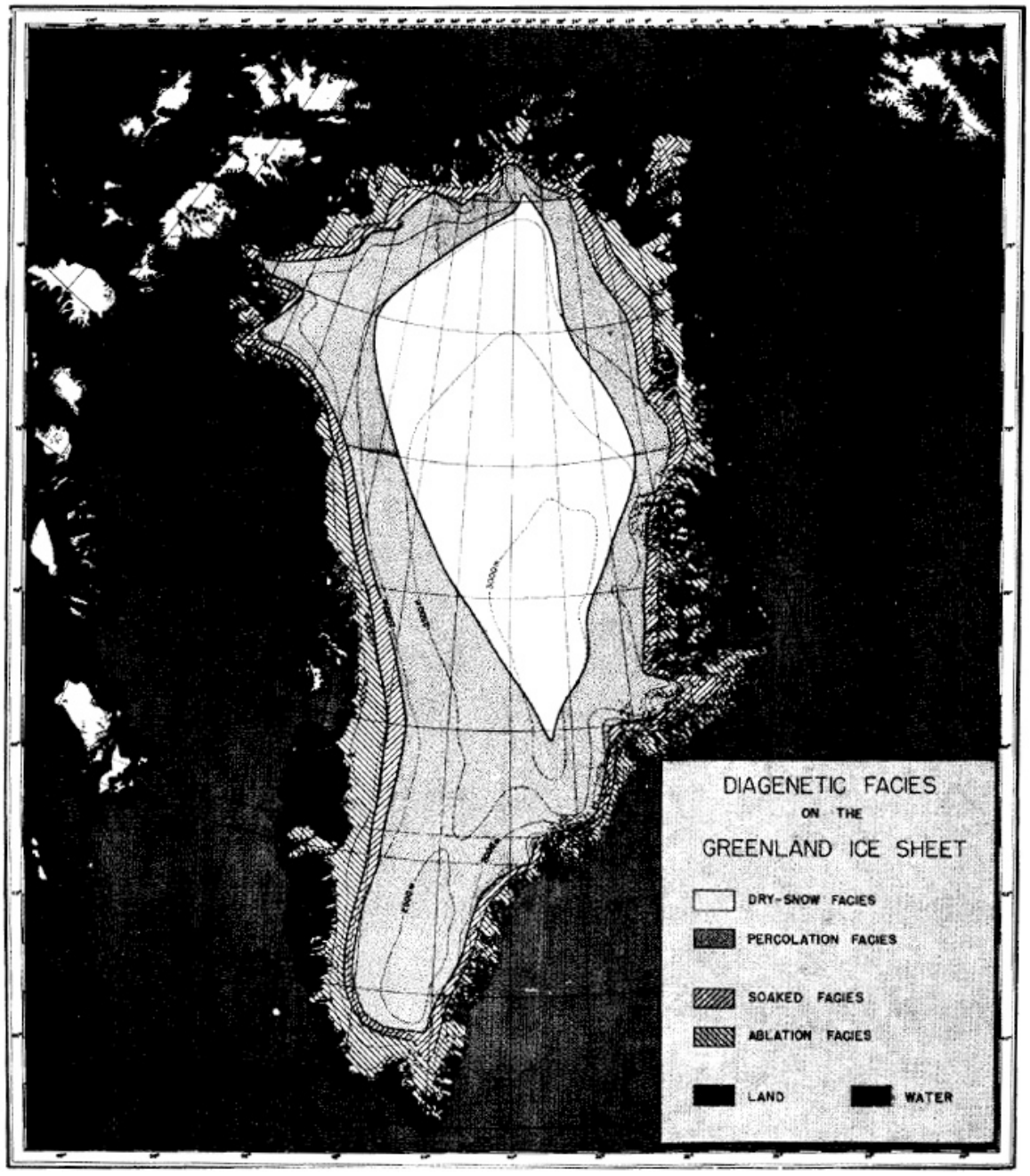

Figure 2 | Distribution of facies on the Greenland ice sheet (Benson, 1962).

Other groups performed extensive classification of the facies of glaciers and ice sheets during and preceding those times (e.g. Müller, 1962), but had not mapped these out across the entire extent of Greenland.

A central piece of this work was the delineation of the melt facies of the Greenland ice sheet. The highest of these zones, the "dry snow facies," are dominated by dry snow, where little to no melt occurs on annual timescales (**Figure 1**). The near-surface firn in the dry snow zone contains small, highly-faceted grains which slowly become rounded by ablation and vapor deposition as they age (Cuffey & Paterson, 2010). The "percolation facies" refer to areas where melt occurs regularly in small amounts and penetrates minimally before refreezing. The percolation facies contain a mix of dry firn and wetted refrozen firn where water has percolated, causing larger, rounded grains. Small ice lenses exist where water refreezes, scattered heterogeneously throughout the firn column. The "wet-snow facies" refer to the zone where meltwater is generated in enough quantity to percolate through the seasonal snow layer before refreezing, causing most or all of the firn to have larger grains which have been wetted and rounded. Ice lenses are typically thicker and more crowded in these facies. Below the wet snow zone is a typically-narrow facies referred to as the "superimposed ice zone," in which the pore-space of the snow and firn is overwhelmed by meltwater on an annual basis. Some melt water escapes the superimposed ice zone while some slush refreezes atop the surface, thus causing annual accumulation. The upper-limit of the superimposed ice zone is the runoff line, the highest extent to which liquid water leaves the ice sheet. Below the superimposed ice zone is the ablation zone, the area where annual melt exceeds accumulation, little or no firn is accumulated, and bare ice is exposed annually. The wet snow and superimposed ice zones define the transition between the runoff zone where some water is lost and the higher accumulation zone where 100% of melt water is refrozen and retained. Areas transitioning from wet snow to superimposed ice define the

migration of the runoff line in Greenland. The wet snow and superimposed ice zones are the primary focus of this dissertation.

Inter-annual variability is significant in all of these zones. On an annual basis the exact boundary between the zones may vary uphill or downhill substantially, causing a location on the ice sheet to be in the percolation or wet-snow zone one year and below the equilibrium line in another. The boundaries between these lines are typically defined on a long-term basis, by analyzing pits and firn cores to depth, studying the dominant stratigraphy of the firn column at a given location over time. In today's changing climate it can be difficult to discern where these zones, which are now moving, are located in a given year, and often regional climate modeling is used to make these distinctions.

In the 1990's, NASA's Program for Regional Climate Assessment (PARCA) (Steffen & Box, 2001; Thomas, 2001) was initiated to provide key details necessary to determine the total mass balance of the Greenland ice sheet. Among these goals was a more detailed and extensive study of Greenland's facies in the accumulation zone. The PARCA program drilled a series of firn cores around an approximate 2000-meter elevation contour of the Greenland ice sheet (**Figure 3**) to measure firn density and stratigraphy, as well as ice velocity, annual accumulation rates, compaction rates and other key variables to assist in constraining Greenland's overall mass balance (e.g. Mosley-Thompson et al., 2001). The PARCA cores are used extensively to this day in glaciological studies, including some of the work outlined in this dissertation.

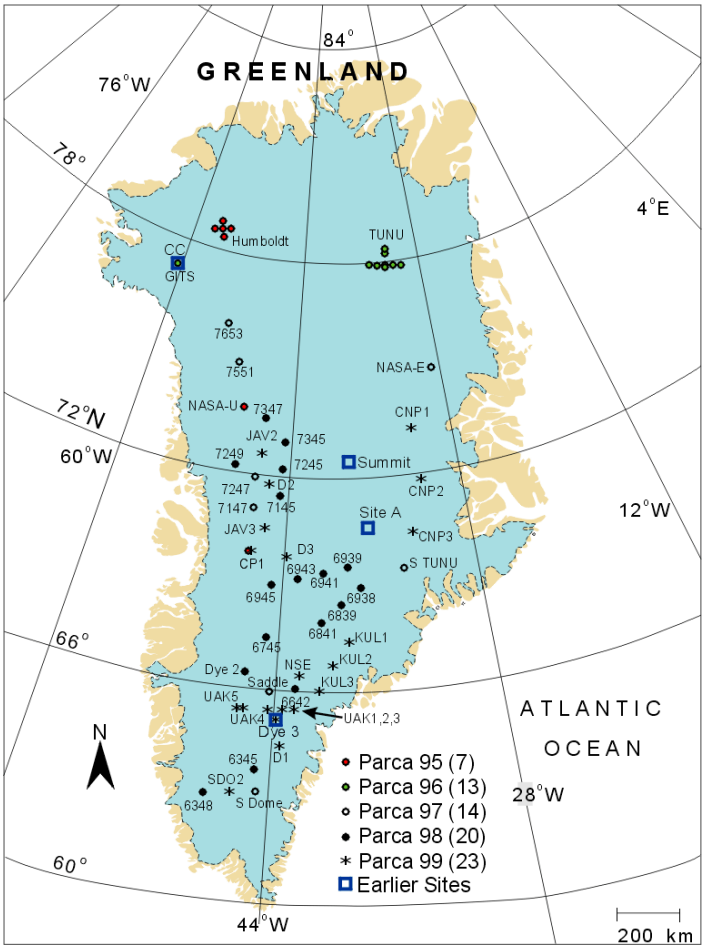

Figure 3 | PARCA core sites (from http://research.bpcrc.osu.edu/Icecore/Greenland.html)

As polar climate warms, university-led studies have documented how the facies in Greenland and other polar glaciers and ice caps are beginning to respond to greater melt. On a series of repeat field seasons spanning 2004 through 2012, a team of Canadian researchers used coincident repeat cores on the Devon Ice Cap (Nunavut, Canada) to document meter thick ice layers that had formed in the top several meters of firn (Bezeau et al., 2013). The layers were significantly thicker and more prevalent in the later campaigns (2010-12) than they were in earlier campaigns (2004-07) at every coring site. The increasing ice content across the entire study area represented significant changes in stratigraphic regimes of the snow and firn during

the intervening years at all elevations of the ice cap. They hypothesized that in the future, such layers may cause runoff if such layers continued to grow.

1.2.2 Ground-Penetrating Radar Surveys

GPR has given ground-based researchers a non-invasive tool to map stratigraphy in polar ice sheets. Radar signals traveling through firn and ice reflect off sharp dielectric gradients, such as ice, snow, air and/or water transitions (Jol, 2008), making them particularly useful for mapping subsurface features in polar snow and firn. To properly convert two-way signal travel times into appropriate depths within snow and firn, Kou et al., (1993) and Kovacs et al. (1993, 1995) performed a series of experiments to empirically calculate the dielectric constant of firn. The time-depth conversion of radar signals through snow, firn and ice is a complicated and oft-revisited task that depends not only upon the physical properties of the substrate but also the design, engineering and operating frequencies of the instrument. Despite these challenges, GPR has been a vital tool for mapping stratigraphic boundaries within the Greenland ice sheet. For instance, Brown et al. (2011) used *in situ* GPR and firn cores to map the spatial heterogeneity of stratigraphic layers within firn over different spatial scales. MacGregor et al. (2015) used airborne GPR and deep ice cores to map the age and radio-stratigraphy of the entire Greenland ice sheet, finding much more ice from the Eemian Period (~130,000 yr b.p.) than was previously believed to exist at Greenland's bed.

On the Canadian Arctic's Devon Ice Cap, researchers used cores and a continuous 40 kilometer uphill GPR transect to document the formation of extensive ice layers in Devon's near-shallow firn (Gascon et al., 2013). The work hypothesized that these layers had the potential to block

percolation in the lower accumulation zone of the ice cap, possibly raising the runoff line atop these layers in future years. In Western Greenland, researchers found ice lenses that caused bright continuous reflections for several hundred kilometers using the Snow Radar data aboard an Operation IceBridge flight line in 2011 (de la Peña et al., 2015). Several cores indicated these layers to be 30-60 cm thick, although OIB's Snow Radar lacked adequate penetration to infer their thickness from the radar signal directly. At the time, the layers were concluded to have likely formed in the previous high-intensity 2010 melt year in Greenland (de la Peña et al., 2015). The research hypothesized that these layers may be capable of blocking percolation and causing runoff, but no such relationship was shown at the time of the study.

1.2.3 Firn Aquifers

In the Spring of 2011, Rick Forster and colleagues were drilling a firn core in the Helheim Glacier drainage of Southeast Greenland (Forster et al., 2014). Although summer melt regularly occurs in the area, Spring temperatures averaged approximately -20 °C and no Spring melt had yet occurred, leading the researchers to assume they were drilling "dry" refrozen firn cores. In one borehole, the drill emerged dripping with liquid water, coming from a saturated firn layer below (at approximately 12 meters' depth). Later analysis of GPR data found that the researchers had drilled into a "perennial firn aquifer" on the ice sheet, capable of storing meltwater throughout the year without freezing. Analysis of *in situ* GPR data found that these layers formed distinct bright reflectors in the firn column which completely attenuated nearly all signal beneath them. (Due to its extremely high index of refraction, liquid water tends to attenuate GPR signals far more strongly than dry firn or ice.) The researchers used *in situ* GPR and OIB's mid-frequency Accumulation Radar to map the presence of these aquifers across the Greenland ice

sheet, creating the first extensive GPR-derived map of a subsurface firn process across an entire ice sheet (**Figure 4**, Miège et al., 2016). Combining these maps with a firn model determined that high rates of melt coupled with high annual snow accumulation caused these aquifers to form in the places where they are now known to exist (Munneke et al., 2014).

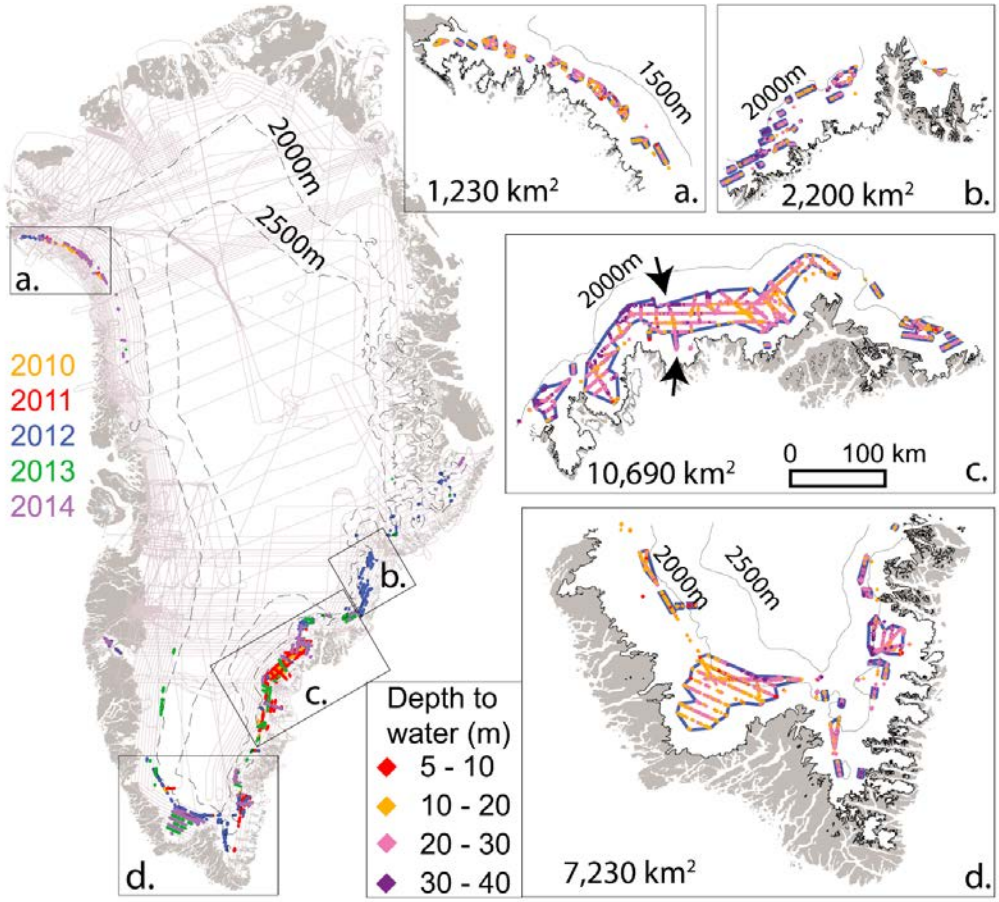

Figure 4 | Perennial firn aquifers on the Greenland ice sheet, mapped by Operation IceBridge (Miège et al., 2016).

Munneke et al. (2014) modeled the formation of aquifers with a high-resolution multi-layered firn model to determine the conditions under which they form. They found that a combination of two primary conditions must be met to form a perennial firn aquifer where water is stored in

liquid form throughout a winter season. First, the annual air temperature and seasonal air temperature magnitude must be high enough to produce enough summer melt to overwhelm the firn's capacity to refreezing it. Second, the annual snow accumulation rate must be high enough to insulate percolated water from the winter cold, which would otherwise cause refreezing. Their work found that an annual air temperature greater than approximately -17 °C, combined with a seasonal temperature swing great enough to cause significant summer melt, would allow aquifers to form if the annual snow accumulation rate is more than 500-1000 mm water-equivalent per year, with the exact accumulation threshold depending upon the annual temperature (Munneke et al., 2014). To summarize, in regions warm enough to have significant summer melt that are also buried by snow deep enough to insulate it through the winter, water is retained in perennial aquifers in the firn rather than refreezing.

1.3 Firn Permeability, Saturation and Runoff

1.3.1 Saturation Ratios

The primary distinctions between the ablation zone of a glacier and the accumulation zone is the ratio between snow accumulation and melt. In warm areas where melt exceeds snowfall in a given year, water is forced to run off from the area of melt, usually over bare ice. In regions where little meltwater is generated, the underlying snow and firn is able to absorb the melt, which typically refreezes and does not run off from the ice sheet. The runoff line defines the upper limit of where some amount of mass is lost to runoff in an average melt year. The runoff line is also the upper extent of the superimposed ice zone, where seasonal snow is routinely saturated completely and accumulation consists of refrozen slush with little or any pore space. In

superimposed ice regions, some mass can accumulate annually as slush refreezes on top of the ice, even though water is lost to runoff (Figure 1).

Pfeffer et al. (1991) calculated an envelope for the possible upward migration of the runoff line in Greenland under a warming climate. They proposed two modeling studies, one in which any meltwater generated on the surface would fill all firn pore space before running off to sea, and another in which an "impermeable horizon" quickly formed at runoff was allowed to flow almost immediately out to sea. These two models were dubbed the "Maximum Time Fill-In Model" and the "Minimum Time Fill-In Model," respectively. Both models were run across the Greenland ice sheet against six forcing scenarios simulating different levels of warming (3-5 °C) and different changes in accumulation (0-15%) over a 100-year time span (Figure 5). Both models predicted that the runoff line would migrate uphill, with the Minimum Time Fill-In Model's runoff lines rising faster (Figure 6). The results of this study and the work within this thesis that builds upon it are discussed at greater length in Chapter 4.

Climate Model	ΔT, °C	$\Delta c/c$	Variation From Standard Model
S	4	0.10	
I	3	0.10	1°C cooler
II	5	0.10	1°C warmer
III	4	0.15	50% wetter
IV	4	0.5	50% drier
V	4	0.0	no change in accumulation from present

Figure 5 | Experiment descriptions from Pfeffer et al. (1991)

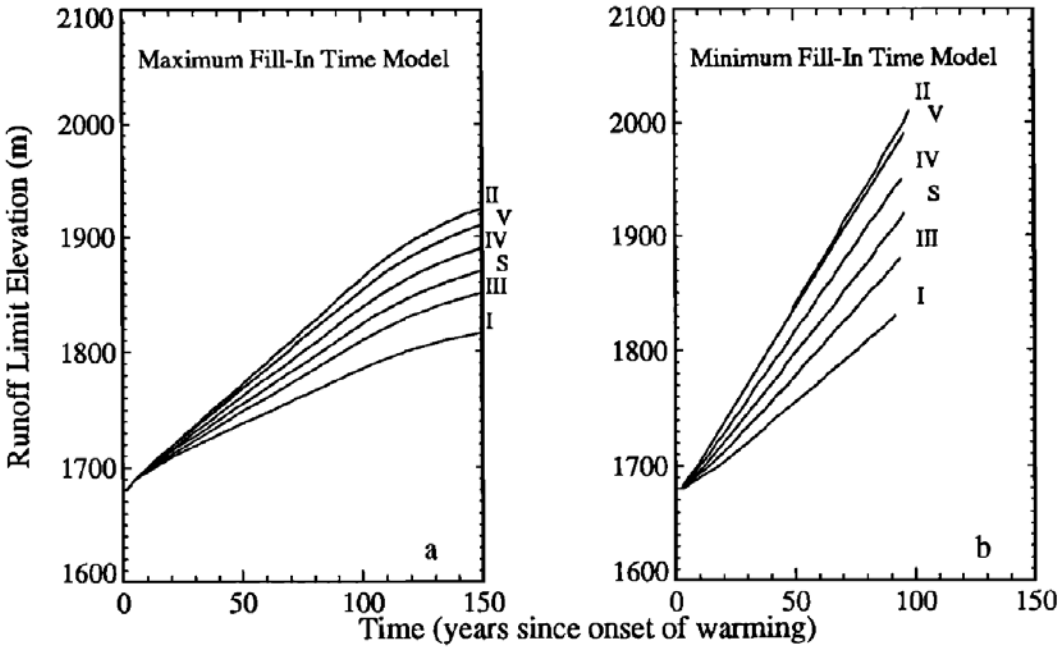

Figure 6 | Upward migration of runoff line, model results (image from Pfeffer et al., 1991)

To assess when a particular elevation of the ice sheet would begin running off, Pfeffer et al. calculated a "runoff threshold," the amount of meltwater that would cause pore space to fill and water to eventually pool at the surface. The relationship is based upon the density of snow and ice and the cold content present in the snow which is available to contribute to refreezing, outlined in (1:

$$M \geq \frac{\mathbb{c}}{L} C \cdot T_f + (C - M)\left(\frac{\rho_r - \rho_c}{\rho_c}\right) \quad (1)$$

M = annual melt
C = annual accumulation
$\mathbb{c}$ = heat capacity of ice
L = latent heat of fusion for ice
T_f = initial firn temperature
ρ_{pc} = pore close-off density (.830 g cm^{-3})
ρ_c = initial snow/firn density

This equation can be refactored in terms of a melt-to-accumulation ratio ((2):

$$\frac{M}{C} \geq \left[\frac{c}{L} T_f + \frac{\rho_{pc} - \rho_c}{\rho_c}\right]\left[1 + \left(\frac{\rho_{pc} - \rho_c}{\rho_c}\right)\right]^{-1}. \quad (2)$$

The M/C ratio defined a threshold of melt to accumulation, above which runoff would inevitably occur. They found this ratio to be approximately 0.697 for the majority of the ice sheet, and noted that *"this number turns out to be quite insensitive to reasonable variations in T_f and ρ_c, and for a wide variety of firn conditions, the necessary conditions for runoff can simply be stated as*

$$\frac{M}{C} \approx 0.7 \quad " \quad (3)$$

(Pfeffer et al., 1991). The mechanisms by which underlying firn would saturate and the timing at which runoff could occur after this threshold is crossed were still open questions.

Roger Braithwaite performed similar calculations when exploring snow and firn densities in the lower accumulation zone of Greenland, reaching a final value of 0.58 for the same ratio, using a different formulation (Braithwaite et al., 1994). The final numbers differ in each formulation, but provide a simple way to determine a threshold in which an area of Greenland's accumulation zone may begin running off. This relationship proves important now that the polar regions are rapidly warming (IPCC, 2013) and melt is increasing across Greenland (Van den Broeke et al., 2016). Their theoretical predictive experiments have turned into a contemporary reality.

1.3.2 Firn Buffering Capacity

The threshold at which a patch of snow and firn will begin saturating has been calculated with a high degree of confidence, but the timing of runoff is largely dependent on the speed at which the "sponge" of underlying snow and firn can saturate. Recent work hypothesized that even in a warming climate with increased melt, Greenland's percolation and dry snow facies contain considerable pore space which may buffer melt water and delay additional runoff to the sea up to several decades (Harper, et al., 2012). Melt extent has increased across the Greenland ice sheet by ~16,800 km^2 a^{-1} in the period 1979-2011 (Box et al., 2011), with a record melt event in 2012 that covered nearly the entire ice sheet (Nghiem et al., 2012). Recent trends suggest that this pattern is likely to continue, and the entire surface of the GrIS will likely experience regular melt within the next several decades (McGrath, et al., 2013). Supraglacial melt lakes have been observed to form progressively higher on the ice sheet's surface (Liang et al., 2012, Howat, et al., 2013), indicating that surface water is failing to percolate at higher elevations, and is instead pooling on the surface where such lakes have not previously been observed. Subsurface ice layers caused by increase melt and refreezing have been observed in Arctic glaciers and ice caps such as the Devon ice cap in the Canadian Arctic (Bezeau et al., 2013) and Greenland (Brown et al., 2011). Although previous studies have hypothesized that such layers may contribute to lateral runoff from the ice (e.g. Gascon et al., 2013), such a relationship had not yet been conclusively shown. Understanding the exact nature and behavior of refrozen subsurface ice in a transient warming climate is vital to predicting future projections of runoff, mass loss, and global sea level rise.

1.4 Firn Compaction

A primary uncertainty in the calculations of firn's capacity to absorb meltwater is the density of snow and firn. As snow accumulates in the upper regions of an ice sheet, it is buried by subsequent layers of snow and compressed over time, eventually becoming polycrystalline glacial ice (Cuffey & Paterson, 2010). This process is known as "firn compaction." The rate of firn compaction has been important for numerous glaciological problems such as determining the age of air bubbles in ice cores. Firn compaction has proven crucial for construction and maintenance of on-ice structures on the Greenland ice sheet, and was a primary contributor to the unviability and eventual condemnation of Cold War military installations in Greenland (Kovacs, 1970). Changes in firn compaction rates are among the largest uncertainties in altimetry-based mass balance assessments of Greenland. Studies have focused on firn compaction in Greenland for nearly a century, and the topic has seen a resurgent interest in the context of Greenland's changing climate.

1.4.1 Sorge's Law

During a series of 1929-31 field campaigns performed at Eismitte, Greenland, Ernst Sorge deduced that—in glacial regions of dry snow and relatively stable climate—one can determine the velocity of densification of a layer with a depth-density profile (as acquired from a firn core) and a knowledge of the annual accumulation rate at a given site (Sorge, 1935). By computing the annual rate at which each layer compacts as it advects deeper into the firn column, Sorge found that the layer of snow found at a given depth would stay constant over time. For example, if firn at 50 meters' depth were 145 years old in one year at a given location, firn at 50 m depth at that location would remain ~145 years old in any future date. Sorge later applied this theory to

calculate the approximate accumulation rate in firn layers in places where individual layers were difficult to determine (Sorge, 1938). At a later date, Henri Bader generalized the finite increment methodology employed by Sorge into a mathematical function known as “Sorge’s Law” (Bader, 1954). Sorge and Bader’s work were among the first to mathematically calculate the vertical compaction of firn and snow on a glacier or ice sheet. Their basic methods are still applicable and used to this day.

1.4.2 Coffee Can Measurements

Annual accumulation rates, initial snow density, mean annual temperature, and melt rates are poorly constrained by a lack of observations over many parts of the Greenland ice sheet. It is difficult to apply Sorge’s Law to compute contemporary firn compaction rates across the entire Greenland ice sheet in a given year. Even if these were previously known everywhere, changes in Greenland’s climate (such as those caused by anthropogenic climate warming) invalidate the steady-state assumptions used by Sorge and Bader to deduce steady-state compaction rates from density profiles alone. A simple mathematical model for dry-snow compaction cannot currently serve the needs of the Greenland mass balance community. Research using direct measurements is vital to understanding compaction rates in Greenland.

As part of NASA’s PARCA program in the 1990s, Hamilton and Whillans (2000) used stiff rods placed down boreholes in Greenland’s firn to measure contemporary annual rates of firn compaction. They drilled a borehole and placed a stiff rod down the length of the borehole, marking the distance of the snow surface along the pole at that point in time. They covered the

borehole and upon repeat visits, measured the distance the previous surface has fallen in the intervening year to derive the annual compaction rate of firn at that location.

Combining firn compaction measurements with accumulation, elevation and ice flow, they could quantify the total specific mass balance at selected locations on the ice sheet. These borehole measurements were named “coffee can” measurements, which has become an umbrella term for *in situ* compaction measurements taken over firn boreholes on a glacier or ice sheet. Rates of compaction were measured on annual timescales upon repeat visits to each site. Their results found that the ice sheets thinned at two points in the West and Northwest (Crawford Point and Camp Century, respectively), was nearly in balance at another Western coastal site inland from the village of Upernavik, but thickened slightly at both Summit Camp (North-central Greenland) and Dye-2 (Southwest) (**Figure 7**).

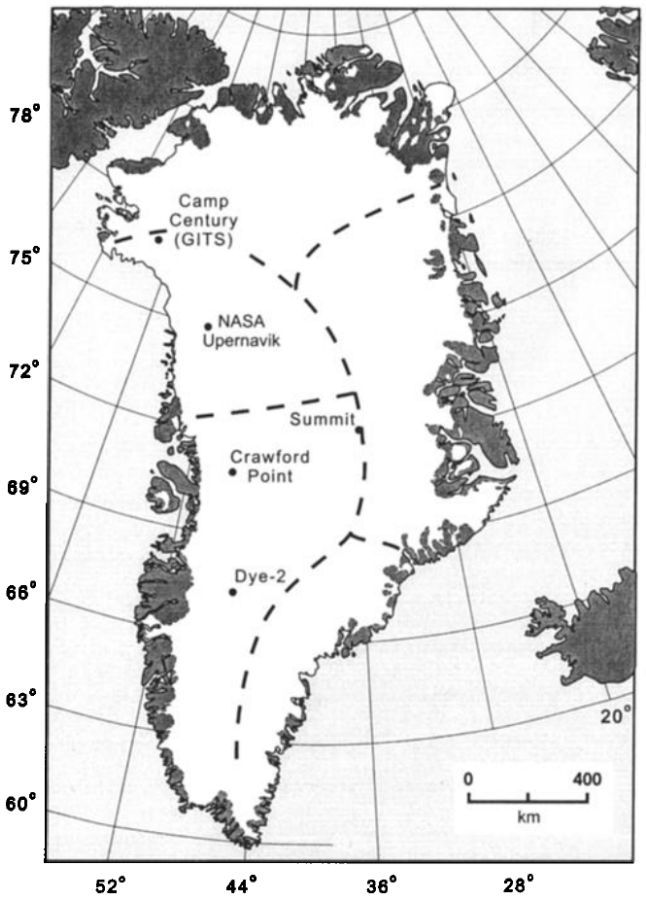

Figure 7 | Coffee can point mass balance measurements (Hamilton & Whillans, 2000).

Arthern et al. (2010) later performed similar compaction measurements using strain meters to measure continuously at several sites in West Antarctica. The stations measured compaction hourly and transmitted results daily over an Iridium satellite phone connection. Their results were among the first real-time compaction measurements taken in Antarctica, and differed somewhat from what other compaction models predicted (for the measured temperatures and accumulation rates at each site). They found rates of compaction to be higher than what other models predicted, and thus created their own empirically-driven model based on their measurements.

1.4.3 Vertical Compaction Models

Herron & Langway (1980) compared core density profiles and annual accumulation rates at 17 locations in both Greenland and Antarctica, and derived an empirical model for steady-state rates of compaction in dry snow. They found a linear relationship exists between snow/firn depth and a log-function of density

$$ln[\rho/(\rho_i - \rho)] \quad (4)$$

where ρ is the density of firn at a given depth and ρ_i is the density of pure ice, consistent with Sorge's law. They found the slope of this linear relationship depended primarily on mean annual temperature and accumulation rate at a given location. They also found that density profiles and compaction rates have a distinct cutoff at a density of ~550 kg m^{-3}, in which compaction is faster at shallow depths until hitting this cutoff density, but slows down at deeper depths with higher densities. Two sets of slope constants (one for density <550 kg m^{-3}, the other for ≥550 kg m^{-3}) were derived from empirical fits to the depth/density profiles seen in cores at each study location. Herron and Langway's (1980) work remains the basis for the majority of compaction modeling today. However, as melt water increases across Greenland, the steady-state assumptions used by Herron and Langway and their predecessors are being challenged. In addition to changing temperatures and accumulation rates, changes in melt water formation are altering the physical structure and temperature of the firn in ways that make vertical compaction models more and more difficult to use. Coupled regional climate models (with working ice, snow and atmospheric boundaries) are being used more and more to simulate the density and stratigraphy of Greenland's firn layer.

1.4.4 Regional Climate Models

Vertical firn models do well simulating firn density in dry-snow regions of the ice in a constant climate. However, given that meltwater percolation in Greenland's firn affects an increasingly large segment of the ice sheet (Machguth et al., 2016; Mikkelsen et al., 2016; de la Peña et al., 2015; Fitzpatrick et al., 2014), punctuated by increasingly common record-breaking summer melt events (McGrath et al., 2013; Nghiem et al., 2012; Tedesco et al., 2013), it is important to note that meltwater routing is not an entirely one-dimensional process. The exact nature and extent of horizontal water flow both within the firn (Brown et al., 2011; Humphrey et al., 2012; W. T. Pfeffer & Humphrey, 1998) and water routing on the surface atop low-permeability ice layers in the shallow firn (Machguth et al., 2016; Mikkelsen et al., 2016) is still being studied (including the work in this dissertation), but the existence of these processes directly imply that modeling the evolution of firn layers across the entire Greenland ice sheet requires a spatially-coupled model approach where water can route between adjacent pixels over wide areas.

Regional Climate Models (RCMs) that simulate the atmospheric inputs to surface mass balance (SMB) (snow, sunlight, melt and evaporation, e.g.), use a multi-layered approach to simulate firn densification and absorption, and utilize fully-coupled energy transfer models between them, are uniquely well-suited to perform this work. The surface mass balance components in all SMB models are based upon the surface mass balance equation for ice sheets and glaciers:

$$\dot{b_s} = \dot{a}_s + \dot{a}_r - \dot{m}_s + \dot{a_r} - \dot{s} + \dot{a_w} \quad (5)$$

$\dot{b_s}$ = surface mass balance
$\dot{a}_s$ = snow accumulation
$\dot{a}_r$ = rain deposition
$\dot{m}_s$ = melt
$\dot{a_r}$ = refreezing
$\dot{s}$ = sublimation
$\dot{a_w}$ = accumulation by wind deposition

with all values defined in mass per unit area (Cuffey & Paterson, 2010). Some formulations also include a term for avalanche deposition, which is irrelevant in the interior of ice sheets and is ignored here. SMB models typically use an atmospheric model to generate the snow, rain and wind components of the equation, coupled with a surface-energy model to calculate melt and sublimation. These are coupled to a multi-layer firn model which calculates refreezing and runoff (the residual between melt, sublimation and refreezing). On polar ice sheets, the dominant factors in SMB are typically snow accumulation, melt and refreezing. Rain, sublimation and wind deposition play more minor roles, although in some areas of Greenland rain is becoming a growing factor as the melt season increases (Doyle et al., 2015).

Box et al. (2006) used the PolarMM5 model which incorporates an NCAR mesoscale atmospheric model modified for use in the polar regions with a firn model to simulate the evolution of Greenland's firn in a changing climate. They found that in 2006, both melt rates and accumulation rates increased across Greenland, leading to a negligible decrease in Greenland's overall surface mass balance. The Modèle Atmosphérique Régional (MAR) (Fettweis et al., 2013) couples the multi-layered Crocus snow model (Vionnet et al., 2012) to simulate Greenland's firn. Among numerous other studies, MAR was used to determine the overall severity of runoff in Greenland's record-breaking 2012 melt summer (Tedesco et al., 2013). One

of the more popular RCMs used in glaciological circles today is the "Regional Climate Model" (RACMO), which uses High Resolution Limited Area weather forecasting Model (HIRLAM) (Undén, Rontu, Järvinen, Lynch, & Calvo, 2002) coupled with the European Center for Medium-range Weather Forecast (ECMWF) model (Dee et al., 2011) and an in-house multilayer Firn Densification Model (FDM) (Ligtenberg et al., 2011) to simulate firn processes. The HIRHAM5 model (Christensen et al., 2007) built and distributed by the Danish Meteorological Institute uses a tuned combination of the HIRLAM (Undén et al., 2002) and ECHAM (Roeckner et al., 2003) models to simulate surface mass balance and firn processes in Greenland. The Polar Portal (http://www.PolarPortal.org) uses HIRHAM5 outputs to simulate daily surface mass balance of the GrIS, and the model is lately becoming increasingly well known for accurately simulating meltwater processes across Greenland, fitting well with a wide range of observations (Langen et al., 2017). Each of these models are large multi-institution efforts run on supercomputers to best simulate the surface mass balance of the Greenland and Antarctic ice sheets in a changing climate.

Many of the processes simulated by RCMs can suffer from resolution issues. Millimeter- and meter-scale firn processes cannot be accurately resolved directly by the models' physics run on 5-20 km grids, and therefore must be parameterized and validated based on very limited observational datasets. A one-dimensional energy and surface mass balance models built at the Geological Survey of Denmark and Greenland (GEUS) is actively forced with observational datasets to simulate surface mass balance very accurately in regions with a time series of weather observations (van As et al., 2017, e.g.), but has yet to be applied in regions where observations are sparse or non-existent. The general lack of real-time observational data sets against which

RCM firn models can be forced or validated remains an open problem within the modeling community.

2 ON THE FORMATION OF LOW-PERMEABILITY ICE SLABS IN GREENLAND'S LOWER ACCUMULATION ZONE

2.1 Introduction

As melt percolates into cold polar firn, it refreezes to form ice lenses. Cycles of melt and refreezing create a stratified firn layer in the wet snow and percolation facies of a glacier (Benson, 1962). The concept of a "perched impermeable layer" is used to describe the possibility that a horizon of meltwater can penetrate homogeneously from the surface and refreeze into an impermeable layer. Further meltwater would be forced to propagate horizontally over this layer rather than propagating vertically into the firn (Pfeffer & Humphrey, 1996, 1998). It was found that over large spatial scales (decameters to kilometers) refreezing was vertically heterogeneous in polar firn. Water often uses preferential flow paths ("pipes") to penetrate to various depths within the firn before hitting a hydrologic permeability barrier and refreezing (Brown et al., 2011). These preferential flow paths can help water temporarily circumvent the cold content of immediately-surrounding firn and percolate to great depths, at times more than 10 meters before refreezing (Humphrey et al., 2012). Because of this great penetration depth, it was argued that even in the presence of increased meltwater from warming temperatures, water could fill much (or all) available firn pore space before it would escape and run off horizontally toward the ice margins (Harper et al., 2012). Firn would act as a "buffer" for meltwater for decades, partially delaying the increase of meltwater reaching the sea.

Recent evidence from in Arctic Canada shows that large volumes of ice have begun to accumulate within the shallow firn along a transect near the summit of the Devon Ice Cap, seen in cores (Gascon et al., 2013) and ground-penetrating radar (GPR) (Bezeau et al., 2013). It was

hypothesized that if these ice layers were continuous enough, they may be capable of blocking percolation and causing runoff from the high elevations of the Devon ice cap. However, no runoff these ice layers had been observed yet during the study period. Whether they would actually impact runoff was yet unclear.

This chapter describes the discovery of Low-Permeability Ice Slabs (LPISs) in Greenland, and seeks to answer the question of whether or not LPISs can cause runoff from the long-term accumulation zone on short time spans, before meltwater has filled all available pore space.

2.2 Study Area

The Kangerlussuaq Transect ("K-Transect") defines a line of automated weather stations, GPS locations, and mass balance stakes along the central flow line of the Russell Glacier drainage in southwest Greenland (Figure 8). Due in part to the relative ease of access to Kangerlussuaq, it is a well-studied region and contains some of the longest-running continuous mass-balance measurements anywhere in Greenland (van de Wal et al., 2012). Mass balance stakes extend from "S1" near the terminus of the glacier to "S10" in the glacier's accumulation zone, with S10 located approximately 1850 m elevation and 130 km inland. A series of automated weather stations monitor radiation and climatological conditions both at the proglacial foot of the glacier (KAN-B) and along increasing elevations of the K-Transect (KAN-L, KAN-M, and KAN-U).

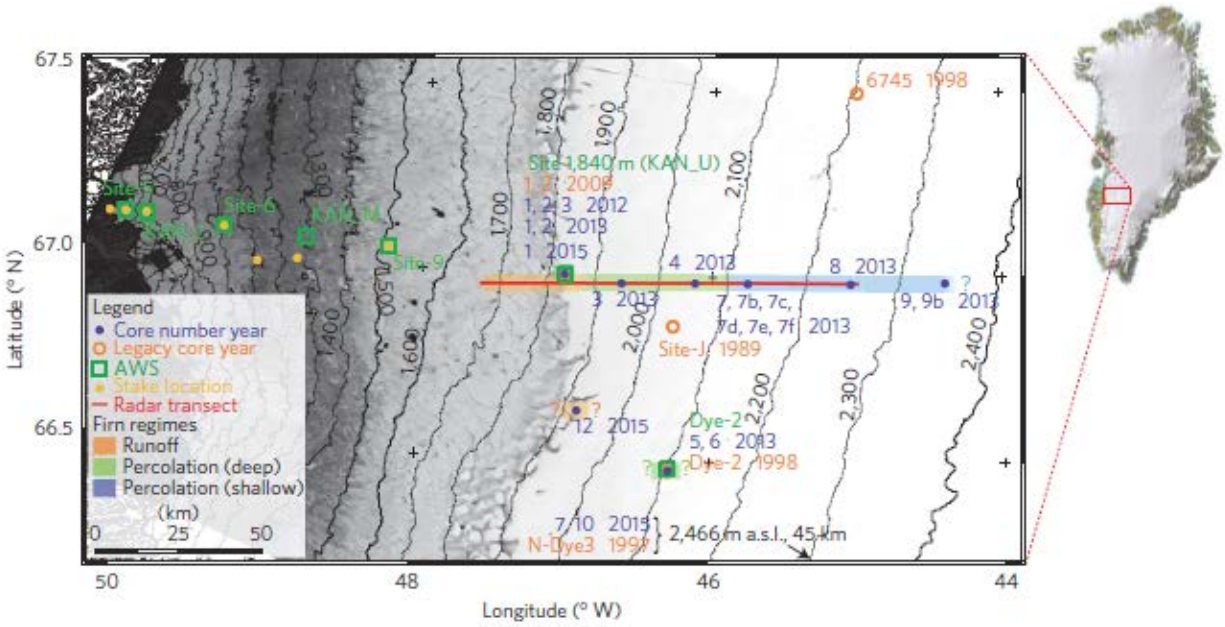

Figure 8 | 2012 and 2013 field campaign locations (image by Machguth et al., 2016).

In 2012, the Greenland Analogue Project (GAP) funded a field campaign for the Geological Survey of Denmark and Greenland (GEUS) and Aberwystwyth University to visit the KAN-U site. A portion of the project was called the "Surface Processes of the Lower Accumulation Zone" (SPLAZ), and among its goals were to study surface changes happening in Greenland's lower accumulation zone in the context or recent high-melt years, including above-average melt years in 2004 and 2007. In the anomalously warm melt summer of 2010 the KAN-U site was almost below the equilibrium line (van As et al., 2012), where melt nearly exceeded accumulation for the first time in the observational melt record on the K-Transect.

2.3 Identifying Thick Ice Slabs in Greenland's Firn

2.3.1 2012 Firn Cores

During the SPLAZ 2012 campaign, Horst Machguth and I drilled three 10-12 m firn cores (and several shallower ones) at the KAN-U camp in southwest Greenland's Russell Glacier drainage. Cores were drilled at 10 cm diameter and ice lenses were recorded at 1 cm resolution. Cores were cut into 10 cm long segments; each section was measured and weighed to calculate density (Figure 9).

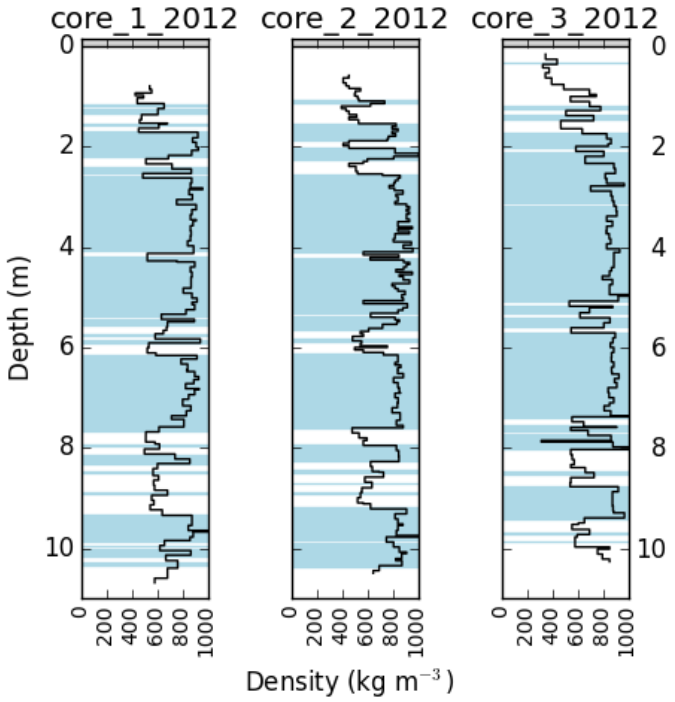

Figure 9 | Density (black line) & stratigraphy (blue span) of KAN-U cores drilled in 2012. Thick blue spans show multi-meter thick ice slabs from 2 to 7.5 meters' depth, with more firn pore space and thinner ice layers both above the slabs to the surface, and below the slabs up to 10 m depth.

Each core from the KAN-U site in 2012 is dominated by thick ice layers which begin approximately 1.75 m beneath the surface and continue with gaps for 4-5 additional meters

before more firn is observed at depth. Several shallower cores (3-5 m deep) showed similar stratigraphy, although their density and stratigraphy were not recorded.

2.3.2 *In Situ* GPR

500 MHz ground-penetrating radar data collected on the SPLAZ campaign indicated the thick ice layers were largely continuous within a 1 km grid surrounding camp (Figure 10). There was a visible match between “smooth” regions on the GPR signal and thick ice layers in cores drilled immediately adjacent to the GPR line. There didn’t appear to be any breaks or incongruities in the layers, and were largely consistent in thickness. Twenty transects of 500 MHz GPR profiles collected in a grid around the KAN-U camp all showed a similar pattern of thick consistent ice layers.

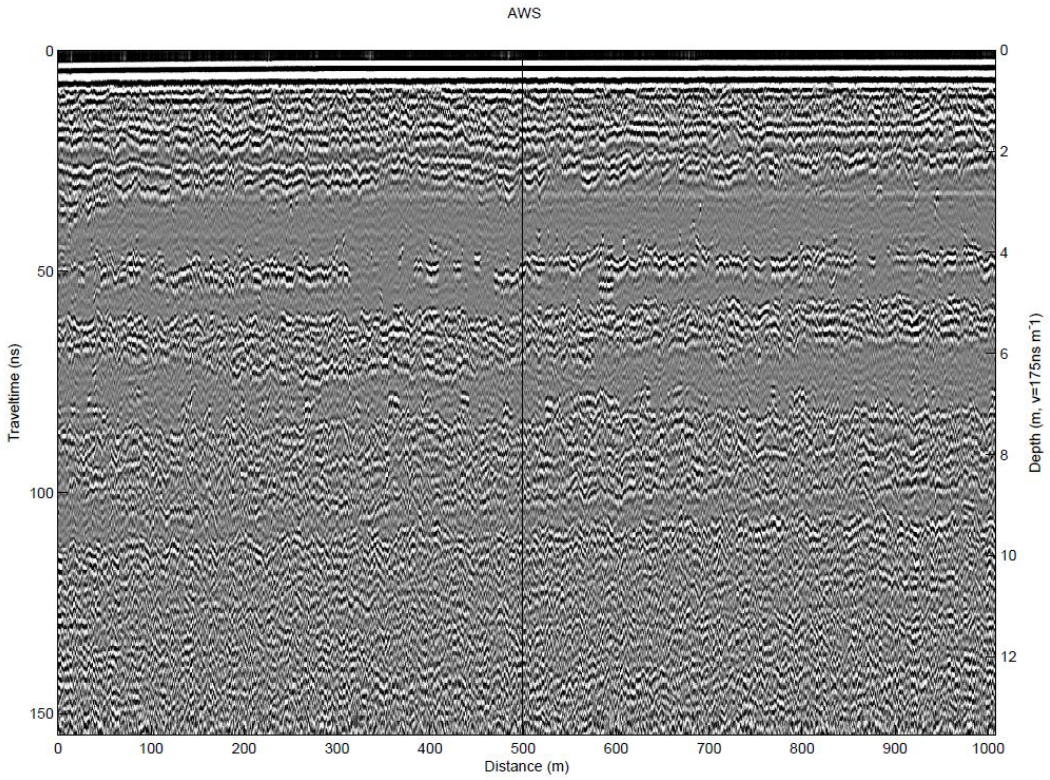

Figure 10 | 500 MHz GPR from a 1 km transect at KAN-U, Greenland, 2012. "Smooth" areas in the GPR coincide with thick ice layers identified in nearby cores (Figure 9). Ice slabs appear to be continuous along the 1 km GPR transect. (Image courtesy Rickard Petterson & Katrin Lindbäck, unpublished.)

2.3.3 Definition of Ice Slabs

In the context of this work, ice "lenses" refer to refrozen layers within snow and firn which form from refreezing in a single melt event or season (Benson, 1962). Lenses are typically thin (0-10 cm) and refreeze in heterogeneous and discontinuous patterns, both vertically and horizontally, within the firn (Brown et al., 2011). Due to spatial heterogeneity, meltwater can percolate through and around lenses along preferential flow paths, sometimes reaching significant depths (≥10 m) before refreezing (Humphrey et al., 2012). In regions of heavy melt and refreezing, ice lenses can thicken into ice layers (10-100 cm) which can become relatively impermeable on

small spatial scales (meters), but are still relatively heterogeneously scattered throughout the firn layer and contain spatial gaps between them where water could flow. Figure 11 below shows ice layers within six shallow firn cores collected 10 meters of each other at a site in the percolation zone of southwest Greenland, elevation 2150 m. Although relatively thick ice layers (10-60 cm) exist in all cores collected, their depths are very inconsistent and it is unclear whether ice exists consistently at any one depth. This indicates it is unlikely that such ice layers form a continuous impermeable layer capable of blocking percolation over wide areas. Low-permeability ice "slabs" refer to much thicker layers (≥1 m) that form when additional water refreezes between individual ice lenses and layers and anneals them together. Slabs are spatially extensive, span more than a kilometer, and cause the near-surface permeability of the firn to approach zero (Sommers et al., 2017). The work of this dissertation ignores thin ice lenses and layers which do not affect runoff on wide scales, and focuses solely upon LPISs in Greenland's firn layer.

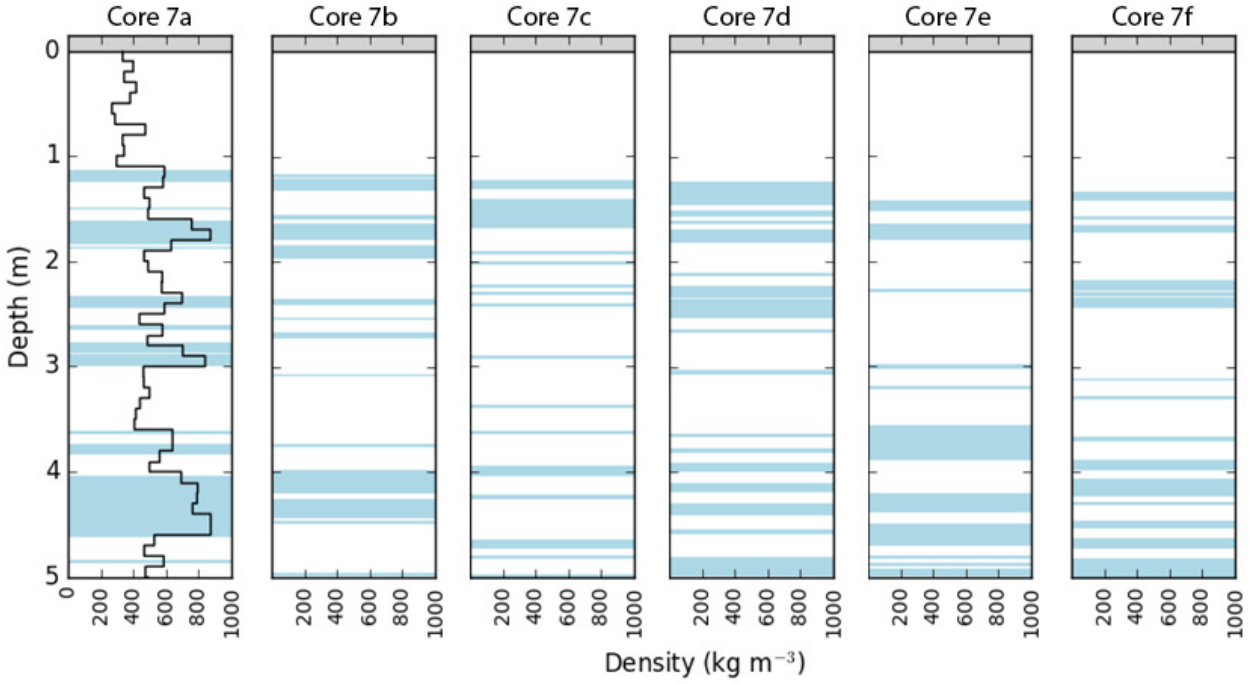

Figure 11 | Shallow cores collected at Site 7 (2150 m a.s.l.) on the ACT-13 transect within 10 meters of each other. Blue spans indicated ice volumes in the cores. The black line in Core 7a is the density profile, which was collected only for that core. Only stratigraphy was recorded in the remaining cores.

2.4 2012 Runoff Season

The summer of 2012 broke observational records for the Greenland ice sheet, both by large extent of melt in the satellite record (Nghiem et al., 2012) and the amount of runoff in regional climate models (Tedesco et al., 2013; Langen et al., 2017). By early July, melt reached Greenland's summit for the first time in observational history, covering roughly 98% of the ice sheet on July 8 and a majority of the ice sheet during a second major melt on July 29 (Figure 12). The GrIS's surface mass balance was 3.9 standard deviations below normal with a record melt of bare ice exposure, melt and runoff (Tedesco et al., 2013).

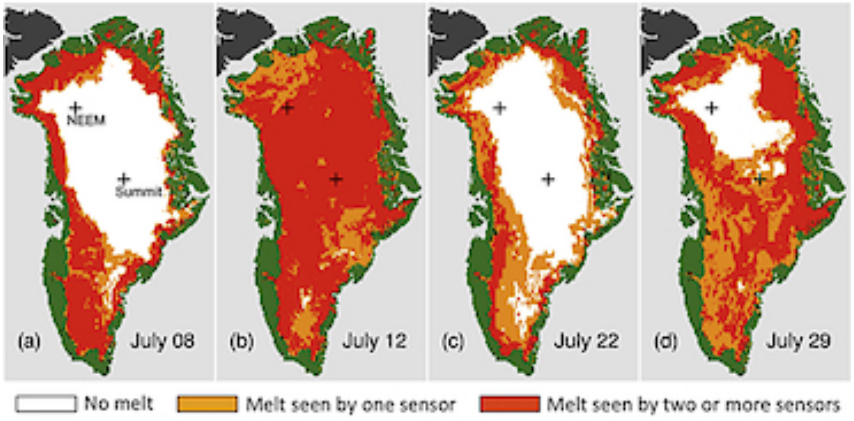

Figure 12 | Greenland 2012 melt extent as detected from passive microwave, scatterometry and optical satellite measurements (Nghiem et al., 2012). Orange areas indicate where one sensor detected melt, and red areas show where two or more sensors detected melt.

2.4.1 Satellite Imagery

A color-enhanced LandSat-7 image from July 16, 2012 (Figure 13) shows that surface saturation reached the proximity of the KAN-U site. Efficient surface drainage channels can be seen

transporting water downhill as runoff. It was the first time in the optical satellite record that runoff had been observed this high along the K-Transect.

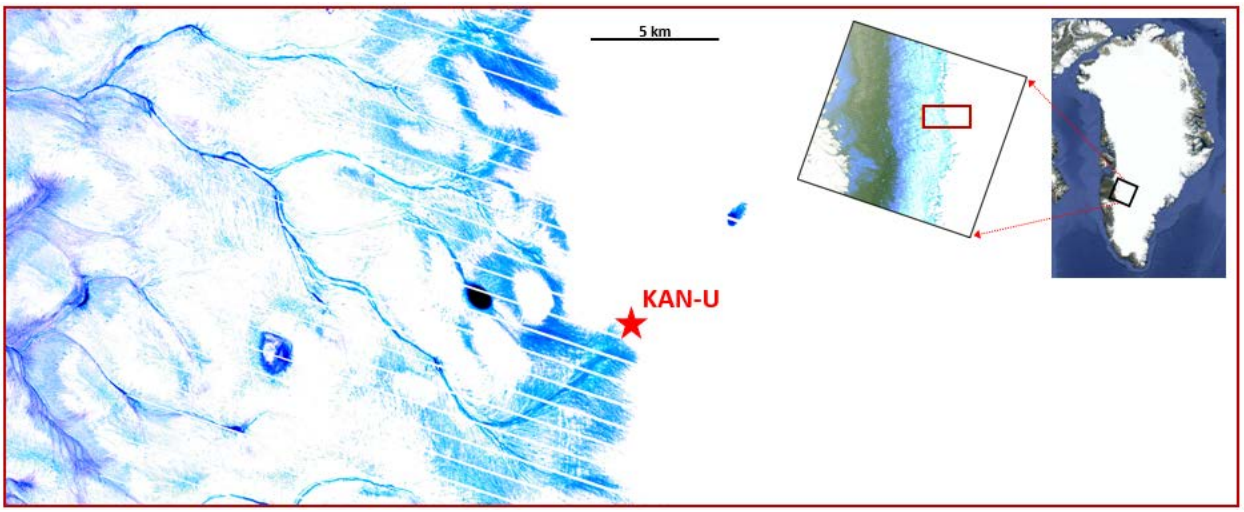

Figure 13 | LandSat-7 image (color-enhanced), July 16, 2012, showing runoff in the immediate vicinity of KAN-U, southwest Greenland.

A field team visiting KAN-U in August 2012 verified that the surface was dominated by slush; one field member punched his boot through refrozen surface ice, soaking the boot approximately 20-30 cm in slush (Paul Smeets, personal correspondence). A WorldView-1 image on August 12, 2012 shows slush fields and drainage channels emanating from nearby the KAN-U AWS (Figure 14). This suggests that water was actively running off from the KAN-U location in some capacity for nearly a full month during summer 2012.

Figure 14 | 5x5 km tile from WorldView-1 panchromatic image of KAN-U, August 12th, 2012 (Machguth et al., 2016).

2.4.2 Watson River Flooding

The Watson River flows from the Russell Glacier through the town of Kangerlussuaq on Greenland's southwest coast. KAN-U is located in the accumulation zone of the Russell Glacier, draining into the Watson River. On July 11, 2016, the Watson River reached its highest discharge levels on record at 3100 $m^3 s^{-1}$, washing away the supports of a large bridge built in 1953 (Figure 15) and sweeping a large Caterpillar earth mover off the bridge.

Figure 15 | Photograph of the Watson River bridge in Kangerlussuaq, 16:00 West Greenland time on July 11, 2012. (Image courtesy of Jens Christiansson, Mikkelsen et al., 2016).

The cumulative atmospheric energy available to melt the Russell Glacier feeding the Watson River was only 3% more in July 2012 than it was in the previous record melt season of 2010, making the melt conditions statistically indistinguishable in that drainage. Despite this small difference, discharge from the Watson River was far higher in 2012, indicating more than just meteorological conditions alone were responsible for the difference in discharge from the Russell Glacier (Mikkelsen et al., 2016).

2.4.3 Saturation Modeling

Ice slabs within the firn at KAN-U in 2012, although shallow, were not located immediately beneath the snow surface. A layer of firn approximately 1.75 meters thick lay atop the first instance of ice thick ice layers seen in cores (Figure 9). In order for slush to be visible on the surface at KAN-U and runoff to occur, near-surface pore space must be completely filled (Pfeffer et al., 1991). To test whether melt could have saturated the surface within the time span of observations, I created a water table model based on the a priori assumption that one of two sets of ice layers within the cores at KAN-U could have possibly blocked percolation (Figure 16). The model is intended to answer the question *"If ice slabs blocked percolation at KAN-U, when would slush fields be expected to form at the surface given the observed summer 2012 melt?"*

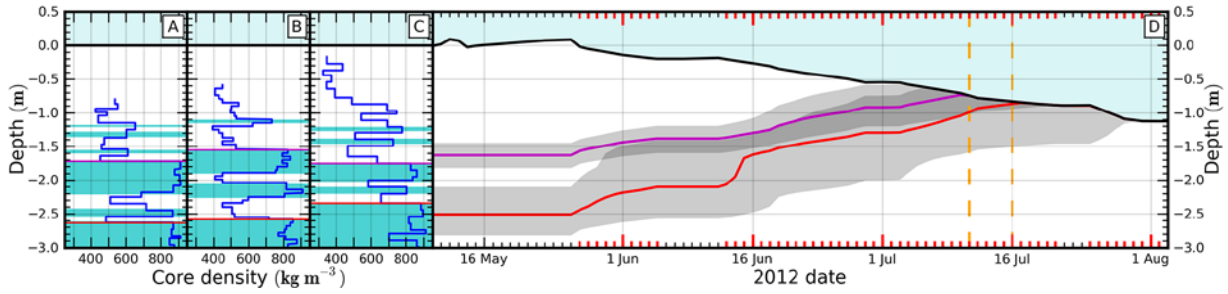

Figure 16 | Firn water table model at KAN-U, southwest Greenland, summer 2012. (A-C) show density (blue lines) and near-surface stratigraphy (aquamarine spans) in three cores drilled at the KAN-U site in Spring 2012. Purple and red lines represent two assumptions about which set of ice layers may be capable of blocking percolation in summer 2012. (D) shows the simulated water-table depth (purple and red, with 95% confidence intervals) as the near-surface firn fills with water, given each assumption of the blocking layer. The black line is the surface lowering, as measured by a sonic ranging sensor on the KAN-U weather station. Red ticks on the horizontal axis are days when 2-m air temperature was above 0 °C and melt would have occurred. The orange dotted lines indicate July 11, the date of the peak flow of the Watson River (Figure 15) and July 16, the date of the LandSat-7 image when runoff is seen to occur from the vicinity of KAN-U (Figure 13).

A Monte-Carlo simulation was run to determine the timing of runoff at the surface of KAN-U. Core densities for each firn layer (and therefore firn pore space available to fill with water) were derived from one of three cores at the KAN-U site (Figure 16A-C). Near-surface snow density (which was not measured in the cores) and snow depth was taken from one of 42 snow pits dug at the KAN-U site in Spring 2012 (Mikkelsen et al., 2016). Air temperature and surface height were recorded from the nearby KAN-U automated weather station. In days when temperatures were above freezing (Figure 16D, red tick marks), lowering of the surface was attributed to melt. As snow was melted at the surface, water would accumulate within the available pore space of the underlying firn, atop a blocking ice layer, and the water table would rise. The density of refrozen ice was determined by selecting one the density from of 67 all-ice segments from cores drilled at KAN-U. Sublimation was subtracted from the surface by randomly selecting a value ±50 % of the sublimation calculated by an observationally-forced surface mass balance model specifically tuned to the K-transect (van As et al., 2012). One of two assumptions for the "blocking ice layer" was selected from one of the three cores, either a 60-90 cm span of ice found ~1.5 m deep in cores or a several-meter thick set of ice layers that begun ~2.5 m deep in the firn column. 10^7 iterations were run to simulate the rise of the near-surface water table using values from each of the variables described above. When the water table reached the surface, the simulation was stopped and all further surface lowering is attributed to runoff.

The Monte-Carlo simulations predict that within the 95% confidence intervals (Figure 16D, grey spans), if either of the two sets of ice layers were capable of blocking deep percolation, the near-surface firn at KAN-U would have saturated sometime during the month of July. The median of the models under both ice-layer assumptions shows the firn saturating in early- to mid-July,

consistent with the satellite and in-situ observations. The close match between the calculated dates by which the KAN-U site would be expected to exhibit surface runoff (Figure 16) and the date when saturation and runoff was observed at KAN-U (Figure 13) adds confidence that the ice slabs found at KAN-U could have acted as thick perched impermeable layers, causing runoff atop them in the summer of 2012.

2.4.4 ACT-13 Firn Cores

The following spring 2013, cores were drilled along the extended K-Transect (Figure 8). Cores 1 and 2 are from 1850 m elevation at KAN-U with the remaining cores drilled at progressively higher elevations. Core 9 is at 2350 m (the EKT station) near the ice divide (Figure 17).

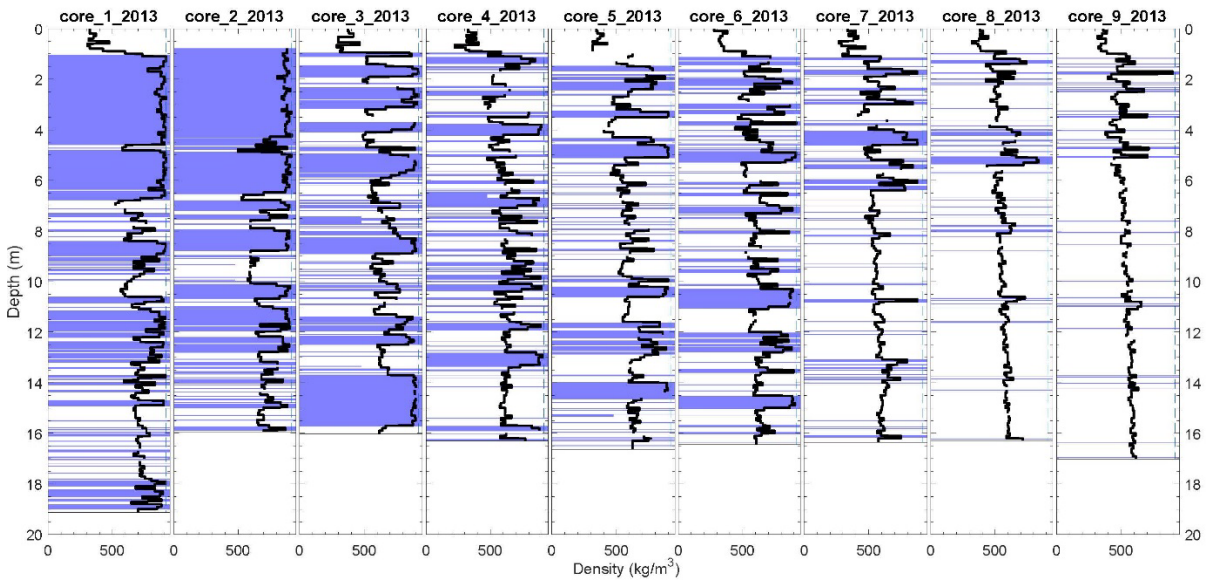

Figure 17 | Firn cores along the ACT-13 transect. Black lines show ice and firn density measured in 10 cm intervals. Blue spans show ice lenses and layers measured at 1 cm resolution in each core, before the cores were cut to measure density. Cores 1 and 2 show the multi-meter thick near-surface ice slabs at KAN-U after the 2012 melt season. Core elevations range from 1850 m a.s.l. at KAN-U (Cores 1 & 2) to 2350 m a.s.l. about 70 km from the ice divide (Core 9).

Firn cores immediately after the 2012 melt season confirm that at the KAN-U site (ACT-13 Cores 1 & 2), despite the runoff observed from the surface, pore space still remained at depth which had not been filled with melt water. The ice slabs appeared to have grown thicker and more continuous at the KAN-U site, but when cores are compared side-by-side, no evidence is seen that any meltwater percolated and refroze beneath them (Machguth et al., 2016).

2.4.5 Uphill Migration of the K-Transect Runoff Limit

Landsat images were collected on the K-transect from the Landsat 4, 5, 7, and 8 satellites during the peak melt season, July 15 through August 31, each year from 1985 to 2015. The upper extent of visible surface rivers were identified in each image, and the maximum elevation of liquid water in each year was selected to determine that year's maximum runoff elevation (Figure 18).

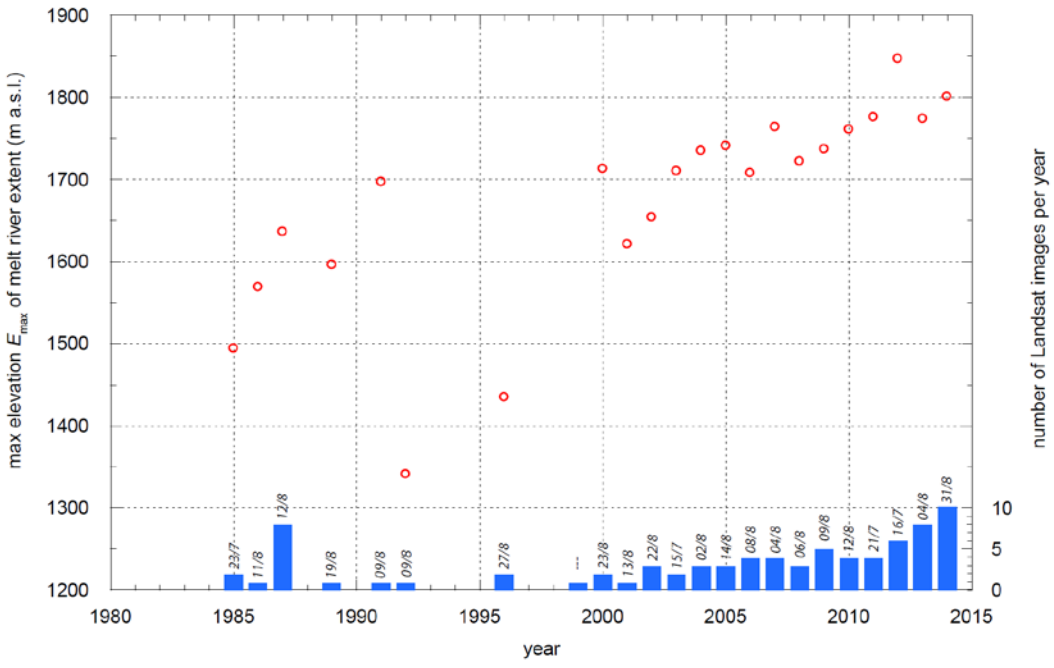

Figure 18 | Maximum elevation E_{max} of supraglacial rivers (red circles) in the vicinity of the radar transect, as mapped from Landsat 4, 5, 7, and 8 imagery. Blue bars indicate the number of available Landsat images in the time frame July 15 to August 31 for every year. Date of the image showing the highest melt river extent is indicated on top of the bars. (Machguth et al., 2016.)

Earlier years in the LandSat record (Figure 18) suffer from a relatively low number of available images, which may cause a low-bias in those years. During the years 2000-2015, the maximum extent of runoff appears to have steadily risen approximately 10 meters elevation per year, with the highest visible extent in 2012 of 1850 meters above sea level (m a.s.l.), the KAN-U site. The imagery suggests a progressive uphill migration of the runoff line along the K-Transect since at least the year 2000.

Analysis of repeat cores in 2012 and 2013 indicates that approximately 66 cm water-equivalent was lost to runoff from the KAN-U site in 2012. Ice slab areas contributed approximately 14±3 % to the total runoff volume in southwest Greenland that summer, adding to the already-significant melt that summer (Machguth et al., 2016). The "runoff line" is typically defined as topmost elevation at which any water is lost, having zero runoff at that location. If KAN-U lost 66 cm of melt, it suggests the K-Transect runoff line was somewhere uphill from the KAN-U site in 2012. A regression model has indicated the runoff limit was likely approximately 1900 m elevation during the 2012 melt season (Machguth et al., 2016).

2.5 Continued Growth of Ice Slabs

Shallow 3 m cores were drilled by another team at the KAN-U location in 2009, and no ice slabs greater than 1 m thickness were present in the shallow firn. Our teams have drilled repeat cores at KAN-U in 2012, 2013, 2015, 2016, and 2017 (Figure 19**Error! Reference source not found.**), identifying the stratigraphy of the cores through time.

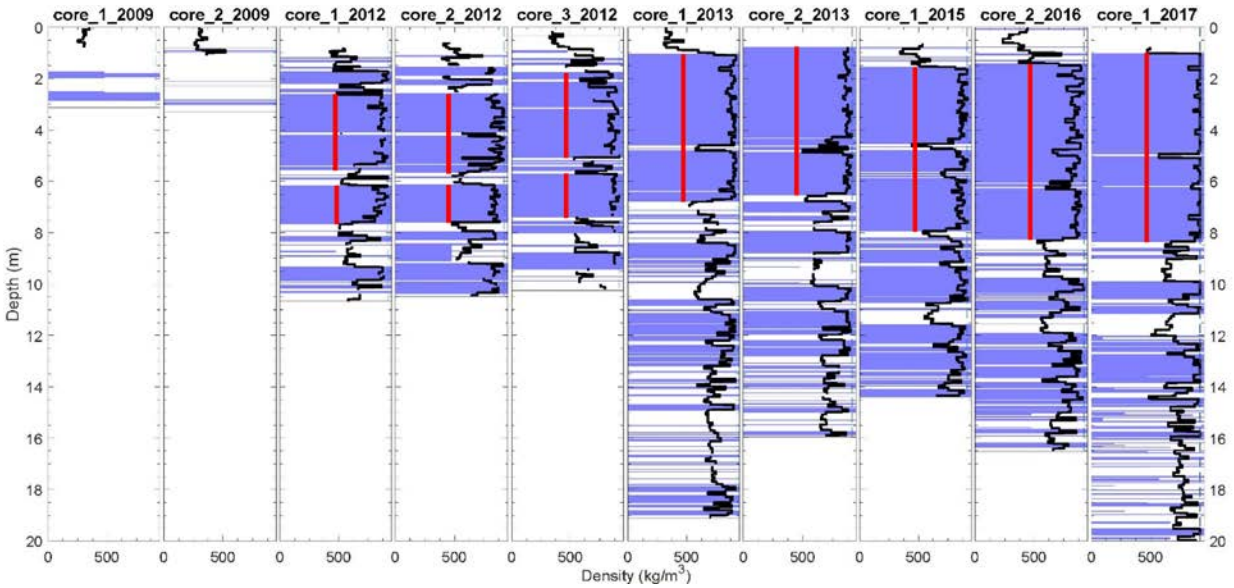

Figure 19 | Firn cores at the KAN-U field site, 2009-2017. Black lines indicate density, blue spans are stratigraphy. The red vertical lines show the thickness of near-surface ice slabs in the cores. Ice slabs grew from ~4.7 m thick in Spring 2012 (with a 0.5 m gap in the middle of them) to 7.2 m thick in Spring 2017, indicating a steady growth of the slabs at the KAN-U site. Shallow cores in 2009 were not deep enough to tell if slabs existed beneath them, but show that no thick slabs were present in the top 3 meters at that time.

Repeat cores indicate that the Low-Permeability Ice Slabs (LPISs) have grown at the KAN-U site between 2009 and 2017. In 2012, pore space between 2.5 and 5.5 m depth was filled primarily with ice. Ice slabs more than a meter thick were present in all three cores drilled that year. After the 2012 melt season, ice layers grew to form a nearly-continuous ice slab approximately 5 meters thick observed in cores in 2013. By 2017, the ice slab grew to 7 meters thick. This indicates that even in years in which runoff is not visible from the surface such as 2013 and 2014, ice slabs continue to grow by refreezing additional meltwater.

2012 and 2016 were the two years in our study period when KAN-U melted enough to saturate the surface. A layer of fresh snow rests atop a solid refrozen ice slab the following Spring (2013 and 2017), with no porous firn visible at the top of the firn column. After relatively cool years

where melt did not overwhelm near-surface pore space, some firn is visible (containing thin ice lenses) on top of the ice slabs. In both warm and cool summers, meltwater annealed atop the ice slabs, growing them progressively thicker.

The “BAB-U” drilling site, visited on the 2015 and 2017 Arctic Circle Traverses, is 40 km southeast of KAN-U and 80 meters’ higher in elevation (66.63°N, 46.89°E, 1927 m a.s.l). Although slightly less melt occurs at BAB-U than at KAN-U, approximately three meters’ of ice slabs were evident between two and five meters’ depth in 2015 (Figure 20). This layer is an additional meter thicker when re-drilled in 2017. Although the time-series of cores at BAB-U is short with only two individual years of data, ice slabs thickening there are consistent with the longer time-series collected at KAN-U.

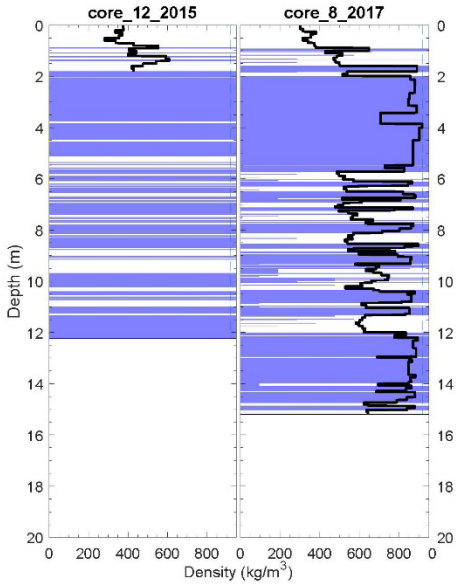

Figure 20 | Firn cores from the BAB-U field site, 40 km southeast of KAN-U, 2015 and 2017. Near-surface ice slabs appear to grow approximately 0.5 m thicker in the intervening two years, consistent with ice slabs at KAN-U (Figure 19).

2.6 Ice Slab – Albedo Feedback

When ice slabs cause water to be trapped near the surface, ensuing slush fields darken the surface. This darkening effect is immediately visible in optical imagery (Figure 13). Water is significantly darker than snow, both in visible wavelengths and infrared (Baldridge et al., 2009), and thereby absorbs a large amount of incoming solar radiation. In mid-summer when the surface of the snow is already melting and thereby isothermal, the extra absorbed radiation creates extra melt, which can significantly increase the summer melt totals for a given location. Radiation sensors installed at KAN-U in 2012 detected that broadband albedo quickly dropped from 0.78 to 0.71 and absorbed 28% more radiation (213 MJ m^{-2}) than the average of other years since 2009 (Charalampidis et al., 2015). This extra energy accounted for 36% of the total surface lowering due to melt at KAN-U, accelerating runoff beyond what would have already been a large melt year due to atmospheric conditions. The total atmospheric radiation at KAN-U was nearly identical in summer 2010 as it was in 2012 (Mikkelsen et al., 2016), but the darkened surface accounted for the extra melt and runoff. In this way, ice slabs enhance melt after they have formed. Since we know they block percolation and cause runoff, this feedback is a mechanism by which the expansion of ice slabs to higher elevations of Greenland's runoff zone may act as a positive feedback mechanism, enhancing the runoff of the ice sheet.

2.7 Discussion and Conclusion

We have identified that ice layers have the ability to cause runoff in regions of the ice sheet where water was previously assumed to percolate and refreeze. Pore space between ice layers within the firn can fill, merging ice layers together to form thick and continuous ice "slabs." We have shown that the runoff line from the ice sheet has progressively moved uphill over the top of

these slabs, and significantly raised the elevation of the runoff line along the K-Transect in the exceptional 2012 melt season. We have shown that these slabs have continued to grow thicker, even in lower-melt years when the near-surface snow has not saturated. Once formed, the slabs isolate firn at depth which was previously assumed to act as a long term “buffer” that could absorb high-elevation runoff for decades (Harper et al., 2012). With this buffer isolated from melt, the runoff line can migrate uphill far more quickly than previously assumed in a warming climate, which serious implications for future runoff from the Greenland ice sheet.

3 MAPPING LOW-PERMEABILITY ICE SLABS ACROSS GREENLAND

3.1 Introduction

Given enough meltwater and cold content in polar firn, ice lenses can anneal together to form extensive low-permeability ice slabs (LPISs) (Chapter 2). In warm melt summers when the near-surface snow and firn is overwhelmed with meltwater, LPISs block percolation to depth. Once the near-surface snow has saturated, they can cause runoff in areas where meltwater used to refreeze entirely. This phenomena was observed in southwest Greenland in the record-breaking 2012 melt summer, when ice slabs generated an extra 14±3 % to runoff in that region of Greenland (Machguth et al., 2016) and flooded runoff-fed rivers nearby (Mikkelsen et al., 2016).

It is yet unknown how much of the Greenland ice sheet has been affected by LPISs. Observations along one transect in southwest Greenland are not sufficient to quantify their impact across the remainder of the ice sheet. Field observations collecting firn cores and GPR are valuable tools to measure LPISs, but are prohibitively expensive for more than a small number of individual campaigns. Satellite remote sensing can cover large areas, but is typically ineffective at measuring sub-surface processes more than 1-2 meters deep. Airborne ground-penetrating radar is an ideal tool for measuring LPISs, having the ability to measure deeper into the firn than satellite observations but cover more area than ground-based measurements.

NASA's Operation IceBridge program was begun in 2010 to bridge the altimetry gap between the IceSat-1 and IceSat-2 satellites (Schutz et al., 2005; Abdalati et al., 2010). IceBridge carries

an array of scientific instruments to map and measure ice sheet and sea-ice processes over Greenland, Antarctica, Arctic Canada, Patagonia, and other polar regions (Figure 21).

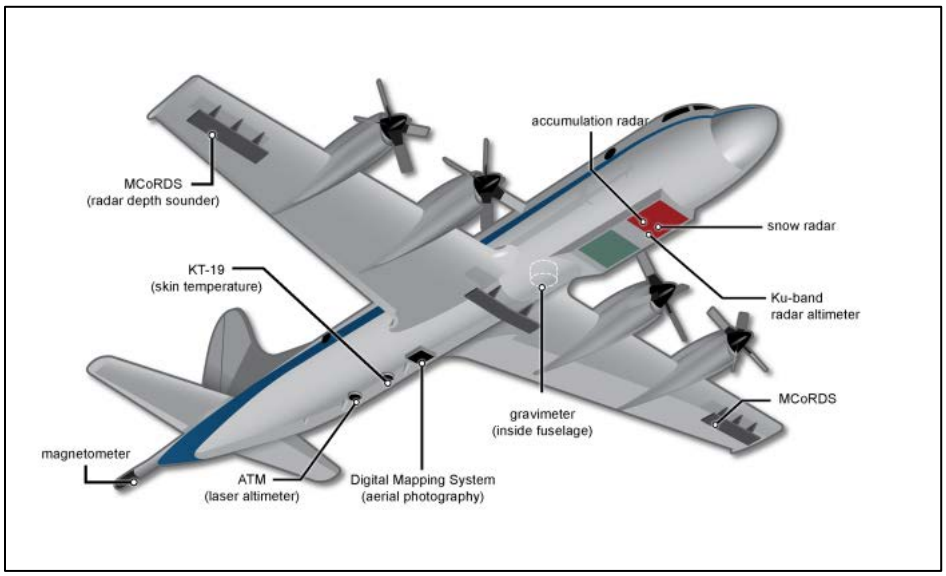

Figure 21 | Operation IceBridge schematic on a P-3 aircraft. (Image from https://icebridge.gsfc.nasa.gov/)

IceBridge carries several radar systems, each developed for specific purposes. The MCoRDS radar is a deep-scanning instrument capable of measuring bedrock elevations through multiple kilometers of ice. The KU-band altimeter measures surface elevation and snow subsurface elevations over sea ice and ice sheets. The Snow Radar is a high-frequency system ideal for measuring snow depth to 0-3 meters over ice sheets and sea ice, as well as freeboard elevations of sea ice leads. The IceBridge Accumulation Radar (AR) is a mid-frequency system capable of penetrating tens to hundreds of meters deep to identify firn and shallow-ice processes deeper than the snow or Ku radar can penetrate, but at higher resolution than the deep-scanning MCoRDS instrument. The AR radar data is used for the majority of work in this chapter.

IceBridge radar instruments and antennae are improved and upgraded between campaigns to provide the "best" data possible in any given flight campaign. IceBridge flies on several planes, including a P-3, DC-8 and occasionally a C-130, depending upon the needs and limitations of individual campaigns, sometimes with different antenna configurations on each aircraft. Although the instruments continue to improve over time, the inconsistent instrumentation introduces considerable technical challenges when attempting to combine multiple years of data into a single comparable dataset, or when trying to detect inter-annual change.

An IceBridge flight-line was collected along an uphill transect approximately 3 km south of the KAN-U field site on April 23, 2012 (Figure 22). The quick-look files provided by NASA alongside the IceBridge AR data shows ice slabs similar in pattern and thickness to those seen at KAN-U by the SPLAZ campaign. The SPLAZ cores and *in situ* GPR were not immediately in the path of an IceBridge flight line, however, so no direct comparison could be made that year. If cores and *in situ* GPR could be taken directly coincident to an IceBridge AR flight line, it would hypothetically be possible to scale-up observations and map ice slabs across Greenland wherever IceBridge has flown. We convinced the Operation IceBridge team to fly the same flight-line the following year in 2013 and organized the ACT-13 field campaign to investigate a coincident transect underneath it, immediately following the 2012 melt year.

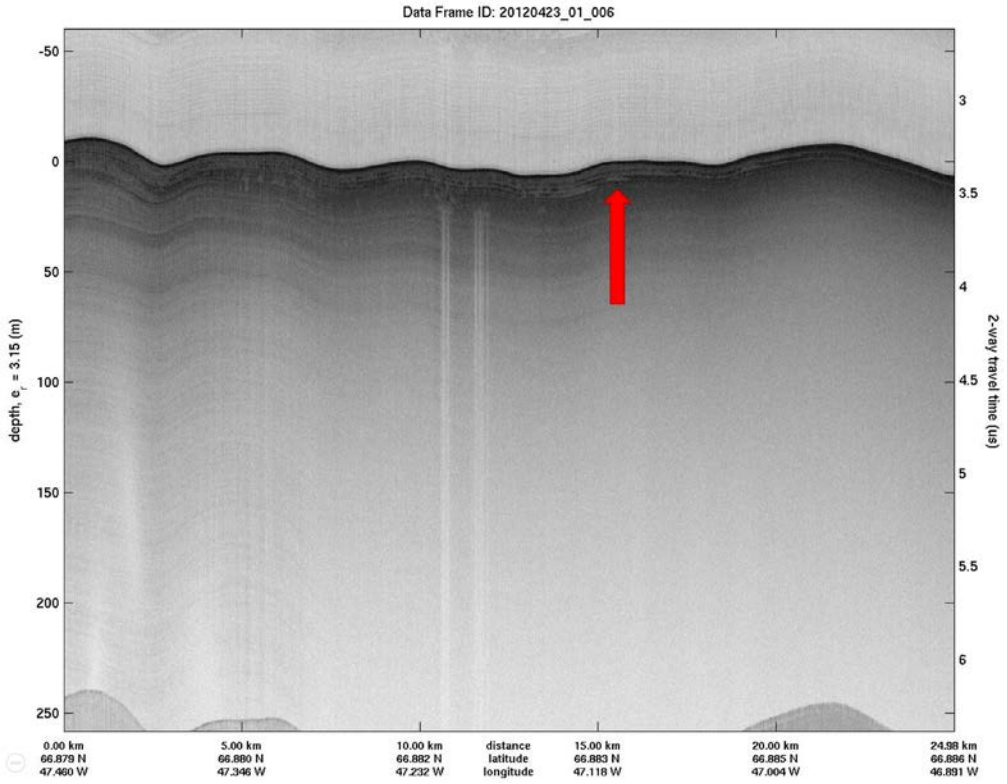

Figure 22 | IceBridge quick-look file for Accumulation Radar segment 20120423_01_006. The red arrow points to apparent ice slabs in the near-surface firn.

3.2 Methods

3.2.1 Overview

The goal of this work is to create the first map of low-permeability ice slabs across the Greenland ice sheet. This task is performed in four major steps. **First,** I use ACT-13 cores to process ACT-13 *in situ* GPR to identify LPISs and quantify its accuracy in doing so. **Second,** I process IceBridge AR data from multiple years to minimize systemic errors and create a single, comparable, usable data set for the purpose of identifying LPISs. **Third,** I match ACT-13 *in situ* GPR with the adjacent IceBridge AR "reference track" flight line to develop an algorithm for identifying ice slabs in AR data, again quantifying its accuracy in doing so. **Fourth,** I use this

algorithm to map the presence and thickness of LPISs across the Greenland ice sheet and peripheral glaciers and ice caps, wherever IceBridge has flown.

3.2.2 Cores

Nine firn cores were collected along the ACT-13 transect between April 22 and May 14, 2013. Two more were collected at the KAN-U field site and two more at the Dye-2 station. The locations of the cores are mapped in Figure 8 (Chapter 2), with the firn profiles presented in Figure 17. The cores range from areas with thick ice slabs (KAN-U) up to the high-elevation percolation zone where only thin lenses occur in a mix of dry and wetted firn layers. All cores except Core 9 are immediately adjacent to GPR data collected on the ACT-13 campaign.

3.2.3 *In Situ* GPR

3.2.3.1 GPR Pre-processing

In situ GPR data was collected from a Malå 800 MHz shielded GPR Rx/Tx antenna, with traces collected every 0.5 seconds. Traces had an average spacing of 1.42 ± 0.13 m along-track, which was later resampled using a nearest-neighbour approach to constant 1.5 m spacing. GPR transects were collected along a 1×1 km grid (50 m spacing) adjacent to Cores 1 and 2 at the KAN-U site, in select tracks near Cores 5 and 6 at Dye-2, and along the primary transect line adjacent to all of the remaining cores. GPR trace locations were recorded by a Trimble R7 GPS receiver every 1 second. Since the GPR antenna was sitting on a sled behind a skidoo where the differential Global Positioning System (dGPS) antenna was mounted, I subtracted 1.35 m vertical 3.65 m along-track horizontal offsets to the recorded dGPS locations to account for the spacing difference between them. Because GPR traces were recorded every 0.5 s while the dGPS

recorded locations every 1 s, GPR trace locations were linearly interpolated between dGPS positions. I applied a high-pass dewow filter with a 1.25 ns time window (one wavelength) to remove low-frequency artifacts and a linear gain filter to enhance the signal at depth. We combined individual GPR files collected along the main transect and the KAN-U grid to form continuous radar transects.

3.2.3.2 Local log-variance calculations

A moving window spanning three traces horizontally (4.5 m) by thirteen samples vertically (1.3 ns, ~23 cm, the span of one 800 MHz radar wavelength in firn) measured the variance of the signal in the 3x13 local neighborhood surrounding each sample pixel. Thick ice slabs, having a homogeneous physical structure compared to the surrounding firn, result in a lower local variance than samples within more porous and heterogeneous firn. GPR data were processed in their original 16-bit signed integer format as the gain/bias conversion from digital number to signal power would not enhance the signal further. We applied a $\log_{10}$-transformation to the GPR local variance data to convert to decibels and condense the logarithmic distribution of the data into a more normalized distribution.

3.2.3.3 Adaptive depth de-trending

The GPR signal decays much more quickly with depth when traveling through porous firn than through solid ice slabs. After performing log-variance calculations, the variance of the signal still decayed with depth in high-elevations regions dominated by firn with little refrozen ice (Figure 17, cores 4-9). This vertical heteroscedasticity in the GPR data causes weaker signals at depth in

firn than in pure ice, resulting in false positive (Type-1) errors if uncorrected. To remedy the signal decay in firn versus ice, I applied an adaptive vertical de-trending scheme to reduce Type-1 errors in firn. The algorithm calculated the linear vertical trend (slope and intercept) in the GPR variance at each individual trace (Figure 23) and smoothed the slopes and intercepts along-transect with a 1-km Gaussian filter (Figure 24). In regions where the trend was negative (the signal decayed with depth), I corrected the linear trend to normalize the signal's strength with depth. Regions where the slope was positive, indicating variance increased with depth, were located in areas where thick ice slabs are located on top of more porous firn. The trends in these ice slab areas tended to have a "step-change" pattern rather than a true linear decay, and the p-values of the trend lines were typically higher ($p \geq 0.05$) than in areas dominated solely by firn. In these areas I set the slope to zero to avoid Type-2 (false negative) errors that might falsely enhance the signal in solid ice slabs. The radar was linearly adjusted using the slope/intercepts on the Gaussian-smoothed trend line in order to normalize the signal to depth.

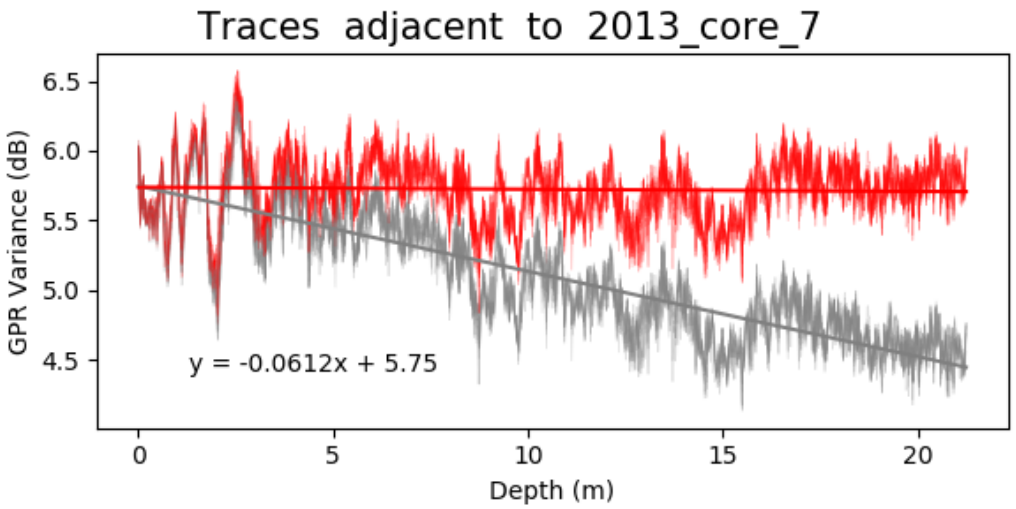

Figure 23 | GPR traces with depth, for the 10 traces nearest the ACT-13 Core 7. Original traces are in grey, de-trended traces in red. The equation references the slope and intercept of the trend line. x is depth and y is GPR variance. The traces here are located at approximately trace number 58,200 in Figure 24.

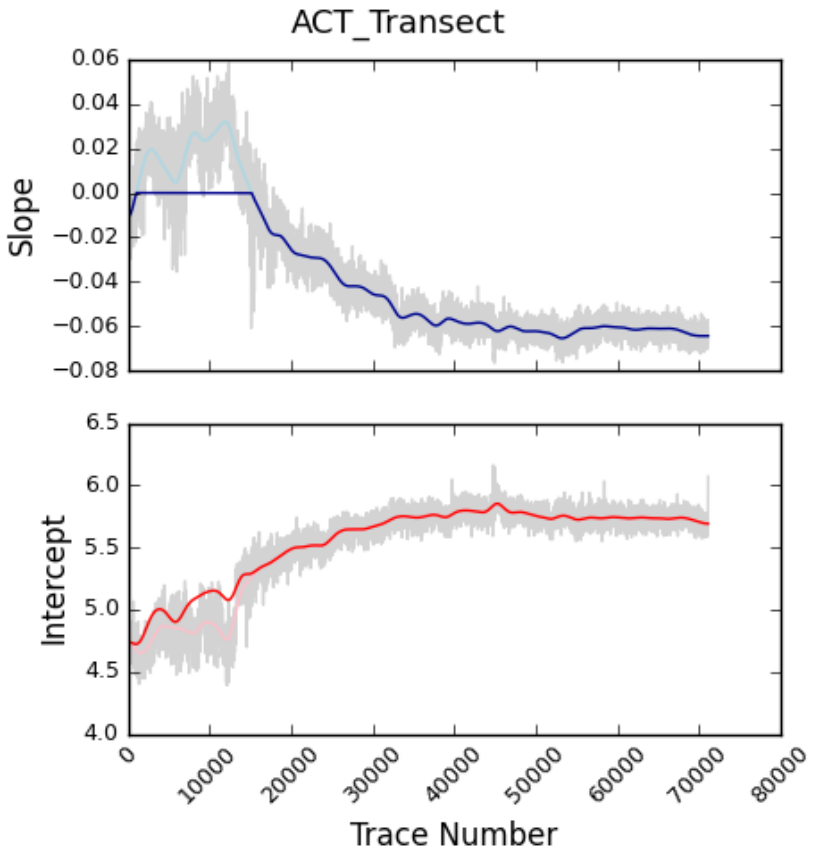

Figure 24 | The vertical slope and intercept of the log-variance of each GPR trace along the main GPR transect. 1 km Gaussian smoothing filters are shown in blue (for slope) and red (for intercept) both with and without omitting positive slope values. Slopes and intercepts were calculated for each trace on the GPR lines and used to correct the extinction of traces to depth. Extinction was greater in areas of porous firn than in areas dominated by ice.

After depth-detrending the data where it still decayed in firn, the GPR variance signal was now consistent with depth, and the strength of the signal corresponded more closely to differences in physical firn structure rather than decay of the signal.

3.2.3.4 Time-depth conversion

The propagation speed of a GPR signal in firn depends upon the physical and dielectric properties of the medium through which it passes, and is dependent upon frequency and interference patterns as well (Jol, 2008). A formula previously postulated by Robin (Robin, 1975) and discussed later by Kovacs and others (Kovacs et al., 1995) computes the dielectric constant of firn (ε_r') with specific gravity (ρ, a unitless measure of density) and a unitless empirical coefficient λ:

$$\varepsilon_r' = (1 + \lambda\rho)^2 \quad (6)$$

The dielectric constant (ε_r') is used to convert two-way GPR travel time (t) to signal depth (D), with c being speed of light in a vacuum:

$$D = \frac{tc}{2\sqrt{\varepsilon_r'}} \quad (7)$$

Robin empirically computed the value of the coefficient λ to be 0.851 (Robin, 1975), but Kovacs et al. showed this formulation produced dielectric constants that were too high tested against radar refraction sounding experiments (Kovacs et al., 1995).

The ACT-13 GPR data indicate that regions of low signal variance correlate strongly with high-density ice slabs. Porous firn has many ice-air surfaces with high-dielectric gradients compared to solid ice, which corresponds to higher signal backscatter. Signal noise and core density should have a negative correlation. I chose a range of values for λ between 0.60-0.90 at 0.01 increments, creating an array of computed depths for each firn layer. I measured the Spearman correlation[1]

[1] Spearman correlation coefficients offer slightly weaker values than traditional Pearson correlations, but do not rely upon the assumption of normalized data. Since neither the core densities nor GPR samples are normally distributed, I chose to use Spearman correlations rather than Pearson.

between core density and the signal variance of the ten nearest GPR traces to each core. Lower-density firn contains more pore space than higher-density firn due to an increased number of pores and reflective surfaces for the GPR. Solid ice, in comparison, ice is denser than firn and contains many fewer highly-reflective surfaces, corresponding with a weaker and more homogeneous GPR return. High GPR variance should correspond with low densities in the cores, producing a negative correlation. Although the relationship between density and GPR variance is likely not purely linear and the correlations may be weak, such a correlation should be enough to identify where ice slabs in the firn best match low-variability signals in GPR, and thus back out the GPR speed that most closely aligns these areas. A λ value of 0.734 produces the strongest negative correlation between core specific gravity and GPR log-variance (Figure 25), providing the best local fit between the core densities and neighboring GPR traces.

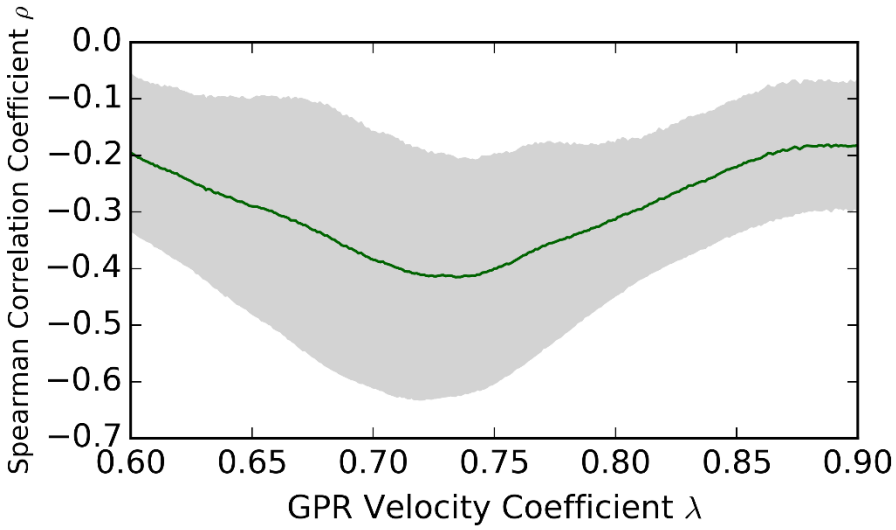

Figure 25 | GPR velocity coefficients (λ, unitless) plotted as a function of Spearman correlation between GPR log-variance calculations and firn core density at equivalent computed depths. Mean correlation is in green, standard deviation in grey.

These values are consistent with the conclusions of Kovacs and others (Kovacs et al., 1995) and produce an average GPR propagation speed of 182.4 m μs^{-1} through refrozen ice within firn (density 873 ± 25 kg m^3, Machguth et al., 2016), with slightly faster speeds traveling through less-dense porous firn. We used this value to compute the depth and thickness of refrozen ice layers in GPR traces.

3.2.3.5 Ice slab identification

Given the 4.5 m x 23 cm vertical size of our 3x13 moving window, the theoretical lower limit of detection for ice lenses in firn is ≥0.46 m thickness spanning at least 9.0 m horizontal distance according to the Nyquist frequency (Grenander, 1959). Ice layers thinner than this which freeze heterogeneously in the firn (Brown et al., 2011) are lost in processing. A local variance of 100,000 ($10^{5.0}$, 16-bit local neighborhood signal variance) was chosen to identify ice layers which maximized the agreement between GPR-detected ice layers and ice layers ≥50 cm thick in adjacent cores (Figure 26). We chose this cutoff to minimize the occurrence of Type-1 (false positive) errors in picking thick ice layers, especially in higher-elevation cores with little or no thick ice. Based on average Type-1 and Type-2 errors, the GPR cutoff correctly identified thick ice layers ≥ 50 cm thick with average accuracy of -13.2 to +3.20 %. Generally speaking, the *in situ* radar is able to reliably identify the presence of thick and continuous ice layers while slightly underestimating their thickness.

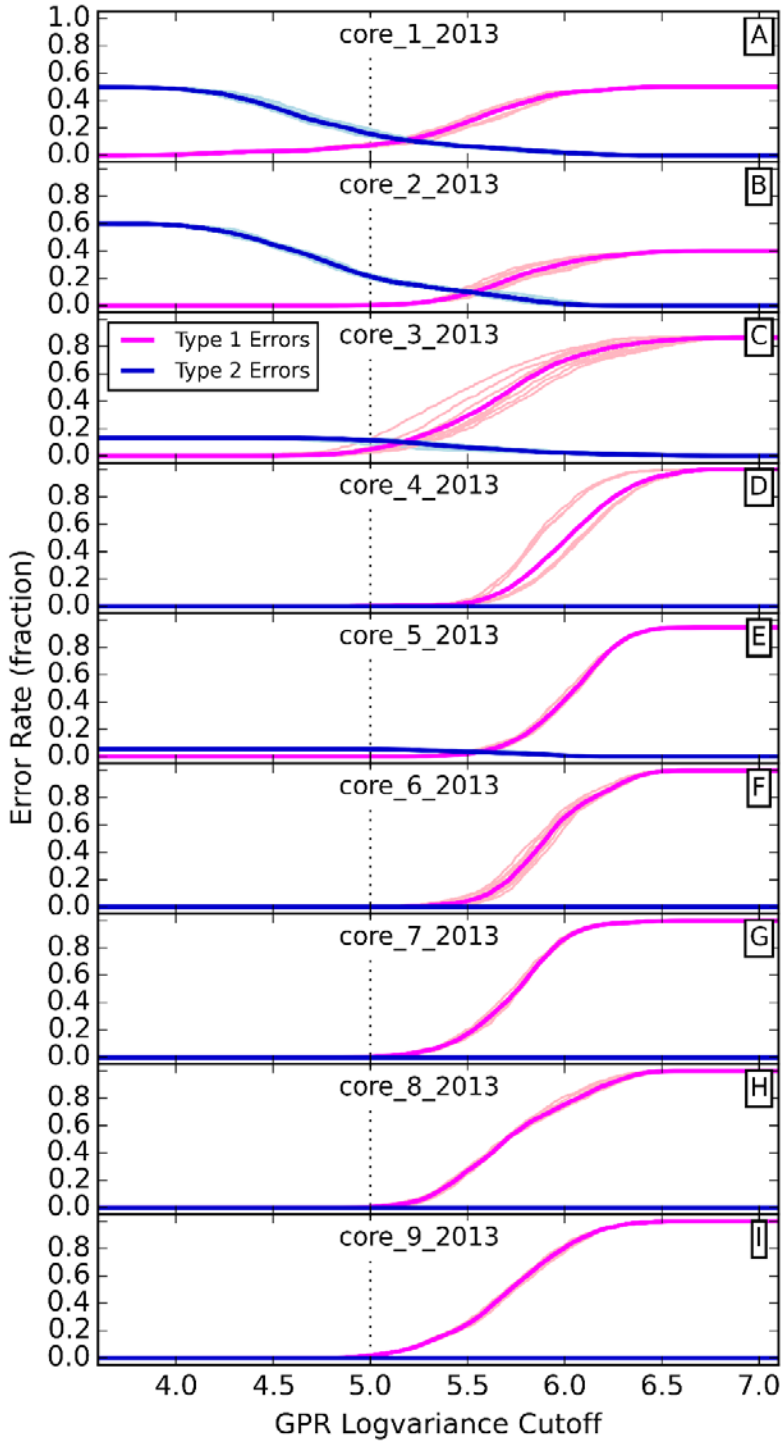

Figure 26 | Error distributions in each ACT-13 core (A-I) as a function of GPR sensitivity cutoff. Type 1 (false positive) errors in magenta, Type 2 (false negative) errors in blue. Lighter lines plot each GPR trace, while bold lines are the mean error.

3.2.4 IceBridge Accumulation Radar

IceBridge Accumulation Radar (AR) data for the years 2010-2014 was downloaded from the CReSIS (Center for Remote Sensing of Ice Sheets) FTP site (Leuschen, 2014). IceBridge did not include the AR instrument on their 2015 and -16 flight campaigns, and the 2017 AR data was not available for this study.

IceBridge AR data was converted from raw data files into ice slabs across Greenland with the following processing steps: First, the data was subset across regions in Greenland where ice slabs were likely to possibly exist and organized into "tracks" for further processing (Section 3.2.4.1). Second, the auto-picking of the ice surface was improved and artifacts eliminated to more reliably subset the near-surface firn for study (Section 3.2.4.2). Third, I de-trended the signal with respect to aircraft roll (Section 3.2.4.3). In flights where aircraft roll was not provided, I computed path curvature as a substitute. Fourth, I manually removed buried lakes and other artifacts in the data that would anomalously affect the signal (Section 3.2.4.4). Fifth, I de-trended each track for signal attenuation at depth, and simultaneously normalized the data so that tracks could be directly inter-compared (Section 3.2.4.5). Sixth, I thresholded the data to pick out ice slabs that most closely matched those detected with *in situ* GPR, and filtered out noise in the signal (Section 3.2.4.6). The IceBridge AR tracks could then be used to map ice slabs across Greenland.

3.2.4.1 IceBridge file organization

IceBridge AR data are separated into flight lines, each of which is separated into multiple files. The files contain a 2-dimensional array of raw GPR signals along with meta-data arrays

containing GPS time of each trace, radar travel time of each sample, position and orientation of the aircraft, and auto-picked surface and other variables useful for post-processing.

Each IceBridge AR flight line is separated into multiple files which I manually subset for the remainder of the work. AR files located entirely outside the boundaries of the Greenland ice sheet and peripheral glaciers were excluded according to the Greenland Ice Mapping Project (GIMP) land-classification mask (Howat et al., 2014). I excluded files located entirely in the Greenland's long-term ablation zone (where no firn exists) and dry-snow areas in Greenland interior (<1 cm a^{-1} melt) where ice layers would not form, according to the HIRHAM5 regional climate model (Langen et al., 2017). Remaining files were manually filtered to eliminate files with extremely poor data quality where no surface returns were identified or the data were otherwise unusable.

After filtering, remaining AR files were grouped into "tracks." I combined adjacent files in a single AR flight line to form continuous transects. Tracks were named similarly to the convention used in the original AR data: "YYYYMMDD_NN_AAA_BBB", where "YYYYMMDD" is the Gregorian calendar date (Year, Month, Day) of the AR flight line, "NN" is the identifier of that flight line on a given day (typically "01", up to "05"), and "AAA" and "BBB" are the file numbers used within that flight line. Tracks ranged in length from 1 AR file to 17 files, spanning between 19.5 and 367 km in length per track. The dataset used here contained 320 tracks consisting of 892 original AR files. The tracks overfly a total 19,096 km of Greenland's accumulation zone.

We applied a $\log_{10}$ transformation to the AR radar files to translate the raw signal into decibels, which was used for the remainder of processing.

3.2.4.2 Surface picking and filtering

AR files come with auto-selected surface returns in the radar file. Although many of these auto-picked returns are sufficient to visually inspect the data, a significant number of artifacts and incorrectly-identified surfaces remained in the provided data (Figure 27-B). To improve selecting the "true" physical surface, I relied upon two assumptions. First, the radar signal at the surface is a very bright reflector (large signal) compared to the relatively weak return from the atmosphere and deep firn/ice. Second, the surface of the ice sheet in the interior accumulation zone is relatively smooth. IceBridge AR traces are spaced approximately 17-20 m apart, and do not contain large jumps in elevation between individual traces within the interior of the ice sheet.

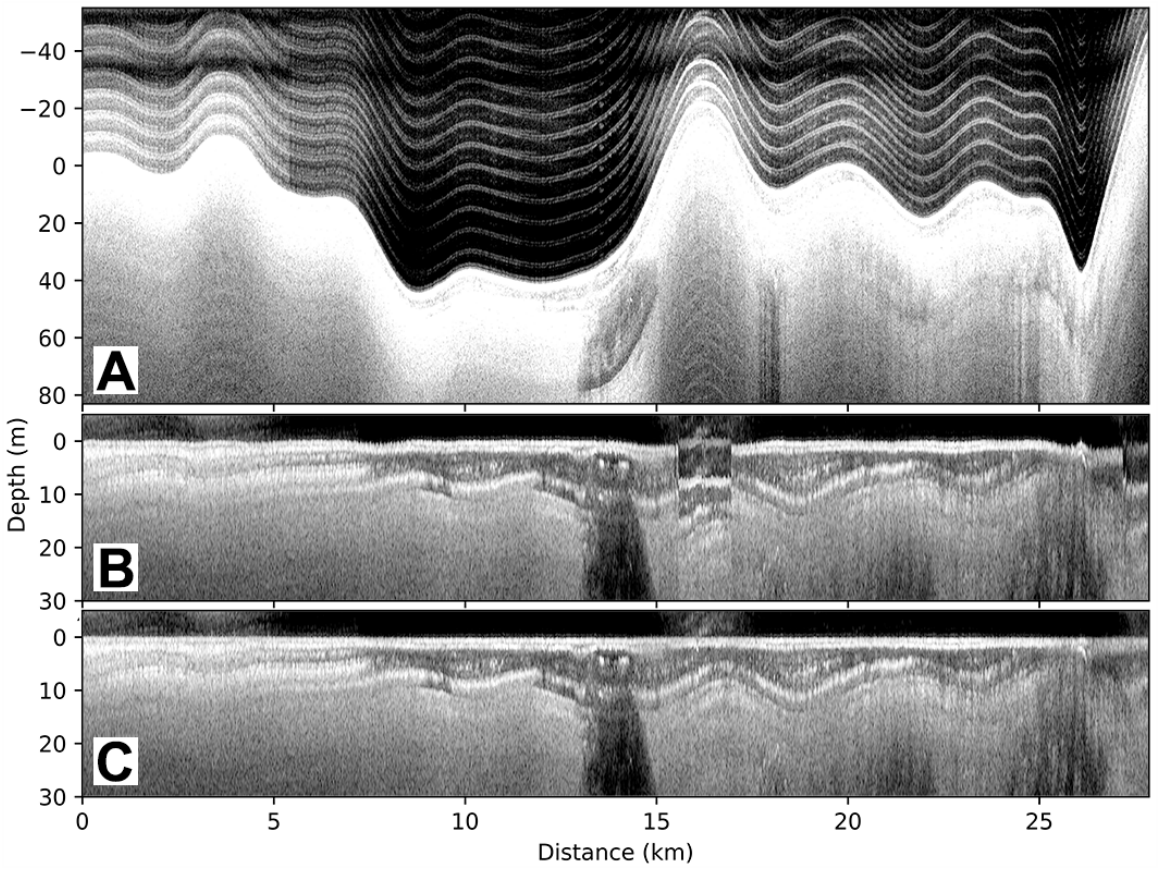

Figure 27 | (A) A raw segment of IceBridge AR track "20110329_04_001_002," with an undulating surface and radar echoes visible above. (B) GPR surface using automated surface picks provided with the OIB AR data. (C) Improved surface picks using mask thresholding and surface-continuity corrections.

Using a vertical pixel range of y-values of [-50,50], I created a 3-standard-deviation pseudo-Gaussian kernel κ(y) (Equations 8-9, Figure 28). The Gaussian function is inverted at the surface with a sign-function S(y) in order to identify signals that are weak in the atmosphere, anomalously strong at the surface, and get gradually weaker beneath the surface with depth. This kernel, when multiplied over 100 vertical pixels in the GPR and summed, would reach its maximum value when centered over the "bright" reflection from the near-surface firn, dark atmosphere above, and dimming surface returns at depth.

$$\kappa(y) = e^{\left[\frac{\left(\frac{y-\mu}{\sigma}\right)^2}{2}\right]} \times S(y) \tag{8}$$

$$S(y) = \begin{cases} -1, & y < 0 \\ +3, & y \geq 0 \end{cases} \tag{9}$$

$$y = [-50, 50],\ \sigma = \frac{50}{3},\ \mu = 0$$

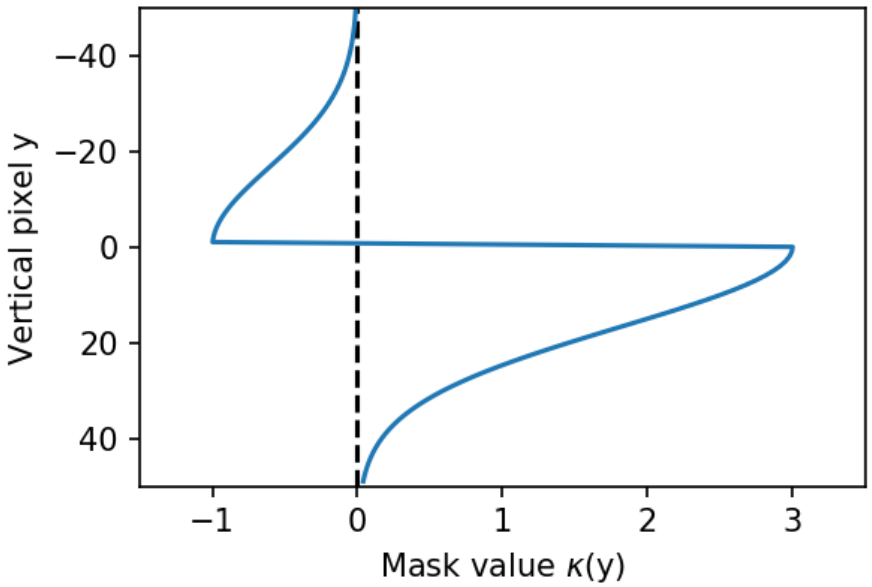

Figure 28 | Surface-identifying kernel used for selecting the ice sheet surface.

The 100-pixel kernel κ(y) was applied to a moving window 150 pixels above and below the suggested surface in each AR track. By visual inspection, we found the true physical surface of the first trace in the file was correctly identified within this search window in all but eight (8) of the 320 AR tracks. In these eight tracks (Table 1), the suggested starting surface was more than 50 pixels away from the correct surface, usually because it was falsely-placed on an "echo" return somewhere above or below the true surface. Initial "suggestion" sample-numbers for these eight files were selected in the AR file in order to begin searching for the surface and correctly

pick the first-trace surface in each AR track. Relying upon the second assumption of relative surface continuity, the search window for the next surface trace was centered at the previous selected surface location and the search was performed again, with the process repeated until the end of the track.

Table 1 | Suggested vertical pixel locations for surface searching in tracks which the auto-picker was unsuccessful in identifying the initial surface.

AR Track	Suggested starting surface pixel, vertical location
20120330_01_025_026	2936
20130419_01_004_005	1850
20130423_01_002_003	1426
20130423_01_069_069	1678
20130423_01_125_125	1755
20130423_01_127_127	1676
20130423_01_130_132	1623
20130426_01_006_007	2234

Upon visual inspection, the kernel successfully identified the snow surface in the majority of GPR traces (> 99 %) in the majority of tracks. Some AR files contained significant echoes in the GPR data (Figure 27-A), and the selections using the kernel occasionally caused a “choppy” uneven surface, which violates the second assumption described above. Jump artifacts were typically short-lived (≤ 20 traces) before returning to the correct surface. To automatically detect where jumps occurred, I calculated the linear slope of the surface from elevations of the 10 traces (~200 m) preceding each trace and calculated whether the surface slope to the next trace was more than 5 vertical pixels (1.5-2.5 m) above or below what would be expected if the surface trend continued along the same slope as before. Pixels up to 20 pixels ahead were searched to find an identified surface whose elevation was consistent to the expected elevation within ±10 % of the prior slope. If such a pixel was found, I linearly interpolated the surface over the gap.

Approximately 0.72% of surface traces pixels were corrected in this manner. Remaining artifacts were identified and masked out from further processing, accounting for 0.38 % of GPR traces being omitted.

3.2.4.3 Roll/Curvature correction

IceBridge AR radar returns are affected by roll of the aircraft. When the instrument is pointed off-nadir the signal echo is deflected away from the aircraft rather than back to the antenna. This can weaken the signal dramatically if unaccounted for (Figure 29-A, dark vertical spans). The correlation between radar return strength and aircraft roll was computed to correct the strength of the AR data for aircraft roll. The magnitude of this weakening depends upon aircraft altitude, elevation, initial signal strength, aircraft and instrument configurations. All of these factors vary between years of the IceBridge mission and even between individual flight lines. To correct for this effect, I computed roll-dependent signal strength on each flight line individually.

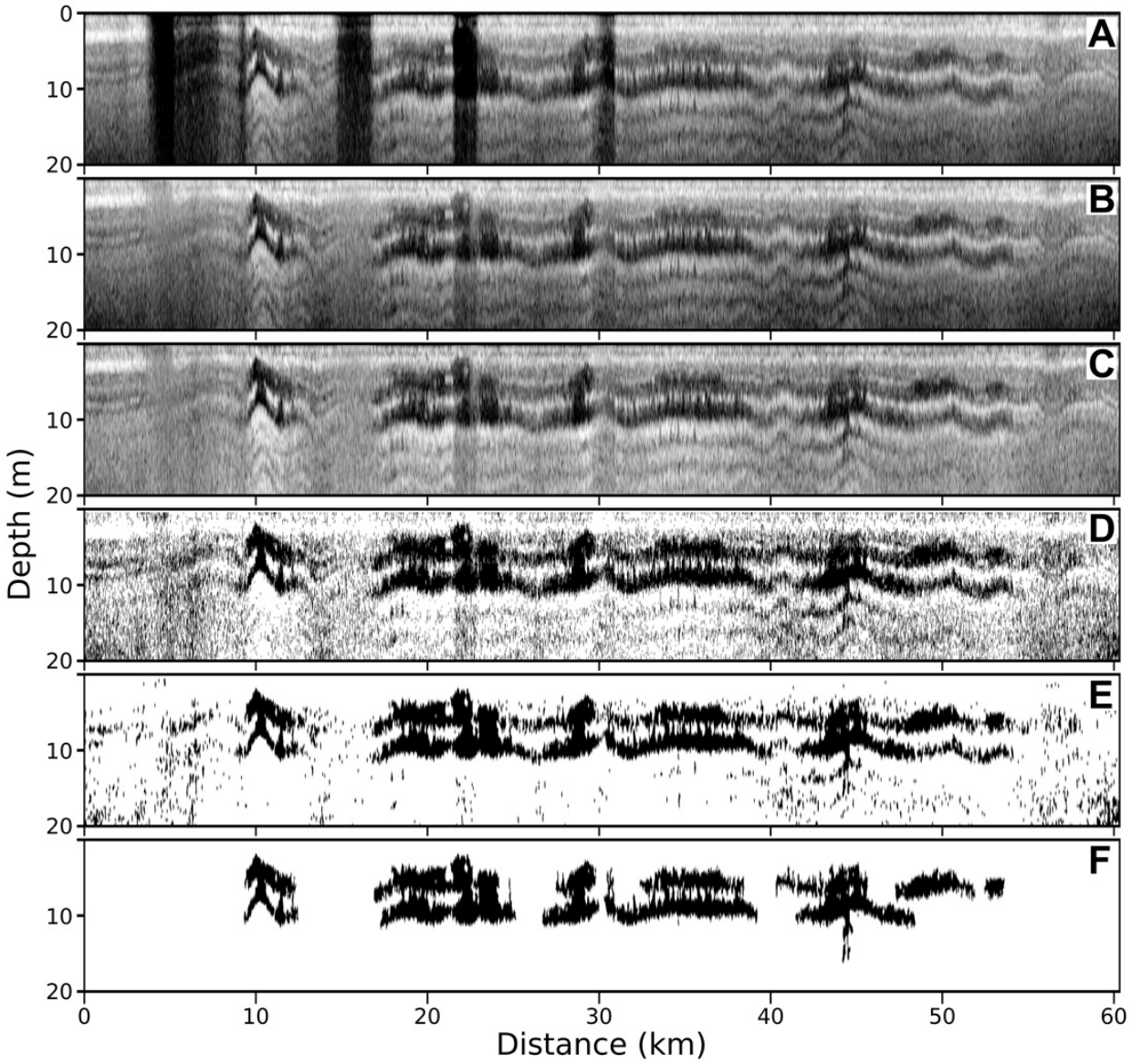

Figure 29 | Flight line 20110406_01_144_146. (A) After surface picking, before correcting for aircraft roll, (B) after correcting for aircraft roll, (C) after correcting for depth attenuation, (D) after initial thresholding to identify dark regions of the image, (E) after initial noise filtering, and (F) after isolating large continuous segments of ≥350 pixels. The dark regions in panel F are identified as ice layers.

Roll-dependent weakening of the signal also depends upon the depth below the physical surface.

Since radar signals attenuate with depth, samples approach background noise if deep enough

below the surface, where it doesn't matter whether the antenna is pointed at nadir or away from the ground. The relative strength of the signal at depth is affected less by aircraft roll than stronger samples collected nearer the surface. A depth-dependent roll correction is necessary to avoid over-correcting signals at depth.

Mean signal strength (Ω) was written computed as a function of aircraft roll (Θ) using a pair of depth-dependent parameter function (*y*) with a quadratic formula. The values A(y) and C(y) are constrained to be negative because the signal decays (does not grow) at higher roll values, and all signal strength values are negative. The parabola is horizontally centered at zero, hence no B term exists.

$$\Omega(\Theta, y) = A(y) \cdot \Theta^2 + C(y) \quad (10)$$

For each flight line, the functions A(y) and C(y) are independently computed as exponential decay functions of depth (y), in meters:

$$A(y) = Re^{Sy} \quad (11)$$

$$C(y) = Te^{Uy} + V \quad (12)$$

At greater depths, A(y) approaches zero and C(y) approaches a constant signal strength, making the Ω(Θ,y) correction function approach a constant (i.e. no correction) with depth. This results in deeper signals being less corrected than shallower signals (Figure 29-B). Best-fit curves were found to determine the R, S, T, U, and V values for roll correction for each flight line (Figure 30

for sample track 20110406_01_144_146). The R, S, T, U and V parameters chosen for every individual flight line are shown in APPENDIX A (Table A1).

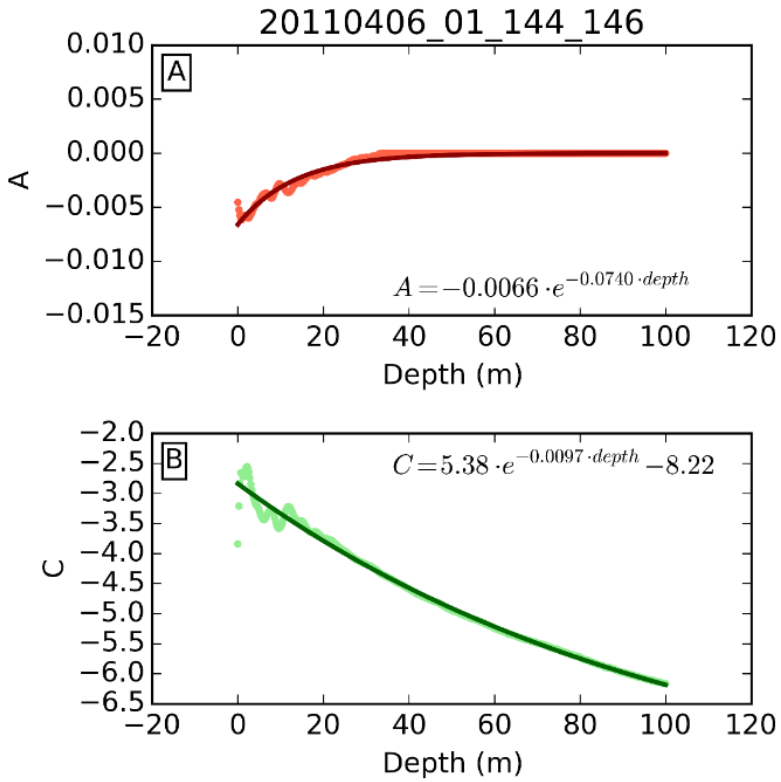

Figure 30 | Depth-dependent roll functions A(y) and C(y) (panels A-B, respectively), calculated for flight line 20110406_01_144_146, with best-fit curves plotted on top.

Functions A(y) and C(y) were calculated in equations (11) and (12) and used in a correction function to convert raw GPR samples (Ω_{raw}) to roll-corrected samples ($\Omega_{corrected}$):

$$\Omega_{corrected}(\Theta, y) = \Omega_{raw} \cdot \frac{C(y)}{A(y) \cdot \Theta^2 + C(y)} \quad (13)$$

When roll (Θ) is zero, traces are multiplied by 1.0 (not adjusted). Since A(y) and C(y) are both negative values, the adjustments increase as aircraft roll (Θ) increases. The adjustment progressively decays to 1.0 at greater depth (y), providing no adjustment to the weaker signals at depth where the signal is less affected by aircraft roll. Figure 31 illustrates this correction applied to the same track shown in Figure 29 (20110406_01_144_146). This track includes several instances when the aircraft rolls by 15-20°, weakening the signal significantly. The correction function removes the weakening of the signal caused by aircraft roll.

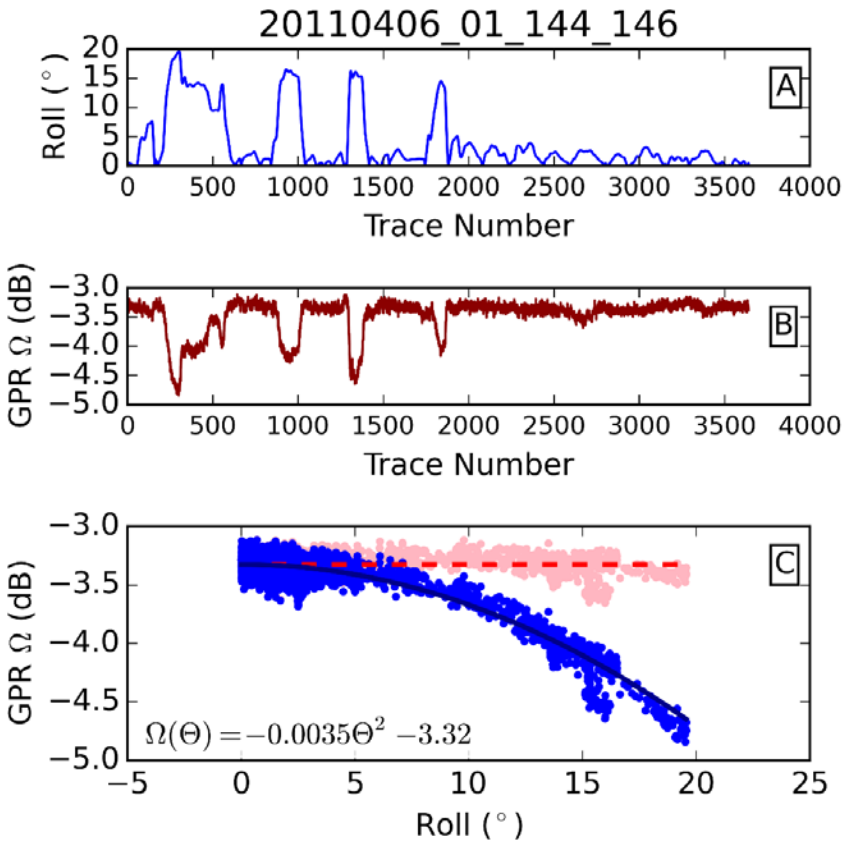

Figure 31 | (A) Roll of the aircraft along flight line 20110406_01_144_146. (B) Average GPR signal strength within the top 20 meters of firn along the same line. (C) Aircraft roll versus mean signal strength of the top 20 meters firn, with quadratic trend lines through the pre-corrected traces (blue) and post-corrected traces (red). The inset formula is uses the mean A and C parameters computed for the top 20 meters of firn.

Roll of the aircraft is included within most AR data files. In one year (2012) aircraft roll data was omitted from the AR data. To account for this missing data field, curvature of the flight path on the ground was substituted for roll of the aircraft on the assumption that for high rolls angles the aircraft typically tilts in the direction it is turning. Path curvature was computed from the coordinates of each AR trace using vector algebra. Trace locations were converted to NSIDC North Polar Stereographic Projection (EPSG: 3413), and vectors V_i were computed between each trace (Figure 32 and Eqs. (14 & (15).

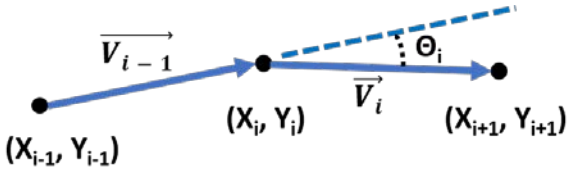

Figure 32 | Schematic diagram for computing aircraft path curvature Θ_i.

$$\vec{V_i} = (X_{i+1} - X_i\,,\quad Y_{i+1} - Y_i) \tag{14}$$

$$\Theta_i = \cos^{-1}\left(\frac{\overrightarrow{V_{i-1}} \cdot \vec{V_i}}{\left|\overrightarrow{V_{i-1}}\right| * \left|\vec{V_i}\right|}\right) \tag{15}$$

IceBridge AR signal strength is weakened most when the roll of the aircraft is greater than 5°. The correlation between aircraft roll and path curvature is high ($R^2 = 0.85$, $p \leq 10^{-7}$) when roll values are greater than 5° (Figure 33). In regions of low roll (≤ 5°) the two variables show little correlation. In years when aircraft roll was unavailable (2012), path curvature was substituted. Since roll corrections are

computed separately for each flight line, it was unnecessary to explicitly convert between roll and curvature when correcting the data. The low correlation between roll and curvature at low roll-angles is not a major concern because the signal is not corrected strongly (<1 %) when the roll is low.

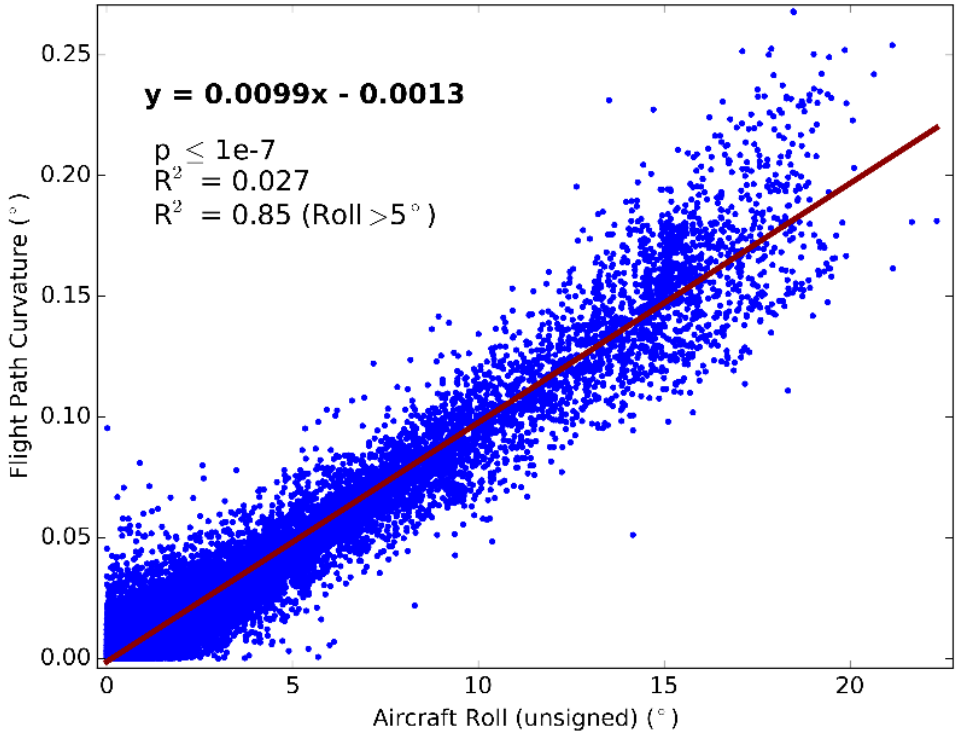

Figure 33 | Correlation between aircraft roll and aircraft path curvature.

Figure 29-A and Figure 29-B illustrate the effect of this roll-correction on the GPR data. Roll corrections were identically applied to each flight line individually. When aircraft roll is minimal (≤ 5°), flight lines were adjusted only slightly, by an average factor of 0.30 ± 0.52 %. When aircraft roll was greater than 5°, signals were strengthened by a mean factor of 5.5 ± 5.6 %.

3.2.4.4 Removing buried lakes and other artifacts

Surface lakes in which some water remains unfrozen through the winter create anomalous radar backscatter signatures, which appear in the IceBridge AR data as extremely bright shallow reflectors with a total extinction of the signal beneath the liquid water (Koenig et al., 2015). To correct the AR signals for depth attenuation, 113 instances of lakes in the AR data were hand-picked and removed from the flight lines in further processing steps. Additionally, I hand-filtered a small number of additional anomalously weak signals (<0.1% of the data), the cause for which was not identified, and removed them from the data set to provide the most consistent returns possible.

3.2.4.5 Depth correction and normalization

AR return signals in firn and ice get exponentially weaker with depth, consistent with Beer's Law for electromagnetic waves attenuating through a medium (Jol, 2008). To de-trend the radar signal with respect to depth, a scatterplot of the top 100 meters in each flight line was fit to an exponential decay curve (Equation (16, and Figure 34 for example track 20110416_01_144_146):

$$\Omega(y) = Ae^{By} + C \tag{16}$$

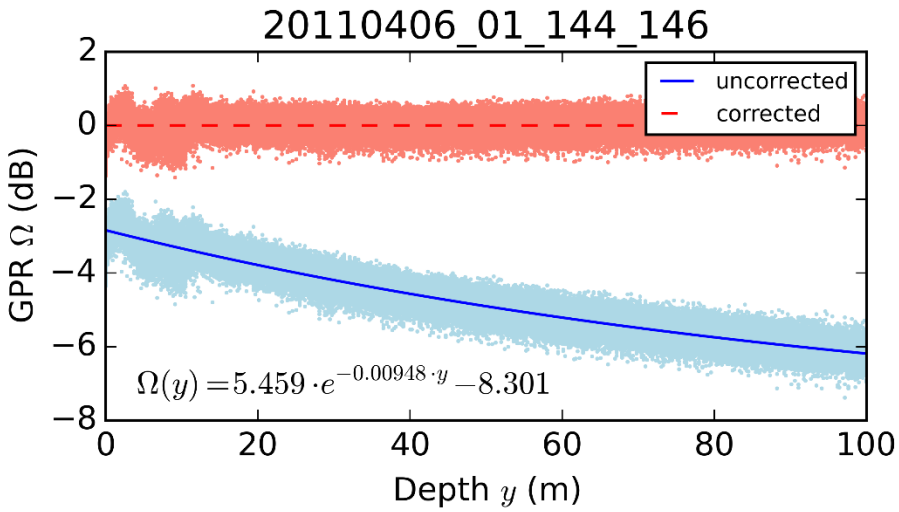

Figure 34 | Depth-correction curve fit, correction and normalization results on OIB flight line 20110406_01_144_146. Blue signals show the original uncorrected data, and the red signal shows data corrected and normalized using Equation (17.

Factors B and C are both constrained to be negative when fitting the curve (the signal will decay at depth, not strengthen, and all values thus far are negative). Ω(y) is the mean strength of the signal at depth y (in meters), the data is corrected for depth using the best-fit values for A, B and C derived from Equation (16, which centers the data around the zero value in Equation (17:

$$\Omega_{depth\_normalized}(y) = \frac{\Omega(y) - C}{A} - e^{-By} \tag{17}$$

The data is then divided by the standard deviation of the entire track data in order to normalize every flight line to a consistent scale, with a mean of zero and a standard deviation of one, allowing us to process the data consistently across all IceBridge AR tracks. The effects of this depth-correction and normalization are shown in Figure 29-C.

3.2.4.6 Thresholding and continuity filtering

After correcting AR data for aircraft roll, penetration depth and removing anomalous artifacts such as lakes, the data was sufficiently pre-processed to select ice slabs. The relatively low resolution of the AR data (approximately 20 m horizontally and 0.25-0.50 m vertically) effectively prevents adopting a "local variance" technique used in the higher-resolution *in situ* radar (Section 3.2.3.2). The AR radar scatters signals back to the antenna less strongly inside solid ice slabs than in more porous firn. In the presence of refrozen ice layers >2x the vertical resolution of the radar, it is possible to pick out LPISs from return strength alone if noise can be effectively filtered from the signal.

I down-sampled the *in situ* GPR processed in Section 3.2.3 to the same horizontal and vertical grid-spacing as the IceBridge AR reference track 20130409_01_010_012, which was flown 2-3 weeks prior on the same line as the *in situ* radar. The AR flight line and the *in situ* GPR are separated by an average of only 17 m, with 99% of the *in situ* radar signals falling within 150 meters cross-track distance from the AR flight line. Each pixel in the down-sampled *in situ* track was assigned a boolean value ("ice" or "no ice") based on a majority of *in situ* pixels that fell within it. This "idealized" down-sampled *in situ* radar dataset was used to validate the IceBridge AR flight line.

In the normalized AR data, the radar signal is less reflected when traveling through ice slabs than through snow and porous firn. We use a three-step process to convert normalized IceBridge AR data into boolean ("ice"/"no ice") values. First, I identified "weak" pixels with signal strength beneath a sensitivity cutoff value (Figure 29-D). I then applied a simple image-processing

technique to filter out small-scale noise (1-2 pixels wide) from the data (Figure 35). This algorithm removes small scale pixel noise from the image while preserving large areas of dark pixels (Figure 29-E).

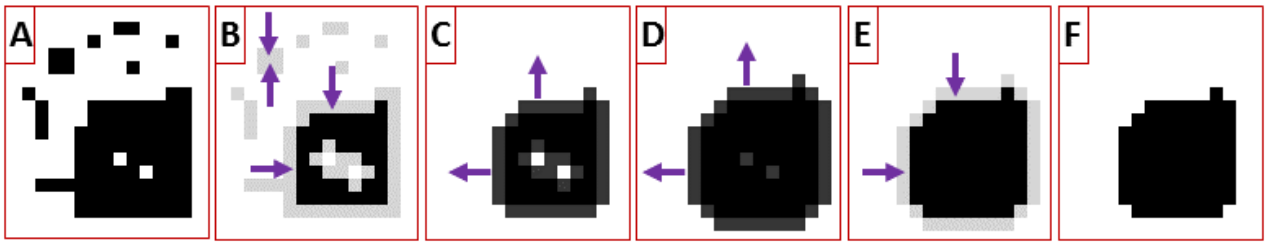

Figure 35 | Schematic illustration of small-scale noise filtering algorithm. (A) The original picture with noise, (B) shrink edges by 1 pixel to eliminate single-pixel assignments, (C) re-grow edges by 1 pixel to their original size, (D) grow edges by one pixel to eliminate single-pixel omissions, (E) shrink pixels back to original size, (F) final product, with small-scale noise removed.

Knowing that ice slabs are both thick and relatively continuous (extending for kilometers), I then applied a "continuity threshold" to only choose regions of the image that are spatially connected to other identified pixels for N continuous pixels (Figure 29-F).

Two thresholds were needed to perform this work: a sensitivity threshold for converting signal strength to ice/no-ice, and a continuity threshold for keeping "continuous" sections of ice and filtering out discontinuous sections that may just be noise. An error-minimization search was used within a range of 41 sensitivity cutoffs (-1.5 to +0.5, by 0.05) and 46 continuity filter cutoffs (0 to 450 pixels, by 10). Ice lenses were calculated using each unique set of cutoffs. False positive (Type-1) and false-negative (Type-2) errors were measured against the down-sampled *in situ* GPR (Figure 36). A minimum combined error of 21.4 % (0.214) is reached when using a normalized GPR sensitivity cutoff of -0.45 dB and continuity cutoff of 350 pixels. Compared to

in-situ GPR, this gives the IceBridge GPR processing an error rate of -16.5% to +4.95% for identifying ice slabs.

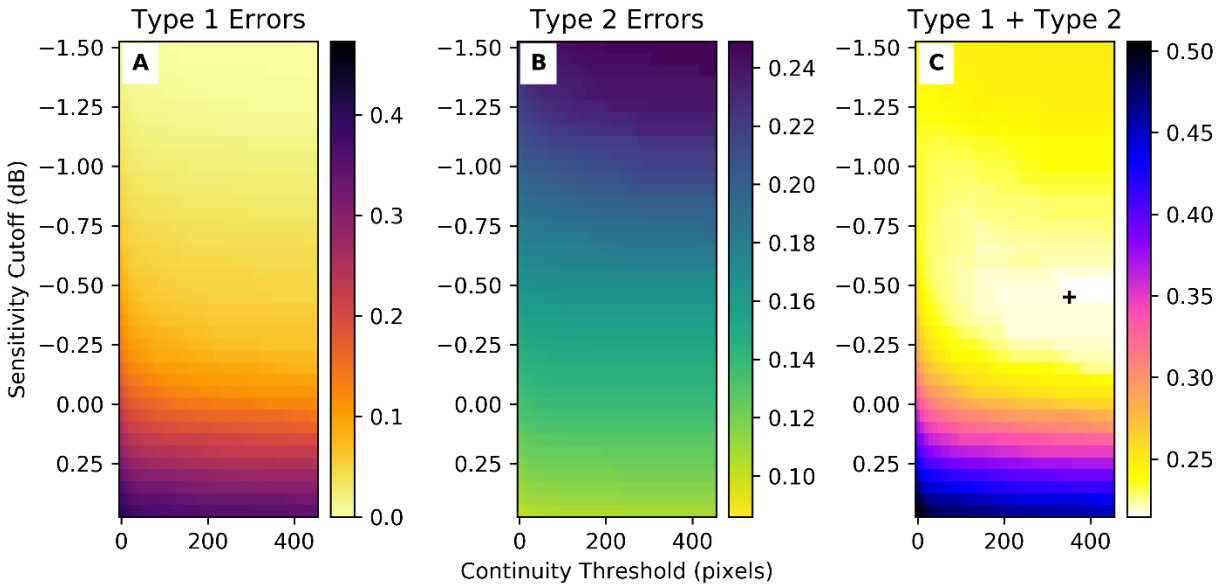

Figure 36 | IceBridge Reference track 2013040901_010_012 error rates compared with resampled *in situ* GPR as a function of continuity thresholds and radar sensitivity cutoffs. (A) Type 1 errors, (B) Type 2 errors, and (C) combined errors (Type 1 + Type 2). The minimum combined error value of 0.214 at (350, -0.45) is identified in panel (C).

Ice layers <1 m thick were omitted from the final dataset for not meeting the definition of "ice slabs" outlined early in this chapter. These layers <1 m are often virtually indistinguishable from noise in the AR files. Areas where ice slabs were >16 m in the top 20 m of firn were omitted as being indistinguishable from regions of solid ablation ice where small pockets of firn or other reflectors may cause false positives for ice-slab identification. Regions with solid ice between 1-16 m in the top 20 meters of firn, with firn at the bottom of the radar slice, were identified at "ice slabs."

3.3 Results

Ice layers ≥50 cm thick were identified with *in situ* radar at a -13.2 to +3.20 % error rate compared ice layers identified in adjacent cores. Ice slabs in IceBridge AR data were identified at a -16.5 to +4.95 % error rate compared to *in situ* radar. In both cases, ice was generally under-identified in the radar. Combining these two uncertainties, we estimate the IceBridge AR data detects ice slabs -21.1 to +5.89 % error rate. False positive values may occur in the data, but are generally less common than false-negative errors, where ice slabs actually exist in the ground that are not detected by the radar. These uncertainty estimates apply to straight-line tracks only, and ice is likely to be underestimated more along segments of tracks where the aircraft was turning. Figure 29-B illustrates that although roll corrections can improve the strength of signals affected by aircraft roll, they do not inherently improve the signal-to-noise ratio in radar returns weakened by roll. Few if any ice slabs were detected in strongly roll-corrected signals, even in areas where they may exist if a core were drilled along the flight line.

An uphill transect of *in situ* ground penetrating radar (GPR) in southwest Greenland shows LPISs begin at approximately 1690 m elevation along the main GPR transect (Figure 37). These LPISs caused slush fields to appear on the surface as high as 1850 m a.s.l. in the summer 2012 (the “KAN-U” field site), approximately 22 km upslope from the long-term saturation identified in the GPR, where ice is seen for the entire depth that can be detected the GPR signal.

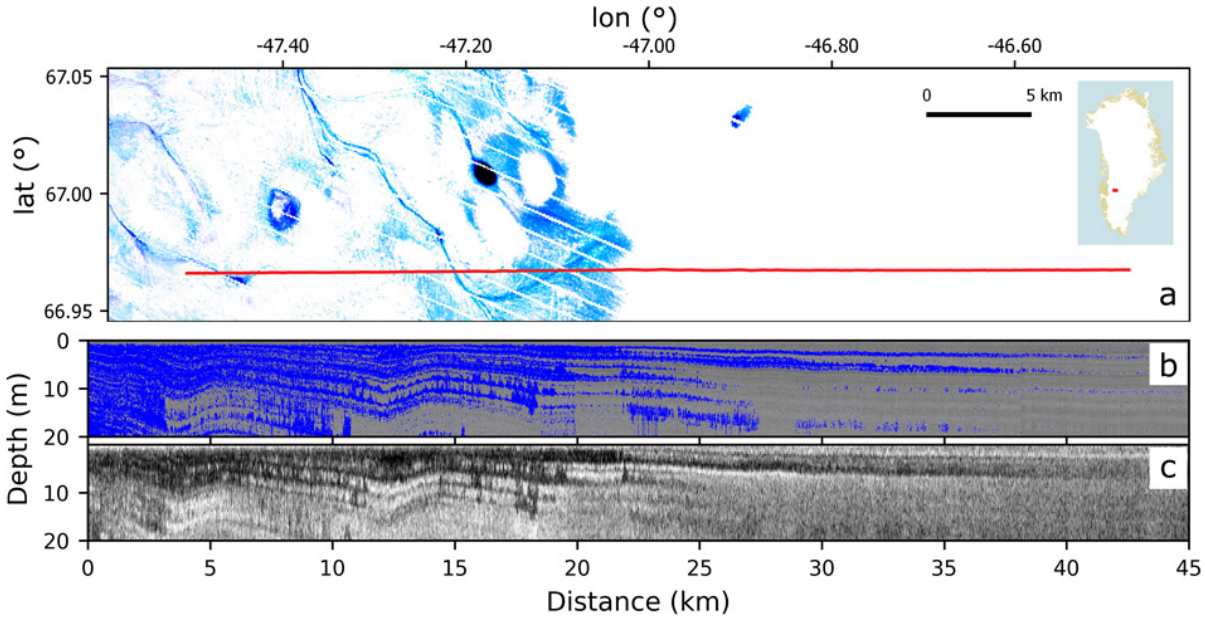

Figure 37 | (a) ACT-13 transect path (red), with a Landsat-7 image from July 16, 2012 (contrast-enhanced). (b) ACT-13 *in situ* GPR with ice layers in blue. (c) IceBridge AR radar.

The automated algorithm used to select LPISs using IceBridge AR data slightly underestimates total ice content, omitting thin or non-continuous sections in post-processing. However, it reliably identifies ice slabs greater than one meter thick and spanning more than one kilometer horizontally in regions where the signal is not negatively affected by adverse collection conditions such as excessive aircraft pitch/roll or poor weather. A map of ice slab thickness in Greenland using this algorithm (Figure 38) should be interpreted as a “minimum observed extent” of LPISs in Greenland rather than an exhaustive map.

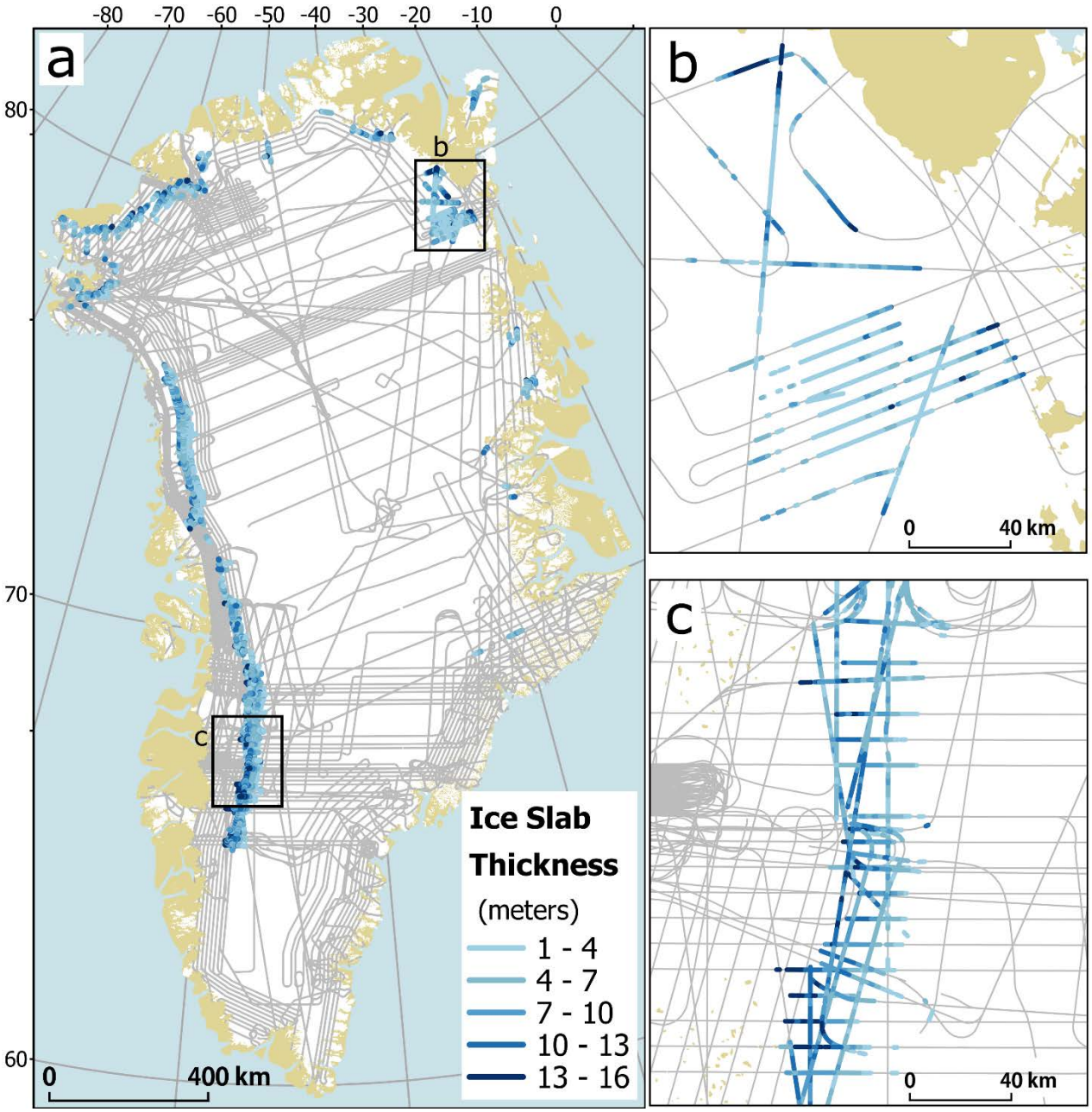

Figure 38 | (a) Low-Permeability Ice Slabs on the Greenland ice sheet and peripheral ice caps detected with IceBridge Accumulation Radar data. Tan areas indicate bare land on Greenland's periphery, and grey lines are all IceBridge flight lines over the ice sheet, with shades of blue indicating thickness of detected ice slabs. (b) Inset over southwest Greenland. (c) Inset over northeast Greenland.

Drawing simple bounding polygons around the groups of AR tracks where ice slabs have been identified, the areas where LPISs are directly observed (Figure 38) cover approximately 69,400

km^2 of Greenland's lower accumulation zone. Coverage gaps exist in several areas of the ice sheet where LPISs may still exist, notably in far southwest Greenland's lower accumulation zone below 65° latitude, mountainous regions of central-east Greenland, and margins along the north coast adjacent to the Arctic Ocean. LPISs do not appear in regions of high generally high accumulation such as SE Greenland, which will be discussed in greater detail in the next chapter.

3.4 Discussion

Figure 38 is the first map of its kind with direct observations of wide scale refreezing in Greenland's accumulation zone. Since ice slabs exist exclusively atop firn in areas immediately uphill from the long-term runoff zone, this data both maps the current extent of ice slabs and the potential uphill migration of the runoff zone in Greenland.

The map shows that near-surface saturation of firn is not a localized phenomenon, not a niche process isolated solely to one location in southwest Greenland. Already covering almost 5% of Greenland's ice, it represents a wide-scale change in the hydrology of the Greenland ice sheet. Ice slabs are known to occur over the top of more porous firn, which reveals a history of change. If the areas where ice slabs exist now had always received this much melt, the pore space at depth would have been long filled, and the area would simply be a map of Greenland's long-term saturation zone. Firn existing at depth, while the surface is dominated by refrozen ice enough that near-surface pore space has been eliminated, is direct evidence of climate changing in Greenland's high elevations. Melt is continuing to trend upward across the ice sheet enough that even Summit Camp may lose its designation as a "dry snow zone" in the coming decades if the current pace of warming continues (McGrath et al., 2013).

By revisiting modeling studies performed decades ago when widespread warming in Greenland was being seriously considered (Pfeffer et al., 1991) and comparing them with current observations along the K-Transect, it becomes apparent that melt and runoff is likely to be progressing faster than originally thought possible (Figure 39).

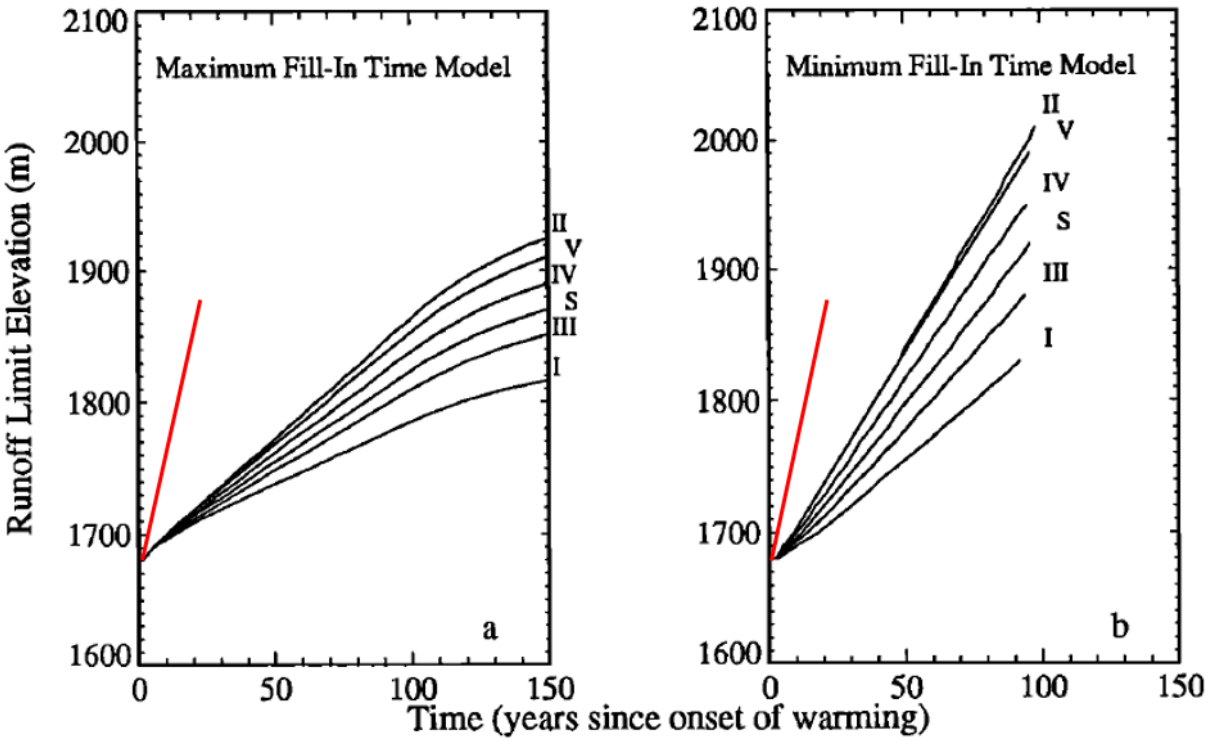

Figure 39 | Runoff elevation predictions in a warming climate, from Pfeffer et al. (1991). The red lines indicate the progression of the runoff zone from the long-term mean of ~1680 m a.s.l. to 1850 m a.s.l. in approximately 20 years (Figure 18). The experiment numbers (Roman numerals) are outlined in Figure 5.

Figure 39 illustrates a first-order comparison between observed runoff extent (red line) and projected extent under various climate warming scenarios. The red line indicates the runoff elevation in the mid-to-late 1990's at approximately 1680 m a.s.l, consistent with models

(Fettweis et al., 2013; van den Broeke et al., 2016), our own GPR measurements of firn stratigraphy in southwest Greenland (Figure 37), and optical satellite observations (Figure 18). Within approximately 20 years or less, the runoff line jumped to above 1850 m a.s.l. and possibly as high as 1900 m (Machguth et al., 2016). The previous modeling studies indicated it would take at least 50-100 years for runoff to expand that high, even under worst-case scenarios. Caution should be taken with such direct comparisons though, since Pfeffer et al. (1991) were looking at average values across all of Greenland and not solely the K-transect in southwest Greenland. Additionally, Figure 39 was originally meant to consider the average runoff elevation, and not solely the runoff line in extreme melt years such as 2012. The trend seen in optical imagery indicates that the runoff line is regularly seen as high as 1800 m a.s.l. along the K-transect even in non-extreme years (Figure 18, Machguth et al., 2016). Further study is needed to perform a more robust comparison between prior modeling and current observations. But the observational data suggests that the runoff line according to observations is migrating uphill more rapidly than prior modeling suggested. The LPIS feedback is a likely contributor to this phenomenon.

Regional Climate Models (RCMs) have become increasingly sophisticated in their ability to simulate and predict melt across the world's ice sheets and glaciers. If we can isolate the climatological conditions under which LPISs recently formed in Greenland, we should be able to predict their future extent in a warming climate and the possible implications for runoff from the Greenland ice sheet.

4 MODELING AND PREDICTING LOW-PERMEABILITY ICE SLABS ACROSS GREENLAND

4.1 Introduction

Recall from Section 1.3.1 (p. 13) that prior work has identified a threshold of melt to accumulation (M/R) that when exceeded, would force firn to saturate and eventually cause runoff (Pfeffer et al., 1991). The threshold was determined to be approximately 0.67 at the time, largely invariant to reasonable ranges of constants for snow and ice density used in its formulation.

Multi-annual ice slabs can only form when melt has saturated the ability for the local firn layer to store meltwater in available pore space. If the amount of annual snow regularly exceeds the amount of melt that can fill the pore space within it, additional pore space would still available, and pore space would be added to the firn column annually. Ice layers would advect downward into the firn every year, mixed with layers of porous snow and firn, resulting in a stratified wet-snow zone that still contains regular layers of pore space available for future refreezing. Such regular layers of porous firn in the wet snow zone are clearly visible in cores where the saturation threshold has not yet been surpassed (Figure 18, cores 3-6). Pore space is also evident in the deeper portions of cores that have recently saturated with ice slabs closer to the surface (Figure 18 cores 1-2, Figure 19 & Figure 20), indicating that melt exceeding this threshold was a relatively recent phenomenon. Only when melt has regularly exceeded the firn's ability to store and refreeze it can ice layers merge together over wide scales to form widespread thick ice slabs. Runoff that occurs over the top of an ice slab in a warm melt season has exceeded the near-surface snow's ability to store and refreeze it. Quantifying this "excess" of meltwater, and where

it has increased in recent years, is key to understanding where ice slabs have formed today, and where they may be expected to form in the future.

In this chapter I describe a formulation for excess melt that builds upon previous work using the ratio of annual melt to annual accumulation ("M/C") derived by Pfeffer et al. (1991). I combine the IceBridge measurements of ice slabs derived in Chapter 3 combined with Regional Climate Models (RCMs) over Greenland to calculate the amounts of excess melt that have formed low-permeability ice slabs (LPISs) in Greenland. I use RCMs forced by forward-looking General Circulation Models (GCMs) to predict the growth of ice slabs in Greenland through the year 2100 under different greenhouse-gas emission scenarios.

4.2 Methods

4.2.1 Definition of Excess Melt

In this work, "excess melt" specifically describes the quantity of liquid water (melt or rain) in a given year added to the firn column that has *exceeded* the annual snow layer's ability to store and refreeze it. Although rain contributes to total liquid water entering the firn, in areas of Greenland's lower accumulation zone annual melt typically exceeds rain by a factor of ten or more. The term excess melt is used to conceptually simplify this relationship. At the upper limit of the runoff line, where the snow's ability to absorb water has been filled but not exceeded by melt and rain, excess melt is zero.

It is acknowledged that in porous firn, meltwater can percolate deeper than the topmost annual snow layer before refreezing (Humphrey et al., 2012; Charalampidis et al., 2016) even if this

excess melt threshold is not met. However, from a perspective of filling the firn layer and creating ice slabs, it doesn't matter whether excess melt refreezes near the surface or at depth. If, for instance, pore space is filled at 10 m depth rather than 1 m depth, there will still be pore space available at 1-9 m depth which could absorb liquid water. If pore space is still being added annually to the firn column, the ice at the average refreezing depth will be buried annually and a stratified firn layer will exist where porous firn exists between layers of refrozen ice. Only when liquid water routinely exceeds the ability for annual pore space to absorb it will firn eventually fill with multiple years' of refrozen ice annealed together, forming solid ice slabs in lieu of a porous firn layer. For this reason, the average depth of refreezing is not considered in this work. The mean value of excess melt entering the firn column over long time spans is examined closely.

4.2.2 Excess Melt Calculations

Using the formulation from prior work described in Section 1.3.1, Equation (1), I include a term for rain (*R*), which typically increases in a warmer polar environments (Doyle et al., 2015), and can saturate firn in the same way that melt water does. Rain contributes both to overwhelming pore space and refreezing capacity of snow. Here rain is assumed to be at freezing point when entering the snow surface (Equation (18)).

$$M \geq \frac{\mathbb{c}}{L} C \left(T_f - \frac{RL}{\mathbb{c}C} \right) + (C - M - R) \left(\frac{\rho_r - \rho_c}{\rho_c} \right) \tag{18}$$

M is melt, *R* is rain, *C* is snow accumulation. *L* is the latent heat of fusion of ice, and ℂ is the heat capacity of water. T_f is the average firn temperature, in which the average annual 2 m air

temperature is substituted. In place of ρ_{pc} (pore close-off density) used in prior work (Pfeffer et al., 1991) I substitute the density of refrozen ice in firn, ρ_r. *In situ* core measurements show refrozen "bubbly" ice has a higher density of 873±25 kg m^{-3} (Machguth et al., 2016) compared to firn reaching pore close-off through grain deformation alone, typically ~830 kg m^{-3} (Pfeffer et al., 1991; Cuffey & Paterson, 2010). I calculate the density of fresh snow accumulation ($\rho_{c)}$ with a geographically-based parameterization used in firn modeling (Langen et al., 2017) that provides accumulation density values between 300-390 kg m^{-3}, consistent with independent observations (Koenig et al., 2013).

The assumption of rain at entering the snow surface at a temperature of 0 °C is debatable. However, other studies use this same assumption when calculating surface mass balance (Fettweis et al., 2013; Langen et al., 2017; van As et al., 2012). Since rain is a relatively minor factor compared to surface melt, potential errors introduced by this assumption are not likely to significantly bias the results.

Equation (18) refactors into a ratio threshold similar to that seen in Section 1.3.1, Equation (2):

$$\frac{M+R}{C} \geq \left(\frac{\mathbb{C}}{L}T_f + \frac{\rho_r - \rho_c}{\rho_c}\right)\left(1 + \frac{\rho_r - \rho_c}{\rho_c}\right)^{-1} \tag{19}$$

The left side of Equation (19) defines the amount of liquid water generated in the firn column as a ratio of accumulation. The right side calculates the pore space and refreezing capacity that must be overcome to overwhelm the refreezing capacity, again stated as a ratio of total accumulation.

From this I derive "Excess Melt", the quantity of melt water that has exceeded the snow's cold content and pore capacity to absorb it, scaled for annual accumulation, in units of mass per area:

$$Excess\ Melt = \left(\frac{M+R}{C} - \left[\left(\frac{\mathbb{C}}{L}T_f + \frac{\rho_r - \rho_c}{\rho_c}\right)\left(1 + \frac{\rho_r - \rho_c}{\rho_c}\right)^{-1}\right]\right) \cdot C \quad (20)$$

The units $kg\ m^{-2}$ of water mass are functionally equivalent to millimeters water-equivalent (*mm w.e.*). Excess melt is measured in *mm w.e.* for the remainder of this work.

4.2.3 Mapping Current and Future Ice Slabs

I used three different regional climate models: HIRHAM5 (Christensen et al., 2007), MAR 3.5.2 (Fettweis et al., 2013), and RACMO 2.3 (Noël et al., 2015) forced at their boundaries by reanalysis data sets ERA-Interim (Dee et al., 2011) and NCEP version 1 (Kalnay et al., 1996) to determine the historical climate under which ice slabs have formed (Table 2). Reanalysis data sets are short-term global weather models that are corrected against weather station observations at regular time-steps (4- or 6-hours) in order to accurately simulate the global climate over time without drift from internal variability. RCMs over Greenland forced on their boundaries by reanalyses are considered the best "real-world" simulations available for historical melt in Greenland.

Table 2 | Descriptions of reanalysis-forced RCMs used for ice slab modeling.

RCM	Reanalysis Forcing	Years Available
HIRHAM5	ERA-Interim	1980-2014
MAR 3.5.2	ERA-Interim	1979-2014
MAR 3.5.2	NCEPv1	1948-2015
RACMO 2.3	ERA-Interim	1958-2015

To quantify changes in excess melt which have caused ice slabs to form, pixels from each RCM were selected which mapped to locations where ice slabs have been identified in IceBridge radar (Section 3.3, Figure 38). These pixels containing present day low-permeability ice slabs are referred to here as "LPIS pixels." Excess melt is computed annually over LPIS pixels to determine the timing and magnitude by which excess melt has increased in these areas in recent decades. The decade before excess melt began increasing significantly in LPIS pixels is used as a baseline time period, the relative steady-state climate in which new ice slabs would not yet have formed.

To quantify the amount of excess melt which causes ice slabs grow thick enough to be detected in radar, I used a subset of IceBridge AR tracks which cross ice slab regions in "downhill to uphill" orientations, where both the "bottom" (lowest elevation) and "top" (highest-elevation) extent of present-day ice slabs is clearly identified. This list of these AR tracks is available in APPENDIX B. Excess melt was computed in 10-year running means to better capture the average melt conditions and reduced inter-annual variability in the signal. A 10-year mean also computes melt over a long enough period that thick slabs have the ability to form.

For each IceBridge track listed in APPENDIX B, excess melt was totaled for the 10 years preceding the detection of ice slabs along the track at both the lowest elevation of the track (thickest ice slabs) and the highest elevation (thinnest ice slabs detected). An "intermediate" value was also chosen which separated the regions where ice slabs were detected continuously in IceBridge data versus where gaps were identified between LPIS radar detections. These

thresholds were identified for each track using each RCM. The median value of each excess melt for all tracks was computed for each RCM, and the mean of those medians was selected as the overall threshold of excess melt that has resulted in the formation of the upper, intermediate and lower extent of ice slabs across Greenland. Regions whose 10-year mean excess melt exceeded the threshold to form ice slabs were flagged as containing ice slabs. Regions of the ice sheet where enough excess melt to form LPISs had already been observed in the baseline period were identified as belonging to the long-term ablation zone, and were masked out. Only areas where melt has recently increased beyond the threshold necessary to form LPISs after the baseline period were identified as likely containing modern-day LPISs.

Annual snowfall was computed in 10-year running means over LPIS pixels to determine the maximum amount of snowfall in which ice slabs form in Greenland. Areas above this threshold correspond with regions where perennial firn aquifers form instead of ice slabs (Forster et al., 2014; Koenig et al., 2013; Miège et al., 2016). To account for outliers in the accumulation data, the accumulation threshold was chosen at 95^{th} percentile of mean annual accumulation values over LPIS pixels.

To model ice slab extent into the future, the same excess melt thresholds used to map present-day LPIS extent were applied to RCMs forced at their boundaries by global circulation models (GCMs): ECEarth (Hazeleger et al., 2010), CanESM2 (Chylek, et al., 2011), MIROC5 (Watanabe et al., 2010), NorESM1 (Bentsen et al., 2013), and HadGEM2 (Collins et al., 2008) (Table 3). Each GCM begins their simulations with an “historical” period of known greenhouse-gas emissions (typically through 2005 in these models) followed by a forward-looking

representative concentration pathway (RCP) simulating greenhouse gas concentrations through 2100 specified by the coupled-model inter-comparison experiment (IPCC, 2013). RCP 4.5 represents “moderate emissions” where greenhouse gas emissions are leveled off and tapered to zero by the year 2050. The RCP 8.5 “high emissions” pathway assumes annual greenhouse gas emissions continue to increase through 2100.

Table 3 | Regional Climate Model descriptions, forced by GCMs

RCM	GCM Dataset	RCPs	GCM Historical Forcing Years	GCM RCP Forcing Years	LPIS Baseline Years	LPIS Change Years
HIRHAM 5	ECEarth	4.5, 8.5	1991-2010	2031-2050, 2081-2100	1991-2000	2001-2010, 2031-2050, 2081-2100
MAR 3.5.2	CanESM2	4.5, 8.5	1950-2005	2006-2100	1981-1990	1991-2100
MAR 3.5.2	MIROC5	4.5, 8.5	1900-2005	2006-2100	1981-1990	1991-2100
MAR 3.5.2	NorESM1	4.5, 8.5	1950-2005	2006-2100	1981-1990	1991-2100
RACMO 2.1	HadGEM2	4.5	1971-2004	2005-2098	1981-1990	1991-2098

For the HIRHAM5 RCM forced by the ECEarth GCM, data was not available for the 1980-1989 baseline period, and 1990-1999 was used instead, which may bias the results slightly low for that particular model since ice slab formation would begin at a later date even if melt had already begun increasing. For the RACMO2.1 RCM forced by the HadGEM2 GCM, only RCP4.5 results were available. Since RCP8.5 results were unavailable, the RACMO2.1 results were not included in a direct comparison between RCP4.5 and RCP8.5 results.

Ice slabs are identified when excess melt values exceed the mean thresholds identified earlier for ten years or more. The model does not directly simulate the formation of ice slabs themselves, but rather the expansion of the conditions under which ice slabs are known to have formed in

Greenland. When these conditions are met, the assumption is made that an ice slab now exists there.

Once an area has been identified as likely containing an ice slab, the ice slab is assumed to remain unless excess melt decreases enough for a decade or more to begin re-buffering the firn, or accumulation increases enough for a decade or more to turn the area into an aquifer-based hydrologic regime. Areas which first formed ice slabs in the early 21st century may transition into ablation zones by 2100 with the eventual elimination of porous firn at depth, and thus may not be identified as "ice slab areas" if an identical study were performed in the future. Such a transition is not well understood at this time, and we include new ice slab areas permanently in the future-looking totals in order to identify the cumulative growth of ice slab areas over the study period.

4.3 Results

4.3.1 Increases in Excess Melt

RCMs forced by reanalysis data are consistent with each other in the overall trends and inter-annual variability of excess melt (Figure 40). Excess melt values are relatively constant from the beginning of the RCM runs through approximately 1990, and begin to show a marked increase in the 1990s through the mid-2010s. 1980-1990 was chosen as the baseline period for LPIS calculations, while excess melt values from 1990 through 2013, just before the final year of IceBridge data collection in Spring 2014, were used to model the growth of LPISs across Greenland to compare with IceBridge observations.

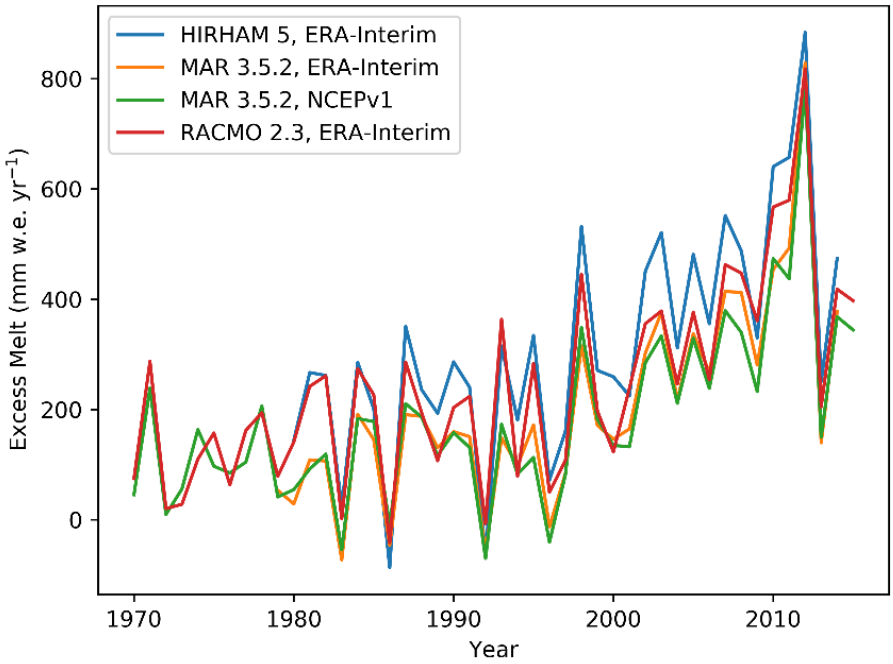

Figure 40 | Excess Melt in RCMs forced by reanalysis data over LPIS pixels, where ice slabs have been identified IceBridge radar data. HIRHAM5 forced by ERA-Interim (blue), MAR 3.5.2 forced by ERA-Interim (orange), MAR 3.5.2 forced by NCEPv1 (green) and RACMO 2.3 forced by ERA-Interim (red). Excess melt was consistent through approximately 1990, increasing through the 2000s and 2010s.

4.3.2 Mapping Current Ice Slab Extent

Excess melt totals for the 2004-2013 decade in LPIS pixels show a good agreement between different RCMs, with the inter-quartile ranges overlapping among nearly all of the different RCMs (Figure 41). The mean values of 573.1, 332.7, and 266.0 mm w.e. are used as the Lower, Upper, and Intermittent Upper values of excess melt where ice slabs to are known to appear in IceBridge AR transects, respectively. The total extent of detected ice slabs appear between the upper intermittent and lower-continuous values, or 266 – 573 mm w.e. for a decade or more, respectively, after masking out baseline areas that received at least that much excess melt annually prior to 1990.

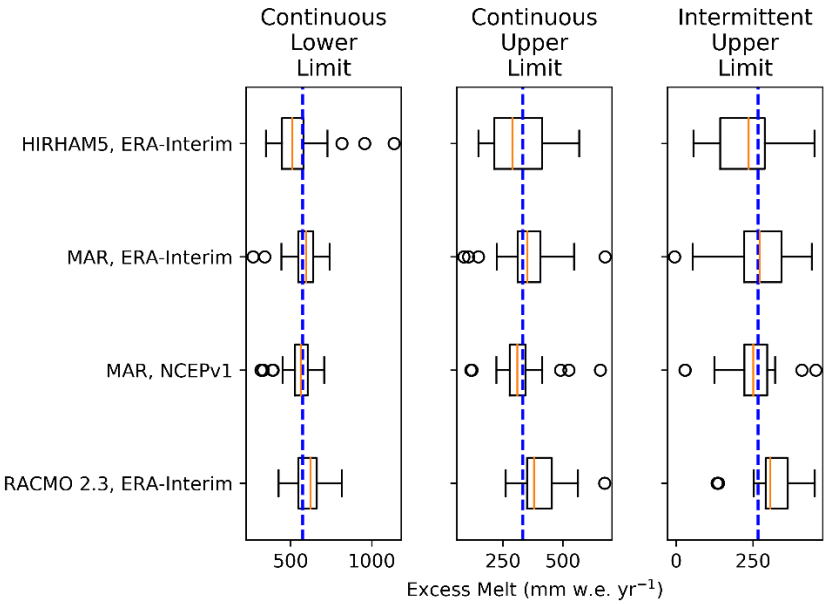

Figure 41 | Excess Melt threshold distributions for the Continuous Lower, Continuous Upper and Intermittent Upper extents of known ice slabs detected over selected IceBridge AR tracks. Each box represents the inter-quartile range of the data with spans representing the full range. Outliers greater than 1.5 inter-quartile ranges from the median are represented with circles. The orange line is the median of each data set. The blue dashed represents the mean value computed for each threshold and used for LPIS modeling.

According to the RCMs, ice slabs have formed in areas with annual accumulations ≤ 572 mm w.e. a^{-1}, or ~1.65-1.8 meters annual snowfall at a 95% confidence threshold. We apply a snow mask for regions with higher annual accumulation rates than this threshold (> 572 mm w.e. a^{-1}) and assume that excess melt in these high-accumulation regions form perennial firn aquifers instead of ice slabs.

RCM models agree that LPIS extent in Greenland remained relatively small or increased only slightly before the year 2000 (Table 4 and Figure 42). Ice slabs grew 284-1270 km^2 a^{-1} in the years 1990-2000, with total ice slab extent between 3400-12,800 km^2 by the year 2000. With the

onset of the highest-intensity melt season in the satellite record (at the time) of 2002 (Steffen et al., 2004), ice slab extent in Greenland began to grow rapidly from 2001-2013 at a rate of 6040-7190 km^2 a^{-1}, with a total LPIS extent of 74,000 - 95,000 km^2 above Greenland's pre-1990 runoff zone by the end of 2013.

Table 4 | RCM LPIS model descriptions and results, forced by Reanalysis data. Statistically insignificant trends are italicized.

RCM	Reanalysis Forcing	LPIS trend (km^2a^{-1}) 1990 – 2000	p-val	R-val	LPIS area (10^3 km^2) 2000	LPIS trend (km^2 a^{-1}) 2001 – 2013	p-val	R-val	LPIS area (10^3 km^2) 2013
HIRHAM5	ERA-Interim	1270	7.01e-05	0.917	11.7	6040	6.78e-09	0.979	82.3
MAR 3.5.2	ERA-Interim	652	3.59e-04	0.880	6.7	7190	1.53e-11	0.993	89.7
MAR 3.5.2	NCEPv1	*284*	*5.30e-02*	*0.596*	*3.4*	6070	1.76e-11	0.993	74.3
RACMO 2.3	ERA-Interim	1230	7.19e-04	0.858	12.8	7190	9.48e-10	0.985	95.0

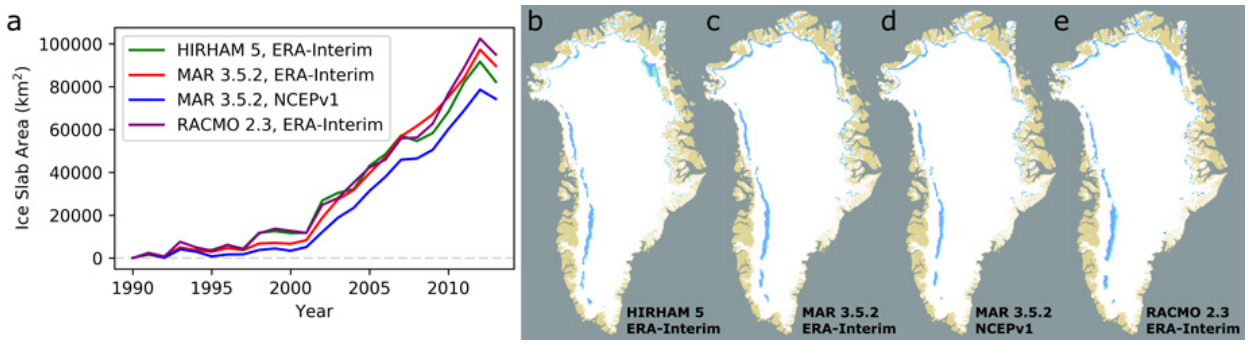

Figure 42 | (a) Modeled LPIS area 1990-2013. Results mapped by (b) HIRHAM 5, (c) MAR 3.5.2 forced by ERA-Interim, (d) MAR 3.5.2 forced by NCEPv1, (e) RACMO 2.3 forced by ERA-Interim.

The steady increase in ice slab formation after the 2002 melt season is clear in the trend lines of LPIS growth (Figure 42-a), with steady growth after that. The slight decrease in LPIS area in 2013 corresponds with the year immediately after the 2012 melt season, when relatively cooler temperatures and high accumulation rates partially offset the rapid growth and slightly re-buffered the highest extent of LPISs in Greenland.

The spatial domains of these simulated LPISs are remarkably consistent with each other (Figure 42, b-e) and with present-day LPISs extent mapped from IceBridge AR data (Figure 38). The consistency between RCM models and against current IceBridge observations provides high confidence for using excess melt as an effective metric when simulating the growth of LPISs across Greenland in a warming climate.

4.3.3 Modeling Future Ice Slab Extent

To simulate the growth of Greenland's LPISs into the future, RCMs are forced by Global Circulation Models (GCMs) on their boundaries. LPISs grow in all RCMs through the 21st Century (Table 5), but RCM 4.5 and 8.5 trends diverge from each other after approximately 2050 (Figure 43).

Table 5 | LPIS Model results, forced by GCMs. † Due to non-continuous data availability, HIRHAM 5 "1990-2050" trends span 2001-2010 and 2031-2050 combined. HIRHAM5 "2051-2100" trends span 2041-2050 and 2081-2100 combined. ‡ The RACMO 2.1 "2051-2100" trend spans 2051-2098, includes only RCP4.5 and is not displayed in Figure 43 due to a lack of RCP 4.5 & 8.5 comparison.

RCM	GCM Forcing	RCP	LPIS trend ($km^2\ a^{-1}$)	p-value	R-value	LPIS area ($10^3\ km^2$)	LPIS trend ($km^2\ a^{-1}$)	p-value	R-value	LPIS area ($10^3\ km^2$)
			1990 - 2050			2050	2051 - 2100			2100
HIRHAM 5†	ECEarth	4.5	1060	5.73e-18	0.989	56.4	772	1.07e-12	0.967	89.2
		8.5	1410	3.14e-22	0.996	72.2	2670	5.70e-21	0.996	205
MAR 3.5.2	CanESM2	4.5	3510	9.83e-44	0.981	227	694	2.70e-05	0.557	243
		8.5	4340	1.58e-53	0.991	256	6810	2.07e-39	0.987	606
MAR 3.5.2	MIROC5	4.5	1950	2.34e-30	0.945	110	1500	1.71e-16	0.872	142
		8.5	1650	2.34e-34	0.960	112	6290	1.21e-38	0.986	420
MAR 3.5.2	NorESM1	4.5	1270	8.93e-23	0.899	103	470	1.69e-04	0.508	104
		8.5	1650	6.06e-30	0.943	63.5	3940	1.45e-36	0.982	255
RACMO 2.1‡	HadGEM2	4.5	3800	1.88e-38	0.971	184	3360	1.39e-30	0.972	345

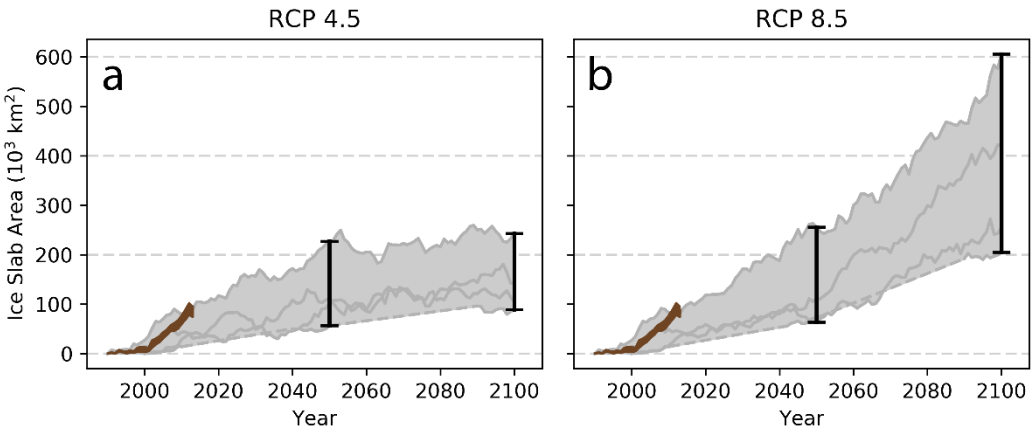

Figure 43 | Modeled LPIS areas through 2100 from GCM-forced RCMs under (a) RCP 4.5 and (b) RCP 8.5. The brown trend line from 1990-2013 shows the spread of "current observations" Reanalysis-forced results displayed in Figure 42. Vertical black bars show the spread of RCM results at 2050 and 2100.

RCM models forced on their boundaries by GCMs all indicate that the area of LPISs across Greenland is likely to expand moderately through 2050, approximately doubling or more in compared to LPIS extent in 2013. Most GCM-forced models under-estimate current ice slab extent through 2013 when compared with reanalysis-forced RCM results (Figure 42). It is unclear whether this low bias of LPIS extent is systemic throughout the entire model run through 2100 or only indicative of inter-annual variability present in reanalysis-forced RCMs that isn't replicated in GCM-forced RCMs. Models forced by RCP 4.5 "moderate emissions" scenarios consistently show a leveling-off of ice slab extent after 2050, growing 1060 – 3510 km^2 a^{-1} in the first half of the century and slowing to 470 – 1500 km^2 a^{-1} from 2051–2100 (Table 5). Under RCP 8.5 "high emissions" scenarios, all models indicate the formation of new ice slabs will accelerate from their 1990-2050 growth (1410-4340 km^2 a^{-1}) to approximately double that rate of growth (2670-6810 km^2 a^{-1}) in the latter half of the century. The cumulative area of ice slabs, relative to pre-1990 steady-state extent, grows by 1-58% under RCP 4.5 from 2050-2100, but by

237-402% in 2100 from their 2050 extent under RCP 8.5 (Table 5). In all cases the pre-2050 and post-2050 trends are statistically significant ($p < 0.0002$).

Figure 43 shows the general trend of LPIS areas through 2100, focusing on the behavior of the entire model ensemble rather than comparing individual RCMs against each other. Figure 44 below identifies the models for comparison with each other, including the RACMO 2.1 result which only contains results for RCP 4.5.

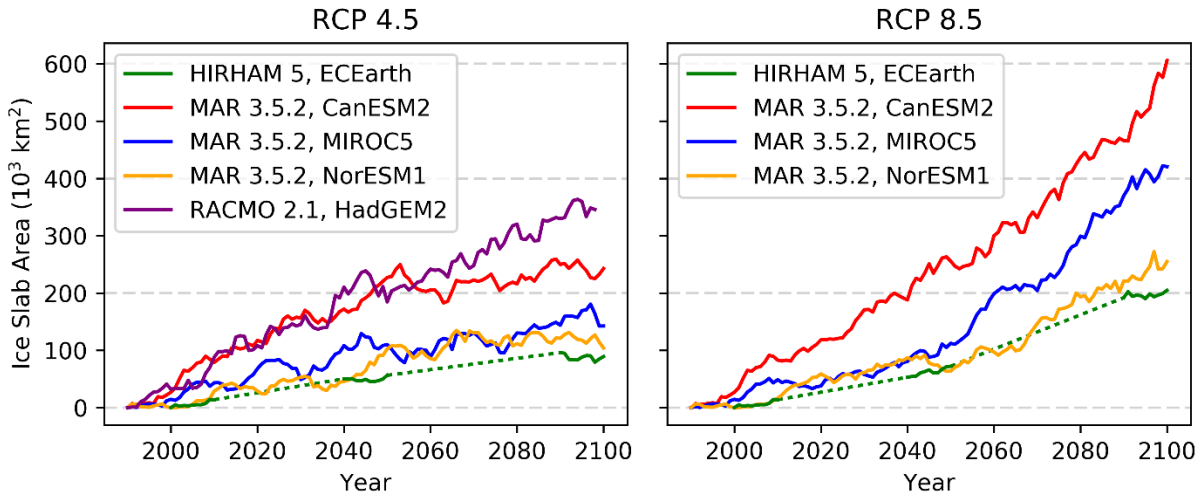

Figure 44 | Modeled LPIS areas through 2100 from five GCM-forced RCMs under RCP 4.5 and 8.5, with all models included and individual models identified. Dotted lines are present in the HIRHAM5 results (green) to fill gaps between incomplete time-series data during 21st century model runs (Table 3).

4.4 Discussion

The upper value of excess melt in that range (573 mm w.e. a^{-1}) would fill a typical porous firn layer (density ~500 kg m^{-3}) into bubbly ice (density 873 kg m^{-3} [(Machguth et al., 2016)]) to a thickness of 15.4 meters, in close agreement with a maximum cutoff thickness of 16 meters used

when detecting LPISs with IceBridge AR data. This first-order calculation compares well to observed ice slab thicknesses (Figure 38) and provides confidence for using excess melt as a metric for the growth of low-permeability ice slabs in Greenland.

The geographical spread of LPISs from RCMs forced by reanalysis data (Figure 42) agrees strongly both between the respective models and against observations (Figure 38), indicating that the RCMs accurately simulate this process when using reanalysis datasets on their boundaries. Minor geographic discrepancies exist between the extent of ice slabs seen in radar data (Figure 38) and simulated by RCMs (Figure 42, b-e), which include ice slabs simulated by the RCMs in far southwest Greenland and along the entire extent of the far north coast that aren't seen in radar observations. These discrepancies are primarily attributable to coverage gaps in the IceBridge data. The extent of LPISs seen by drawing simple polygons around the IceBridge observations from 2010-2014 (69,400 km^2) are likely to slightly underestimate the full extent of LPISs. The slightly-larger values modeled by reanalysis-forced RCMs over the same time period (74,300 - 95,000 km^2) are likely a better estimate for the full extent of ice slabs across Greenland during the span of IceBridge observations. Further work using firn cores and/or more airborne radar may be able to create a better map based on direct observations alone.

When forced on their boundaries by global climate models (GCMs), the RCMs show a much wider range of results. Unlike reanalysis datasets, GCMs are not regularly updated and constrained by weather-station observations and can diverge widely due to internal variability. Although they can simulate the mean state of global climate well against present-day observations, they cannot reliably simulate the timing or magnitude of regional climate cycles

that can affect short-term melt trends in Greenland, such as the North Atlantic Oscillation (Fettweis et al., 2013). GCMs also cannot simulate the precise timing of short-term weather events such as the blocking high-pressure pattern that exacerbated extensive melt across Greenland in the summer 2012 (Hanna et al., 2014). Most RCMs forced by GCMs in this work under-estimate the growth of LPISs in Greenland during the period 1990-2013, with the current observations trending toward the upper end of the envelope of RCM results through 2013 (Figure 43). The least-sensitive of the GCM-forced models show an ice slab extent in 2100 that is no bigger than the extent already observed by the end of 2013, indicating that a low-melt bias exists in at least some of the GCM-forced model results. The same RCMs forced by reanalysis data simulate LPIS extent very closely; the wide range of LPIS extents in Table 5 and Figure 43 are likely the results of GCM forcing at the RCM grid boundaries. Accurate boundary forcing on RCM model domains remains a first-order uncertainty in projecting the future extent of low-permeability ice slabs across Greenland.

Regional patterns of future LPIS extent (Figure 45) show geographic variations between emissions scenarios and RCM runs. Under RCP 4.5, the overall spatial pattern of LPISs mirror those seen presently with reanalysis-forced data (Figure 42). The upper extent of LPISs simply extend further uphill in a warming climate. However, as changes grow larger under RCP 8.5, differences emerge based primarily upon changing snow accumulation rates. Snowfall in the polar regions can increase in a warming climate (Frieler et al., 2015), leading some areas of moderate-accumulation (such as far southwest Greenland) to transition to high-accumulation regimes in the future, favoring the formation of perennial firn aquifers (Forster et al., 2014; Koenig et al., 2013; Miège et al., 2016) rather than ice slabs. Such a transition from one

hydrologic regime to another has not been studied in Greenland, and it is uncertain how such a transition from ice slabs to aquifer might occur, or what its effects might be on local water storage and runoff. For this work, it is assumed that when local snowfall for a decade or more has exceeded the threshold by which aquifers are expected to form, that ice slabs no longer play the major role in runoff and are omitted from the ice slab extents in Figure 45. Further work is needed to more accurately define the nature by which such hydrologic transitions occur within Greenland's firn layer and their effects on runoff.

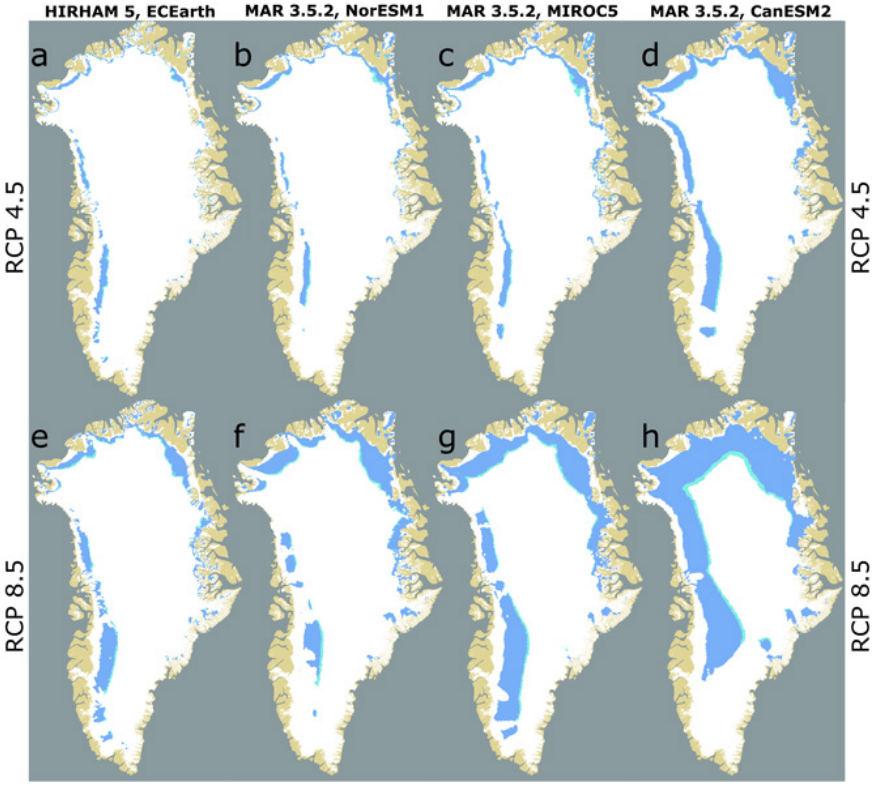

Figure 45 | Geographic extent of LPISs in the year 2100 using four GCM-forced RCM models under RCP 4.5 (a-d) and RCP 8.5 (e-h) emissions scenarios.

Despite uncertainty in the total and regional extent of ice slabs through 2100, the overall behavior of LPISs through the 21st century remains consistent between RCM model runs. All

RCMs show a consistent growth of ice slabs through the first half of the 21st century, approximately doubling the size of Greenland's potential runoff zone by 2050. Under RCP 4.5, the growth of LPISs steadily slows after 2050 through 2100, indicating a possible "leveling off" of Greenland's runoff extent by 2100. This is consistent with the RCP4.5 emissions pathway which has greenhouse-gas concentrations stabilizing by 2050, which in turn appears to stabilize the runoff zone in Greenland. Under RCP 8.5, the growth of LPISs increase similarly to RCP 4.5 through mid-century, but diverge significantly after that, doubling their speed of growth through 2100. This rapid acceleration of the area of Greenland's runoff zone in the latter half of the century is forced by increased surface melt at higher elevations. The parabolic hypsometry of the ice sheet plays a role, which favors a more rapid expansion of LPISs as local surface slopes flatten the further inland they go (Mikkelsen et al., 2016; van As et al., 2017). If melt continues to increase further uphill, the area of the ice sheet affected gets progressively larger as slopes decrease in Greenland's interior.

Low-permeability ice slabs represent a rapid feedback by which melt can cause runoff to occur from high-elevation regions of Greenland where it had previously been assumed to refreeze. The current extent and future vulnerability to this feedback in Greenland has never before been quantified. Greenland's runoff zone is likely to expand by 40-66% by mid-century regardless of likely emissions scenarios, and by up to 177% at the end of the century if emissions are not reduced. Regardless of future forcing, the warming Arctic climate is set to produce a wetter, more runoff-prone Greenland by the year 2100. However, the ~250% difference between moderate- and high-emissions scenarios in 2100 suggests that anthropogenic emissions will

continue to play a decisive role in determining the future extent of Greenland's runoff zone and its contribution to sea-level rise during this century.

5 CONCLUSIONS AND FUTURE WORK

5.1 Summary and Future Implications

I have examined three fundamental aspects about the formation of near-surface low-permeability ice slabs in the accumulation zone of the Greenland ice sheet.

First, I have shown ice slabs greater than a meter thick can form when melt increases enough in wet snow zones to regularly saturate the near-surface firn. Low-permeability ice slabs (LPISs) can be continuous for kilometers, causing runoff in warm melt seasons. LPISs take up to a decade to form, but once formed, continue to grow thicker in subsequent melt years. Meltwater lakes form on top of ice slabs, and surface channels form efficient drainage systems for water to reach lower elevations and eventually run off. I have demonstrated this process occurred in southwest Greenland during the 2012 melt summer, when we observed LPISs in cores under the surface at the KAN-U site, with lakes, slush fields and water channels flowing over them in satellite imagery later that summer. I developed a water table model which simulates the rate at which the available near-surface firn would have saturated at KAN-U in mid-July 2012, which is consistent with satellite observations and peak runoff volumes in the Watson River downstream from the KAN-U site. We have shown that these ice-slabbed regions of saturation contributed 14 ± 3 % to the runoff in that area of southwest Greenland in summer 2012 (Machguth et al., 2016). In summer 2016 the KAN-U site again saturated, contributing further runoff to the Watson River that summer. I have used firn core measurements from 2012 to 2017 to show the ice slabs have grown thicker during that time span. If summer warming continues in Greenland, KAN-U is likely to run off again in the future, perhaps more frequently.

Second, I have mapped the extent of low-permeability ice slabs across the Greenland ice sheet using airborne radar measurements to create the first-ever observations of LPIS formation over wide areas. I have developed an algorithm for identifying ice slabs with high-resolution *in situ* radar, tuning that radar using adjacent firn cores in order to map an ice slab across a radar transect. I linked *in situ* radar with airborne radar from NASA's Operation IceBridge in order to identify LPISs with airborne radar data sets and enable their mapping across wide areas. I developed a new workflow for correcting and normalizing multiple years of IceBridge data flown on different aircraft with different antenna configurations, creating a single, usable dataset for mapping LPISs across the Greenland ice sheet. The automated algorithm minimizes the subjectivity and excessive manual labor of selecting and outlining LPISs by hand in radar data. The map created by this algorithm in Greenland is the first wide-area map of LPISs ever made on any glaciated region on Earth. I have identified the geographic areas where LPISs have formed on the Greenland ice sheet, which now cover a minimum of 69,400 km^2, or ≥4.4% of the ice sheet. LPISs have already increased Greenland's runoff in warm melt seasons.

Third, I have identified the concept of "excess melt" as the amount of meltwater that exceeds the ability for annual accumulation to absorb and refreeze it. I have created a formulation for excess melt that is easily quantifiable from the outputs of regional climate models and effective at predicting where LPISs will form in Greenland. Using thresholds for excess melt constrained by airborne radar observations of LPISs, I have empirically identified the amount of excess melt needed to form ice slabs that are capable of causing runoff. From these modeling results, I have

shown that ice slabs began forming in Greenland slowly after 1990 until the early 2000s. After 2002, ice slabs grew relatively rapidly within the firn to their current observed extent.

Using multiple regional climate model (RCM) historical datasets, I have used excess melt to simulate the current extent of LPISs in Greenland, which show a strong spatial agreement with IceBridge observations and with each other, strengthening the confidence for using excess melt as a metric for LPIS formation. The maps produced by these RCMs help "fill the gaps" if IceBridge data coverage, showing a complete LPIS extent of 75-95,000 km^2, or ~5 % of the ice sheet.

I have used RCMs forced on their grid boundaries by global-scale general climate models (GCMs) to predict the growth of LPISs through the 21st century. I have shown that RCMs consistently predict LPISs to approximately double in size from their current extent by the year 2050. In the second half of the century (2050-2100) the growth of LPISs depends largely upon our global emissions pathways. Under RCP4.5, the extent of LPISs primarily levels off after 2050, while under RCP8.5 emissions the rate of LPIS growth doubles through 2100, representing an accelerated feedback that could have enormous implications for ice sheet runoff. I have shown that the GCM-forced RCM datasets show a much wider range of outcomes than those forced by Reanalysis data. The MAR 3.5.2 RCM dataset, when forced by different GCM boundary conditions, shows a wide range of possible outcomes for present and future LPIS extent. This result demonstrates the importance of determining accurate boundary forcings when predicting the future surface-mass balance conditions of the Greenland ice sheet. Among the GCM-forced RCM datasets used, most of them underestimated the extent of LPISs currently

seen across Greenland when compared to their reanalysis-forced counterparts. This bias indicates that future LPIS extent may be at the upper end of the GCM-forced model range through 2100. The most extreme RCM model (MAR 3.5.2, boundary-forced by CanESM1, RCP 8.5), which fits closest to current observations, shows an LPIS extent of 606,000 km^2 by 2100, 35 % of the Greenland ice sheet. When combined with 20 % of the ice sheet currently in the long-term ablation zone, this would represent an ice sheet with ~55 % of its area in the runoff zone in a warm melt summer. This has enormous effects on future hydrology of the ice sheet and has dangerous implications for residents of coastal communities who live close to rivers fed by the ice sheet, such as Kangerlussuaq.

5.2 Future Work

This work demonstrates a rapid feedback occurring in Greenland's firn that is already affecting runoff in Greenland and is expected to continue in the future. I have provided evidence to help answer several primary questions about ice slabs in Greenland's firn. However, multiple questions remain that could be addressed. This section will briefly discuss potential avenues for future research.

5.2.1 Forming Ice Slabs at High Resolutions

Firn cores, airborne radar and modeling suggests that LPISs form in Greenland when enough melt enters the firn column to overwhelm the ability to maintain open pathways for percolation and refreezing. I have demonstrated empirically that thresholds exist which have formed ice slabs in Greenland's current accumulation zone.

No extensive field, lab, or modeling studies yet exist which show the physical formation of thick, continuous slabs in a firn column. I have identified ice slabs after they have formed and observed their effects on runoff. But we have not yet recorded any data that shows or simulates the transformation of heterogeneous ice layers which do not affect runoff into homogeneous ice slabs that cause runoff.

With Professor Hari Rajaram in the University of Colorado's Civil Engineering Department, we have acquired a small seed grant ($50K) to perform a high-resolution modeling experiment (<1 m) at the KAN-U site to see if we can model the formation of ice slabs at that site and reproduce observations. A goal of the seed study is to help define and illuminate the limitations of coarse-resolution RCMs in simulating the transition of ice lenses into ice slabs. Focused field studies at select sites (such as Dye-2) may also help illustrate exactly how ice slabs form.

5.2.2 The Future Evolution of Ice Existing Slabs

At KAN-U, ice slabs have continued to grow thicker since we first observed them in 2012. If melt continues to increase at KAN-U, it is unclear whether ice slabs will continue to grow thicker or not. If melt increases to make KAN-U routinely below the equilibrium line (i.e. where melt regularly exceeds accumulation), existing ice slabs may progressively melt away, presumably getting thinner over time. KAN-U still has significant pore space at depth, with pore close-off depth about 50 meters under the surface. If slabs are stripped away, it is unclear whether it would expose underlying firn to fill again and buffer against runoff, or whether ice slabs would simply continue to grow thicker without interruption. More work is needed to elucidate these processes as Greenland continues to warm.

5.2.3 The Binary Nature of Ice Slabs and Firn Aquifers

I have shown that ice slabs only grow in regions where excess melt has increased in recent years, and where annual accumulation rates are low enough (≤~570 mm w.e. a^{-1}) to allow winter cold to refreeze water into ice lenses and slabs. Other work has demonstrated that in regions of high accumulation, snow insulates meltwater and inhibits refreezing. In these regions, perennial firn aquifers (PFAs) form which store liquid water through the winter (Forster et al., 2014; Koenig et al., 2013; Miège et al., 2016). Water flows through these porous aquifers, typically draining into crevasses (Poinar et al., 2017).

IceBridge accumulation radar has been used to map the extent of PFAs in high-accumulation areas across Greenland (Miège et al., 2016) (Figure 4). When the map of PFAs is overlaid on the map of LPISs (Figure 46), a "binary" relationship is immediately suggested. Increases in liquid water across Greenland's lower accumulation zone seem to take one of two pathways, either refreezing into LPISs in low-accumulation areas, or remaining liquid as PFAs in high-accumulation areas. This forms a dichotomy of two hydrologic "regimes" in Greenland's lower accumulation zone, driven almost entirely by differences in accumulation rates.

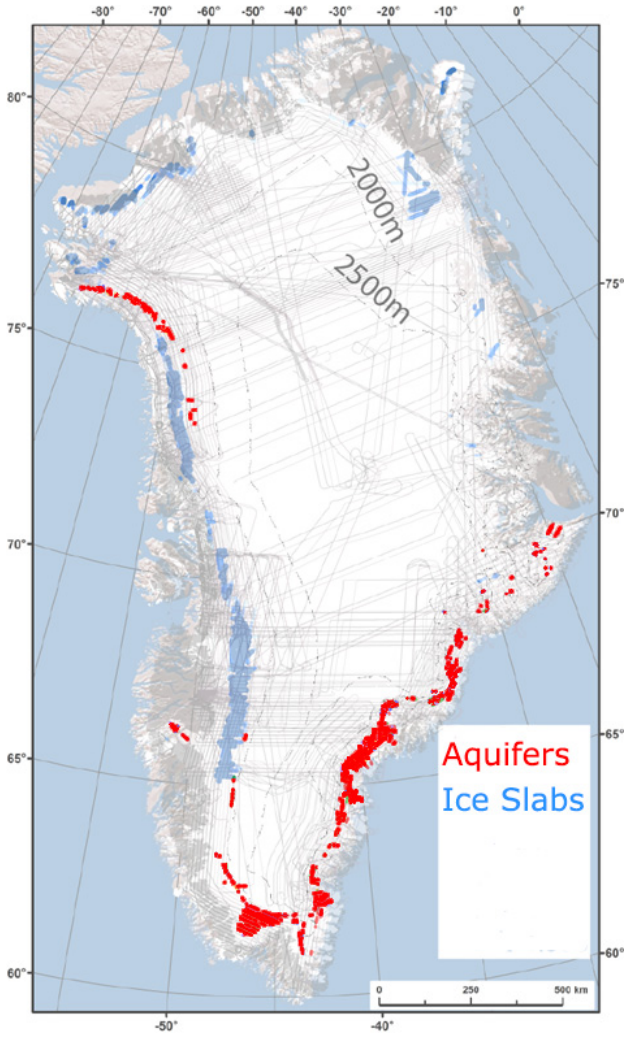

Figure 46 | Map of Greenland ice slabs (Figure 38) overlaid atop a map of firn aquifers (Figure 4).

What happens when accumulation rates change, causing a shift from one hydrologic regime to the other? This question is more than purely hypothetical. In Chapter 4, using RCM models to predict LPIS extent into the future, there were some regions where models showed accumulation rates increased with rising temperatures. During the modeling work, I assumed that if a map pixel containing LPISs accumulated enough snow for ten years or more to form PFAs, any existing LPIS would be buried enough to become irrelevant to near-surface hydrology, and would be rendered irrelevant to LPIS runoff. The ice slab would effectively “disappear” and the

area would transition to an aquifer regime. It is unclear whether a perennial firn aquifer will be able to form at all if an ice slab is already present to prevent deep percolation. The possibility of changing firn hydrology from one regime to another is currently unexplored. Future modeling may help illuminate such a process. A directed field campaign, especially in a boundary area where PFAs and LPISs exist in close proximity to each other, may also elucidate what happens in cold polar firn during such a transition. Future runoff from significant portions of the ice sheet may depend upon how hydrologic regime changes happen.

5.2.4 Interpretations of Altimetry

The initial motivation for this work was the interpretation of airborne and satellite altimetry. To convert volume change into mass change, all altimetry missions must account for density changes in Greenland's firn. The injection of increasing meltwater in to the firn directly affects altimetry-based interpretations in two ways. First, as meltwater leaves the surface and refreezes at depth it immediately makes the underlying firn more dense, becoming a rapid form of compaction. Second, water releases 334 kJ kg^{-1} of latent heat into the firn column when it refreezes, warming the firn around it and increasing compaction rates for months afterward. Such refreezing events is clearly seen from thermistor string measurements buried vertically in the firn column (Humphrey et al., 2012; Charalampidis et al., 2016, e.g.).

In standard altimetry interpretations (Zwally et al., 2011, e.g.), Greenland is divided into two zones. In the ablation zone, no firn exists, all meltwater is assumed to run off the ice sheet, and no density changes are assumed to happen. In the accumulation zone, all meltwater is assumed to refreeze in the firn column, increasing compaction rates but not changing mass. This dividing

line is based upon steady-state assumptions that are no longer true in Greenland's changing climate.

Low-permeability ice slabs create a new hydrologic regime not previously considered in altimetry studies. In an LPIS regime, meltwater can be retained and refreeze atop ice slabs with no local mass loss. Such was the case in 2013 and 2014 at KAN-U, when melt water relatively low and the LPISs grew thicker. In high melt years, water can run off and be lost, directly contributing to sea level rise, as seen in 2012 at KAN-U. Underlying firn, which is now hydrologically isolated from the surface melt, continues to slowly compact, and must be accounted for to correctly interpret elevation change at that location. Meltwater no longer refreezes as deeply as it would in a deep percolation regime (Humphrey et al., 2012; Machguth et al., 2016). Because of their ability to isolate deep firn from additional meltwater, LPISs are assumed to have a cooling effect on underlying firn, slowing firn compaction rates. The precise nature and magnitude of this feedback is still poorly understood, but must be accounted for in order to correctly interpret altitude changes from airborne or satellite altimetry products.

5.2.5 Possible Ice Slabs in Antarctica

All the work presented thus far has concentrated on the Greenland ice sheet. Increases in meltwater have occurred in parts of coastal Antarctica as well, sometimes at greater rates than is seen in Greenland (Domack et al., 2013). The formation and subsequent rapid drainage of surface ponds is known to be a key factor in the sudden disintegration of the Larsen B ice shelf (Scambos et al., 2003; Banwell et al., 2013). No subsurface observations were available at the time to know whether ice slabs played a role in Larsen B's 2002 disintegration event. Ice slabs

forming on the nearby Larsen C ice shelf could have direct implications on the ice shelf's future stability. Although Larsen C has not yet witnessed the extensive surface ponding that was seen on Larsen B prior to its breakup, some ponds have been seen there, which have formed near the interior margins of the ice shelf in response to warm föhn winds (Hubbard et al., 2016).

A series of 2006 photos by Ted Scambos on an Antarctic Peninsula field campaign show the edges of a tabular iceberg recently calved from Larsen C at the time (Figure 47).

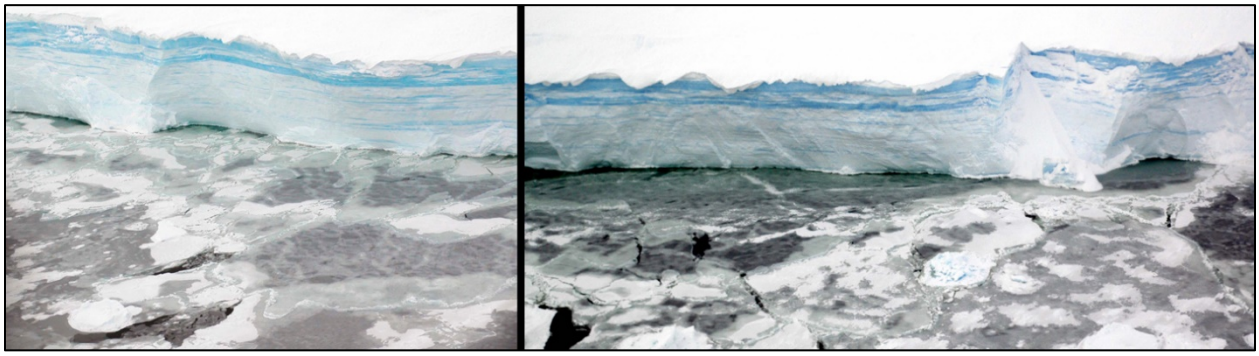

Figure 47 | Photos from the margin of an iceberg calved from the Larsen C ice shelf, Antarctica, 2006. Iceberg freeboard is approximately ~20 m here, with ice slabs seen in the top ~5 meters of firn. (Image courtesy of Ted Scambos, personal correspondence)

These images strongly suggest that ice slabs were forming on Larsen C in 2006. It is unclear how extensive the ice slabs were, what area of Larsen C was covered by them, or whether they were thick enough to cause ponding on the ice shelf's surface. The iceberg had approximately a ~20 m freeboard height, suggesting the ice slabs are 2-4 m thick (Ted Scambos, personal correspondence). It is also unclear how or whether the ice slabs have evolved since 2006. A contemporary airborne radar mapping of LPISs on the Larsen C and other nearby ice shelves might help illuminate these questions. Requests have been put out to teams visiting Larsen C

during the upcoming 2017-18 field season, to see whether similar photos can be acquired which might help provide qualitative answers to these questions.

5.3 Perspective

The 2012 discovery of low-permeability ice slabs in southwest Greenland was an accident. I joined a field team with colleagues at the KAN-U field site, where I installed prototype firn compaction instruments. We drilled boreholes and discovered massive ice slabs hidden just beneath the surface at KAN-U. The subsequent 2012 melt season occurred in mid-July, flooding the Watson River and washing a Caterpillar tractor off a bridge in Kangerlussuaq. I found a LandSat-7 image which clearly showed meltwater pooling at KAN-U and running into drainage channels off the ice. My firn compaction instruments melted out completely in 2012 and proved useless that summer, but that extraordinary melt formed the basis for the entire dissertation presented here. The conditions under which my first instruments failed were key to the success of this present study.

It is both exciting and terrifying to make such a discovery. The implications are important, but have grave potential consequences for the future of the Greenland ice sheet. The work is necessary for understanding the current changing hydrology of the Greenland ice sheet, and more work will be needed to understand how that hydrology will change in the future. The melt will get worse, the flooding more intense. Seas will rise faster. This work is our best efforts so far to answer how extreme future conditions in Greenland may get.

My children are school-aged now. The Greenland they will know in their adulthood will be a fundamentally different place than it was in my own childhood. We do not yet know what secrets the sleeping giant of Greenland still has hidden. I am certain we have not seen the last rapid feedback of the Greenland ice sheet. I hope that we will be able to discover them in time to make a difference, to possibly mitigate the changes, or at least to prepare for them.

In the meantime, we keep working.

REFERENCES

Abdalati, W., Zwally, H. J., Bindschadler, R., Csatho, B., Farrell, S. L., Fricker, H. A., … Webb, C. (2010). The ICESat-2 Laser Altimetry Mission. *Proceedings of the IEEE*, *98*(5), 735–751. https://doi.org/10.1109/JPROC.2009.2034765

Arthern, R. J., Vaughan, D. G., Rankin, A. M., Mulvaney, R., & Thomas, E. R. (2010). *In situ* measurements of Antarctic snow compaction compared with predictions of models. *Journal of Geophysical Research*, *115*, 12 PP. https://doi.org/201010.1029/2009JF001306

Bader, H. (1954). Sorge's law of densification of snow on high polar glaciers. *Journal of Glaciology*, *2*(15), 319–323.

Baldridge, A. M., Hook, S. J., Grove, C. I., & Rivera, G. (2009). The ASTER spectral library version 2.0. *Remote Sensing of Environment*, *113*(4), 711–715. https://doi.org/10.1016/j.rse.2008.11.007

Banwell, A. F., MacAyeal, D. R., & Sergienko, O. V. (2013). Breakup of the Larsen B Ice Shelf triggered by chain reaction drainage of supraglacial lakes. *Geophysical Research Letters*, *40*(22), 2013GL057694. https://doi.org/10.1002/2013GL057694

Benson, C. S. (1962). *Stratigraphic Studies in the Snow and Firn of the Greenland Ice Sheet* (Research Report No. 10). U.S. Army Snow, Ice and Permafrost Research Establishment, Corps of Engineers. Retrieved from http://oai.dtic.mil/oai/oai?verb=getRecord&metadataPrefix=html&identifier=ADA337542

Bentsen, M., Bethke, I., Debernard, J. B., Iversen, T., Kirkevåg, A., Seland, Ø., … Kristjánsson, J. E. (2013). The Norwegian Earth System Model, NorESM1-M – Part 1: Description and basic evaluation of the physical climate. *Geosci. Model Dev.*, *6*(3), 687–720. https://doi.org/10.5194/gmd-6-687-2013

Bezeau, P., Sharp, M., Burgess, D., & Gascon, G. (2013). Firn profile changes in response to extreme 21st-century melting at Devon Ice Cap, Nunavut, Canada. *Journal of Glaciology*, *59*(217), 981–991. https://doi.org/10.3189/2013JoG12J208

Box, J. E., Cappelen, J., Chen, C., Decker, D., Fettweis, X., Hall, D., … Wahr, J. (2011). *Greenland Ice Sheet (in Arctic Report Card 2011)*. Retrieved from http://www.arctic.noaa.gov/report11/

Box, Jason E., Bromwich, D. H., Veenhuis, B. A., Bai, L.-S., Stroeve, J. C., Rogers, J. C., … Wang, S.-H. (2006). Greenland Ice Sheet Surface Mass Balance Variability (1988–2004) from Calibrated Polar MM5 Output. *Journal of Climate*, *19*(12), 2783–2800. https://doi.org/10.1175/JCLI3738.1

Braithwaite, R. J., Laternser, M., & Pfeffer, W. T. (1994). Variations of near-surface firn density in the lower accumulation area of the Greenland ice sheet, Pâkitsoq, West Greenland. *Journal of Glaciology*, *40*(136), 477–485.

Brown, J., Harper, J., Pfeffer, W. T., Humphrey, N., & Bradford, J. (2011). High-resolution study of layering within the percolation and soaked facies of the Greenland ice sheet. *Annals of Glaciology*, *52*(59), 35–42. https://doi.org/10.3189/172756411799096286

Charalampidis, C., van As, D., Box, J. E., van den Broeke, M. R., Colgan, W. T., Doyle, S. H., … Smeets, C. J. P. P. (2015). Changing surface–atmosphere energy exchange and refreezing capacity of the lower accumulation area, West Greenland. *The Cryosphere*, *9*(6), 2163–2181. https://doi.org/10.5194/tc-9-2163-2015

Charalampidis, Charalampos, Van As, D., Colgan, W. T., Fausto, R. S., Macferrin, M., & Machguth, H. (2016). Thermal tracing of retained meltwater in the lower accumulation area of the Southwestern Greenland ice sheet. *Annals of Glaciology*, 1–10. https://doi.org/10.1017/aog.2016.2

Christensen, O., Drews, M., Christensen, J., Dethloff, K., Ketelsen, K., Hebestadt, I., & Rinke, A. (2007). *The HIRHAM regional climate model version 5 (β). Danish Meteorological Institute Technical Report 06-17*.

Chylek, P., Li, J., Dubey, M. K., Wang, M., & Lesins, G. (2011). Observed and model simulated 20th century Arctic temperature variability: Canadian Earth System Model CanESM2. *Atmos. Chem. Phys. Discuss.*, *2011*, 22893–22907. https://doi.org/10.5194/acpd-11-22893-2011

Collins, W. J., Bellouin, N., Doutriaux-Boucher, M., Gedney, N., Hinton, T., Jones, C. D., … Kim, J. (2008). Evaluation of the HadGEM2 model. *Met Office Hadley Centre Technical Note*. Retrieved from http://www.metoffice.gov.uk/publications/HCTN/index.html

Cuffey, K. M., & Paterson, W. S. B. (2010). *The Physics of Glaciers*. Academic Press.

de la Peña, S., Howat, I. M., Nienow, P. W., van den Broeke, M. R., Mosley-Thompson, E., Price, S. F., … Sole, A. J. (2015). Changes in the firn structure of the western Greenland Ice Sheet caused by recent warming. *The Cryosphere*, *9*(3), 1203–1211. https://doi.org/10.5194/tc-9-1203-2015

Dee, D. P., Uppala, S. M., Simmons, A. J., Berrisford, P., Poli, P., Kobayashi, S., … Vitart, F. (2011). The ERA-Interim reanalysis: configuration and performance of the data assimilation system. *Quarterly Journal of the Royal Meteorological Society*, *137*(656), 553–597. https://doi.org/10.1002/qj.828

Domack, E., Leventer, A., Burnett, A., Bindschadler, R., Convey, P., & Kirby, M. (2013). *Antarctic Peninsula Climate Variability: Historical and Paleoenvironmental*

Perspectives. Wiley. Retrieved from http://www.wiley.com/WileyCDA/WileyTitle/productCd-0875909736.html

Doyle, S. H., Hubbard, A., van de Wal, R. S. W., Box, J. E., van As, D., Scharrer, K., … Hubbard, B. (2015). Amplified melt and flow of the Greenland ice sheet driven by late-summer cyclonic rainfall. *Nature Geoscience*, *8*(8), 647–653. https://doi.org/10.1038/ngeo2482

Fettweis, X., Franco, B., Tedesco, M., van Angelen, J. H., Lenaerts, J. T. M., van den Broeke, M. R., & Gallée, H. (2013). Estimating the Greenland ice sheet surface mass balance contribution to future sea level rise using the regional atmospheric climate model MAR. *The Cryosphere*, *7*(2), 469–489. https://doi.org/10.5194/tc-7-469-2013

Fitzpatrick, A. A. W., Hubbard, A. L., Box, J. E., Quincey, D. J., van As, D., Mikkelsen, A. P. B., … Jones, G. A. (2014). A decade (2002–2012) of supraglacial lake volume estimates across Russell Glacier, West Greenland. *The Cryosphere*, *8*(1), 107–121. https://doi.org/10.5194/tc-8-107-2014

Forster, R. R., Box, J. E., van den Broeke, M. R., Miège, C., Burgess, E. W., van Angelen, J. H., … McConnell, J. R. (2014). Extensive liquid meltwater storage in firn within the Greenland ice sheet. *Nature Geoscience*, *7*(2), 95–98. https://doi.org/10.1038/ngeo2043

Frieler, K., Clark, P. U., He, F., Buizert, C., Reese, R., Ligtenberg, S. R. M., … Levermann, A. (2015). Consistent evidence of increasing Antarctic accumulation with warming. *Nature Climate Change*, *5*(4), 348–352. https://doi.org/10.1038/nclimate2574

Gascon, G., Sharp, M., Burgess, D., Bezeau, P., & Bush, A. B. G. (2013). Changes in accumulation-area firn stratigraphy and meltwater flow during a period of climate warming: Devon Ice Cap, Nunavut, Canada. *Journal of Geophysical Research: Earth Surface*, *118*(4), 2380–2391. https://doi.org/10.1002/2013JF002838

Grenander, U. (1959). *Probability and Statistics: The Harald Cram鈔r Volume*. Alqvist & Wiksell.

Hamilton, G. S., & Whillans, I. M. (2000). Point measurements of mass balance of the Greenland Ice Sheet using precision vertical Global Positioning System (GPS) surveys. *Journal of Geophysical Research*, *105*(B7), PP. 16,295-16,301. https://doi.org/200010.1029/2000JB900102

Hanna, E., Fettweis, X., Mernild, S. H., Cappelen, J., Ribergaard, M. H., Shuman, C. A., … Mote, T. L. (2014). Atmospheric and oceanic climate forcing of the exceptional Greenland ice sheet surface melt in summer 2012. *International Journal of Climatology*, *34*(4), 1022–1037. https://doi.org/10.1002/joc.3743

Harper, J., Humphrey, N., Pfeffer, W. T., Brown, J., & Fettweis, X. (2012). Greenland ice-sheet contribution to sea-level rise buffered by meltwater storage in firn. *Nature*, *491*(7423), 240–243. https://doi.org/10.1038/nature11566

Hazeleger, W., Severijns, C., Semmler, T., Ştefănescu, S., Yang, S., Wang, X., … Willén, U. (2010). EC-Earth: A Seamless Earth-System Prediction Approach in Action. *Bulletin of the American Meteorological Society*, *91*(10), 1357–1363. https://doi.org/10.1175/2010BAMS2877.1

Herron, M., & Langway, C. (1980). Firn Densification - An Empirical Model. *Journal of Glaciology*, *25*(93), 373–385.

Holland, D. M., Thomas, R. H., de Young, B., Ribergaard, M. H., & Lyberth, B. (2008). Acceleration of Jakobshavn Isbræ triggered by warm subsurface ocean waters. *Nature Geoscience*, *1*(10), 659–664. https://doi.org/10.1038/ngeo316

Howat, I. M., de la Peña, S., van Angelen, J. H., Lenaerts, J. T. M., & van den Broeke, M. R. (2013). Brief Communication “Expansion of meltwater lakes on the Greenland Ice Sheet.” *The Cryosphere*, *7*(1), 201–204. https://doi.org/10.5194/tc-7-201-2013

Howat, I. M., Negrete, A., & Smith, B. E. (2014). The Greenland Ice Mapping Project (GIMP) land classification and surface elevation data sets. *The Cryosphere*, *8*(4), 1509–1518. https://doi.org/10.5194/tc-8-1509-2014

Hubbard, B., Luckman, A., Ashmore, D. W., Bevan, S., Kulessa, B., Kuipers Munneke, P., … Rutt, I. (2016). Massive subsurface ice formed by refreezing of ice-shelf melt ponds. *Nature Communications*, *7*, 11897. https://doi.org/10.1038/ncomms11897

Humphrey, N. F., Harper, J. T., & Pfeffer, W. T. (2012). Thermal tracking of meltwater retention in Greenland’s accumulation area. *Journal of Geophysical Research*, *117*, 11 PP. https://doi.org/201210.1029/2011JF002083

IPCC. (2013). *Climate Change 2013: The Physical Science Basis. Contribution of Working Group 1 to the Fifth Assessment Report of the Intergovernmental Panel on Climate Change [Stocker, T.F., D. Qin, G.-K. Plattner, S.K. Allen, J. Boschung, A. Nauels, Y. Xia, V. Bex and P.M. Midgley (eds.)]*. Cambridge University Press, Cambridge, United Kingdom and New York, NY, USA, 1535 pp.

Jol, H. M. (2008). *Ground Penetrating Radar Theory and Applications*. Elsevier.

Kalnay, E., Kanamitsu, M., Kistler, R., Collins, W., Deaven, D., Gandin, L., … Joseph, D. (1996). The NCEP/NCAR 40-Year Reanalysis Project. *Bulletin of the American Meteorological Society*, *77*(3), 437–471. https://doi.org/10.1175/1520-0477(1996)077<0437:TNYRP>2.0.CO;2

Kjeldsen, K. K., Korsgaard, N. J., Bjørk, A. A., Khan, S. A., Box, J. E., Funder, S., … Kjær, K. H. (2015). Spatial and temporal distribution of mass loss from the Greenland Ice Sheet since AD 1900. *Nature*, *528*(7582), 396–400. https://doi.org/10.1038/nature16183

Koenig, L. S., Lampkin, D. J., Montgomery, L. N., Hamilton, S. L., Turrin, J. B., Joseph, C. A., … Gogineni, P. (2015). Wintertime storage of water in buried supraglacial lakes across the Greenland Ice Sheet. *The Cryosphere*, *9*(4), 1333–1342. https://doi.org/10.5194/tc-9-1333-2015

Koenig, Lora S., Box, J. E., & Kurtz, N. (2013). Improving Surface Mass Balance Over Ice Sheets and Snow Depth on Sea Ice. *EOS Transactions, 94*(10), 100–100. https://doi.org/doi:10.1002/2013EO100006

Koenig, Lora S., Miège, C., Forster, R. R., & Brucker, L. (2013). Initial *in situ* measurements of perennial meltwater storage in the Greenland firn aquifer. *Geophysical Research Letters*, n/a–n/a. https://doi.org/10.1002/2013GL058083

Kou, L., Labrie, D., & Chylek, P. (1993). Refractive indices of water and ice in the 0.65- to 2.5-μm spectral range. *Applied Optics*, *32*(19), 3531. https://doi.org/10.1364/AO.32.003531

Kovacs, A. (1970). *Camp Century Revisited -- A Pictorial View-June 1969* (No. SR 150). Cold Regions Research and Engineering Laboratory.

Kovacs, A., Gow, A. J., & Morey, R. M. (1993). *A Reassessment of the In-Situ Dielectric Constant of Polar Firn*.

Kovacs, A., Gow, A. J., & Morey, R. M. (1995). The in-situ dielectric constant of polar firn revisited. *Cold Regions Science and Technology*, *23*(3), 245–256. https://doi.org/10.1016/0165-232X(94)00016-Q

Langen, P. L., Fausto, R. S., Vandecrux, B., Mottram, R. H., & Box, J. E. (2017). Liquid Water Flow and Retention on the Greenland Ice Sheet in the Regional Climate Model HIRHAM5: Local and Large-Scale Impacts. *Frontiers in Earth Science*, *4*. https://doi.org/10.3389/feart.2016.00110

Leuschen, C. (2014). *IceBridge Accumulation Radar L1B Geolocated Radar Echo Strength Profiles* (No. Version 2). Boulder, Colorado USA: NASA DAAC at the National Snow and Ice Data Center.

Liang, Y.-L., Colgan, W., Lv, Q., Steffen, K., Abdalati, W., Stroeve, J., … Bayou, N. (2012). A decadal investigation of supraglacial lakes in West Greenland using a fully automatic detection and tracking algorithm. *Remote Sensing of Environment*, *123*, 127–138. https://doi.org/10.1016/j.rse.2012.03.020

Ligtenberg, S. R. M., Helsen, M. M., & van den Broeke, M. R. (2011). An improved semi-empirical model for the densification of Antarctic firn. *The Cryosphere*, *5*(4), 809–819. https://doi.org/10.5194/tc-5-809-2011

MacGregor, J. A., Fahnestock, M. A., Catania, G. A., Paden, J. D., Prasad Gogineni, S., Young, S. K., … Morlighem, M. (2015). Radiostratigraphy and age structure of the Greenland Ice Sheet. *Journal of Geophysical Research: Earth Surface*, *120*(2), 2014JF003215. https://doi.org/10.1002/2014JF003215

Machguth, H., MacFerrin, M., van As, D., Box, J. E., Charalampidis, C., Colgan, W., … van de Wal, R. S. W. (2016). Greenland meltwater storage in firn limited by near-surface ice formation. *Nature Climate Change*, *6*(4), 390–393. https://doi.org/10.1038/nclimate2899

McGrath, D., Colgan, W., Bayou, N., Muto, A., & Steffen, K. (2013). Recent warming at Summit, Greenland: Global context and implications. *Geophysical Research Letters*, *40*(10), 2091–2096. https://doi.org/10.1002/grl.50456

McMillan, M., Leeson, A., Shepherd, A., Briggs, K., Armitage, T. W. K., Hogg, A., … Gilbert, L. (2016). A high-resolution record of Greenland mass balance. *Geophysical Research Letters*, 2016GL069666. https://doi.org/10.1002/2016GL069666

Miège, C., Forster, R. R., Brucker, L., Koenig, L. S., Solomon, D. K., Paden, J. D., … Gogineni, S. (2016). Spatial extent and temporal variability of Greenland firn aquifers detected by ground and airborne radars. *Journal of Geophysical Research: Earth Surface*, 2016JF003869. https://doi.org/10.1002/2016JF003869

Mikkelsen, A. B., Hubbard, A., MacFerrin, M., Box, J. E., Doyle, S. H., Fitzpatrick, A., … Pettersson, R. (2016). Extraordinary runoff from the Greenland ice sheet in 2012 amplified by hypsometry and depleted firn retention. *The Cryosphere*, *10*(3), 1147–1159. https://doi.org/10.5194/tc-10-1147-2016

Morlighem, M., Williams, C. N., Rignot, E., An, L., Arndt, J. E., Bamber, J. L., … Zinglersen, K. B. (2017). BedMachine v3: Complete Bed Topography and Ocean Bathymetry Mapping of Greenland From Multibeam Echo Sounding Combined With Mass Conservation. *Geophysical Research Letters*, 2017GL074954. https://doi.org/10.1002/2017GL074954

Mosley-Thompson, E., McConnell, J. R., Bales, R. C., Li, Z., Lin, P.-N., Steffen, K., … Bathke, D. (2001). Local to regional-scale variability of annual net accumulation on the Greenland ice sheet from PARCA cores. *Journal of Geophysical Research: Atmospheres*, *106*(D24), 33839–33851. https://doi.org/10.1029/2001JD900067

Mouginot, J., Rignot, E., Scheuchl, B., Fenty, I., Khazendar, A., Morlighem, M., … Paden, J. (2015). Fast retreat of Zachariæ Isstrøm, northeast Greenland. *Science*, aac7111. https://doi.org/10.1126/science.aac7111

Müller, F. (1962). Zonation in the Accumulation Area of the Glaciers of Axel Heiberg, N.W.T., Canada. *Journal of Glaciology*, *4*(33), 302–311.

Munneke, P. K., M. Ligtenberg, S. R., van den Broeke, M. R., van Angelen, J. H., & Forster, R. R. (2014). Explaining the presence of perennial liquid water bodies in the firn of the Greenland Ice Sheet. *Geophysical Research Letters*, *41*(2), 476–483. https://doi.org/10.1002/2013GL058389

Nghiem, S. V., Hall, D. K., Mote, T. L., Tedesco, M., Albert, M. R., Keegan, K., … Neumann, G. (2012). The extreme melt across the Greenland ice sheet in 2012. *Geophysical Research Letters*, *39*(20), L20502. https://doi.org/10.1029/2012GL053611

Noël, B., van de Berg, W. J., van Meijgaard, E., Kuipers Munneke, P., van de Wal, R. S. W., & van den Broeke, M. R. (2015). Evaluation of the updated regional climate model RACMO2.3: summer snowfall impact on the Greenland Ice Sheet. *The Cryosphere*, *9*(5), 1831–1844. https://doi.org/10.5194/tc-9-1831-2015

Pfeffer, W. T., & Humphrey, N. F. (1996). Determination of timing and location of water movement and ice-layer formation by temperature measurements in sub-freezing snow. *Journal of Glaciology*, *42*(141), 292–304.

Pfeffer, W. T., & Humphrey, N. F. (1998). Formation of ice layers by infiltration and refreezing of meltwater. *Annals of Glaciology*, *26*, 83–91.

Pfeffer, W. Tad, Meier, M. F., & Illangasekare, T. H. (1991). Retention of Greenland runoff by refreezing: Implications for projected future sea level change. *Journal of Geophysical Research*, *96*(C12), 22117–22,124. https://doi.org/10.1029/91JC02502

Poinar, K., Joughin, I., Lilien, D., Brucker, L., Kehrl, L., & Nowicki, S. (2017). Drainage of Southeast Greenland Firn Aquifer Water through Crevasses to the Bed. *Frontiers in Earth Science*, *5*. https://doi.org/10.3389/feart.2017.00005

Price, S. F., Payne, A. J., Howat, I. M., & Smith, B. E. (2011). Committed sea-level rise for the next century from Greenland ice sheet dynamics during the past decade. *Proceedings of the National Academy of Sciences*, *108*(22), 8978–8983. https://doi.org/10.1073/pnas.1017313108

Rennermalm, A. K., Smith, L. C., Chu, V. W., Box, J. E., Forster, R. R., van den Broeke, M. R., … Moustafa, S. E. (2013). Evidence of meltwater retention within the Greenland ice sheet. *The Cryosphere*, *7*(5), 1433–1445. https://doi.org/10.5194/tc-7-1433-2013

Robin, G. D. Q. (1975). Velocity of radio waves in ice by means of a bore-hole interferometric technique. *Journal of Glaciology*, *15*(73), 151–159. https://doi.org/10.3198/1975JoG15-73-151-159

Roeckner, E., & others. (2003). *The atmospheric general circulation model ECHAM 5. Part I: Model description, Rep. 349, Max Planck Inst. for Meteorol., Hamburg, Germany*.

Scambos, T., Hulbe, C., & Fahnestock, M. (2003). Climate-Induced Ice Shelf Disintegration in the Antarctic Peninsula. In Eugen Domack, A. Levente, A. Burnet, R. Bindschadler, P. Convey, & tthew Kirby (Eds.), *Antarctic Peninsula Climate Variability: Historical and Paleoenvironmental Perspectives* (pp. 79–92). American Geophysical Union. Retrieved from http://onlinelibrary.wiley.com/doi/10.1029/AR079p0079/summary

Schutz, B. E., Zwally, H. J., Shuman, C. A., Hancock, D., & DiMarzio, J. P. (2005). Overview of the ICESat Mission. *Geophysical Research Letters*, *32*(21), n/a–n/a. https://doi.org/10.1029/2005GL024009

Shepherd, A., Ivins, E. R., A, G., Barletta, V. R., Bentley, M. J., Bettadpur, S., … Zwally, H. J. (2012). A Reconciled Estimate of Ice-Sheet Mass Balance. *Science*, *338*(6111), 1183–1189. https://doi.org/10.1126/science.1228102

Smith, L. C., Yang, K., Pitcher, L. H., Overstreet, B. T., Chu, V. W., Rennermalm, Å. K., … Behar, A. E. (2017). Direct measurements of meltwater runoff on the Greenland ice sheet surface. *Proceedings of the National Academy of Sciences*, *114*(50), E10622–E10631. https://doi.org/10.1073/pnas.1707743114

Sommers, A. N., Rajaram, H., Weber, E. P., MacFerrin, M. J., Colgan, W. T., & Stevens, C. M. (2017). Inferring Firn Permeability from Pneumatic Testing: A Case Study on the Greenland Ice Sheet. *Frontiers in Earth Science*, *5*. https://doi.org/10.3389/feart.2017.00020

Sorge, E. (1935). Glazialogische Ulltersuchungell in Eismitte, in Wissenschaftliche Ergebnisse der DeutscheTl Gramland-Expedition Alfred Wegener 1929 und 1930/1931. *Leipzig: F. A. Brockhaus*, *Vol. 3*, 270 p.

Sorge, E. (1938). Die Firnschrumpfun in den oberstm Schichten des Groenlaendischen Inlandeises. *International Geodetic and Geophysical Union, Association of Scientific Hydrology*, *Bulletin 23*, 275–331.

Steffen, K., Nghiem, S. V., Huff, R., & Neumann, G. (2004). The melt anomaly of 2002 on the Greenland Ice Sheet from active and passive microwave satellite observations. *Geophysical Research Letters*, *31*(20), L20402. https://doi.org/10.1029/2004GL020444

Steffen, Konrad, & Box, J. (2001). Surface climatology of the Greenland Ice Sheet: Greenland Climate Network 1995–1999. *Journal of Geophysical Research: Atmospheres*, *106*(D24), 33951–33964. https://doi.org/10.1029/2001JD900161

Tedesco, M., Fettweis, X., Mote, T., Wahr, J., Alexander, P., Box, J. E., & Wouters, B. (2013). Evidence and analysis of 2012 Greenland records from spaceborne observations, a

regional climate model and reanalysis data. *The Cryosphere*, *7*(2), 615–630. https://doi.org/10.5194/tc-7-615-2013

Thomas, R. H. (2001). Program for Arctic Regional Climate Assessment (PARCA): Goals, key findings, and future directions. *Journal of Geophysical Research: Atmospheres*, *106*(D24), 33691–33705. https://doi.org/10.1029/2001JD900042

Undén, P., Rontu, L., Järvinen, H., Lynch, P., & Calvo, J. (2002). The HIRLAM model (version 5.2). *Norrköping (Sweden), High Resolution Limited Area Model Scientific Report, 144pp*.

van As, D., Bech Mikkelsen, A., Holtegaard Nielsen, M., Box, J. E., Claesson Liljedahl, L., Lindbäck, K., … Hasholt, B. (2017). Hypsometric amplification and routing moderation of Greenland ice sheet meltwater release. *The Cryosphere*, *11*(3), 1371–1386. https://doi.org/10.5194/tc-11-1371-2017

van As, D., Hubbard, A. L., Hasholt, B., Mikkelsen, A. B., van den Broeke, M. R., & Fausto, R. S. (2012). Large surface meltwater discharge from the Kangerlussuaq sector of the Greenland ice sheet during the record-warm year 2010 explained by detailed energy balance observations. *The Cryosphere*, *6*(1), 199–209. https://doi.org/10.5194/tc-6-199-2012

van de Wal, R. S. W., Boot, W., Smeets, C. J. P. P., Snellen, H., van den Broeke, M. R., & Oerlemans, J. (2012). Twenty-one years of mass balance observations along the K-transect, West Greenland. *Earth System Science Data*, *4*(1), 31–35. https://doi.org/10.5194/essd-4-31-2012

van den Broeke, M., Bamber, J., Ettema, J., Rignot, E., Schrama, E., van de Berg, W. J., … Wouters, B. (2009). Partitioning Recent Greenland Mass Loss. *Science*, *326*(5955), 984–986. https://doi.org/10.1126/science.1178176

van den Broeke, M. R., Enderlin, E. M., Howat, I. M., Kuipers Munneke, P., Noël, B. P. Y., van de Berg, W. J., … Wouters, B. (2016). On the recent contribution of the Greenland ice sheet to sea level change. *The Cryosphere*, *10*(5), 1933–1946. https://doi.org/10.5194/tc-10-1933-2016

Vionnet, V., Brun, E., Morin, S., Boone, A., Faroux, S., Le Moigne, P., … Willemet, J.-M. (2012). The detailed snowpack scheme Crocus and its implementation in SURFEX v7.2. *Geosci. Model Dev.*, *5*(3), 773–791. https://doi.org/10.5194/gmd-5-773-2012

Watanabe, M., Suzuki, T., O'ishi, R., Komuro, Y., Watanabe, S., Emori, S., … Kimoto, M. (2010). Improved Climate Simulation by MIROC5: Mean States, Variability, and Climate Sensitivity. *Journal of Climate*, *23*(23), 6312–6335. https://doi.org/10.1175/2010JCLI3679.1

Zwally, H. J., Jun, L. I., Brenner, A. C., Beckley, M., Cornejo, H. G., Dimarzio, J., … Wang, W. (2011). Greenland ice sheet mass balance: distribution of increased mass loss with climate warming; 200307 versus 19922002. *Journal of Glaciology*, *57*(201), 88–102. https://doi.org/10.3189/002214311795306682

APPENDIX A

Table A1 | Curve fit values for depth-dependent roll-correction functions in Equations (10) – (12).

	A(y) parameters Equation (11)		C(y) parameters Equation (12)						
Track Name	R	S	T	U	V	Roll or Curve	Max Roll /Curve (°)	Mean A (top 20m)	Mean C (top 20m)
20100507_01_008_010	-0.04885	-0.0309	4.216424	-0.00999	-4.95585	Roll	2.1764	-0.036506	-1.1318066
20100507_04_070_070	-0.00433	-11.9735	5.39853	-0.00959	-7.41829	Roll	3.5974	-5.37E-05	-2.5033039
20100508_01_084_084	-0.00493	-0.14438	4.249206	-0.01557	-6.00111	Roll	15.1497	-0.001631	-2.3466957
20100508_01_114_115	-0.07664	0	5.252223	-0.00852	-6.96869	Roll	1.0629	-0.076638	-2.1375163
20100510_01_034_041	-0.00529	-0.07523	4.316194	-0.01195	-6.08658	Roll	22.5495	-0.00275	-2.245077
20100512_04_073_074	-0.03448	-0.05625	4.7209	-0.01128	-6.30526	Roll	1.8218	-0.020774	-2.0762382
20100513_01_001_002	-0.30269	-0.00325	4.412374	-0.01059	-5.7181	Roll	1.4889	-0.293124	-1.7393003
20100514_01_066_067	-0.00451	-0.01765	5.021151	-0.00961	-7.75785	Roll	19.9813	-0.003805	-3.1874317
20100514_01_077_078	-0.01355	-0.0118	3.819582	-0.01823	-6.56417	Roll	10.8801	-0.012076	-3.360025
20100514_02_001_003	-0.00996	-0.05496	4.436948	-0.01064	-6.99338	Roll	2.3894	-0.006063	-2.9943162
20100514_02_009_010	-0.04116	-0.00335	3.846071	-0.0163	-6.29025	Roll	0.873	-0.039819	-3.0052163
20100514_02_012_015	-0.00466	-0.22434	5.411224	-0.00852	-7.81823	Roll	11.9567	-0.001048	-2.8406508
20100514_02_035_039	-0.00712	-0.08025	4.146821	-0.0161	-6.19774	Roll	20.7993	-0.003567	-2.6491156
20100515_01_007_009	-0.00437	-0.4408	4.533567	-0.01308	-6.61723	Roll	6.5476	-0.000518	-2.6252809
20100517_01_023_026	-0.00669	-0.30144	5.221713	-0.00801	-7.73468	Roll	17.3458	-0.001138	-2.9075126
20100517_01_037_039	-0.00547	-0.32644	9.641602	-0.00356	-12.3256	Roll	16.6403	-0.000863	-3.0177201
20100517_01_053_053	-0.00655	-0.10288	5.117333	-0.00984	-7.52987	Roll	17.7316	-0.002796	-2.8823341
20100517_02_001_002	-0.03232	-0.07809	3.784542	-0.02358	-5.65873	Roll	4.0089	-0.016442	-2.6372405
20100519_01_005_005	-0.00688	-0.12192	3.659794	-0.02121	-5.36611	Roll	21.2027	-0.002599	-2.3800209
20100519_01_036_036	-0.00012	-25.9656	4.499912	-0.0124	-6.84351	Roll	1.0087	-1.36E-06	-2.8554861
20100519_01_048_050	-0.09557	-0.00091	3.798489	-0.01748	-6.07307	Roll	1.8761	-0.094714	-2.8642345
20100519_01_057_058	-0.03765	-0.27767	4.199483	-0.01359	-6.54536	Roll	0.7586	-0.006932	-2.8653347
20100519_01_069_069	-0.00811	-0.05628	6.603591	-0.00741	-8.9038	Roll	14.2404	-0.004887	-2.7638088
20100519_01_072_072	-0.02715	-0.00909	4.242225	-0.01951	-6.44232	Roll	8.2369	-0.024835	-2.9261084
20100520_02_063_063	-0.22599	-0.56993	3.841627	-0.02156	-5.85648	Roll	1.3747	-0.021041	-2.7319508
20100521_02_031_031	-0.10101	-0.01236	4.320098	-0.01476	-6.49464	Roll	3.7419	-0.089555	-2.7506105
20100525_01_051_056	-0.11612	-0.43992	4.154679	-0.01727	-6.58645	Roll	1.6461	-0.013798	-3.0698346
20100525_02_005_008	-0.00079	-0.6369	3.671193	-0.01913	-6.00676	Roll	4.9814	-6.59E-05	-2.9529502
20100525_02_013_015	-5.8E-05	-28.1295	3.805501	-0.01787	-6.11531	Roll	3.0253	-6.8E-07	-2.9123196
20100525_02_030_033	-0.00863	-0.15387	3.72509	-0.01906	-6.04611	Roll	13.8448	-0.002707	-2.9455868
20100526_01_055_059	-0.01779	-0.01253	3.998362	-0.0168	-6.28301	Roll	2.9461	-0.015743	-2.8837802
20100526_01_077_078	-0.01069	-0.10441	4.074252	-0.01321	-6.99781	Roll	15.259	-0.004521	-3.4148494
20100526_01_080_081	-0.0049	-0.23767	2.044298	-0.02046	-6.33236	Roll	3.3013	-0.001044	-4.6527496
20110329_01_003_004	-0.01359	-0.01565	3.47894	-0.02836	-6.50539	Roll	4.0755	-0.011677	-3.8458383

20110329_01_013_018	-0.006	-0.26064	3.701997	-0.02309	-6.83364	Roll	8.0725	-0.001172	-3.8647865
20110329_01_021_021	-0.00736	-0.04206	3.927621	-0.01429	-7.45123	Roll	17.7273	-0.004992	-4.0322808
20110329_01_033_034	-0.00052	-30.0293	4.095587	-0.01549	-7.71684	Roll	7.8777	-6.1E-06	-4.1919539
20110329_04_001_002	-0.13542	-0.10174	4.54944	-0.01154	-7.99873	Roll	2.0524	-0.058282	-3.9337265
20110329_05_001_002	-0.00332	-26.837	4.185993	-0.01179	-7.82843	Roll	1.7417	-3.86E-05	-4.096994
20110331_01_006_011	-5.8E-05	-22.329	3.936671	-0.01906	-7.05316	Roll	1.48	-6.8E-07	-3.776498
20110331_01_014_021	-0.04896	-0.2161	4.156666	-0.01816	-7.27822	Roll	1.1463	-0.011393	-3.7891124
20110331_01_043_044	-0.02523	-0.00724	4.257931	-0.01591	-7.57973	Roll	10.0099	-0.023501	-3.9293924
20110406_01_087_087	-0.00801	-0.01768	4.620703	-0.01411	-7.50552	Roll	5.6331	-0.00675	-3.4765303
20110406_01_108_112	-0.0063	-0.02396	5.99056	-0.00609	-9.46022	Roll	16.3948	-0.005011	-3.8182894
20110406_01_122_124	-0.00444	-0.07093	10.87673	-0.0035	-14.1533	Roll	15.8982	-0.002385	-3.6466527
20110406_01_144_146	-0.00659	-0.07404	5.379983	-0.00974	-8.21549	Roll	19.5583	-0.003453	-3.3244898
20110407_01_009_013	-0.00657	-0.04768	4.172338	-0.00921	-7.56953	Roll	17.6983	-0.004246	-3.7571369
20110407_01_094_094	-5.8E-05	-28.2279	5.30612	-0.01046	-8.40887	Roll	6.457	-6.8E-07	-3.6183968
20110407_01_097_097	-0.06582	-3.56744	4.204564	-0.01633	-7.05516	Roll	2.6284	-0.001352	-3.4650672
20110407_01_127_127	-0.06201	-0.04589	3.619297	-0.01907	-6.58035	Roll	1.357	-0.040692	-3.5681567
20110407_01_134_135	-0.08115	-5.19817	3.471674	-0.02203	-6.54415	Roll	2.338	-0.001341	-3.7328095
20110407_01_166_168	-0.00593	-0.05582	7.515302	-0.00431	-10.953	Roll	18.5097	-0.003582	-3.7510733
20110408_01_087_103	-0.00713	-0.03261	8.563363	-0.00504	-11.6372	Roll	17.012	-0.005245	-3.4890328
20110408_01_125_132	-0.00534	-0.0153	4.767682	-0.00873	-8.17258	Roll	15.4004	-0.004605	-3.7957096
20110411_01_116_118	-0.04853	-0.01392	4.784892	-0.00935	-8.01332	Roll	1.8471	-0.042394	-3.6469279
20110412_01_007_010	-0.0293	-5.80438	4.259187	-0.01164	-7.34233	Roll	1.9529	-0.000459	-3.5401816
20110412_01_158_160	-5.8E-05	-27.9238	4.61105	-0.0124	-7.59127	Roll	2.0313	-6.8E-07	-3.5047392
20110414_01_004_007	-0.0519	-0.08726	4.365974	-0.01204	-7.36999	Roll	2.5211	-0.024698	-3.487231
20110414_01_142_144	-5.8E-05	-26.6826	4.393675	-0.0139	-6.91463	Roll	1.7648	-6.8E-07	-3.0757754
20110416_01_041_042	-0.00431	-0.15237	6.813954	-0.0063	-10.0607	Roll	16.9362	-0.001364	-3.656468
20110416_01_053_055	-0.00504	-0.19369	8.505048	-0.00352	-12.3822	Roll	17.0658	-0.001296	-4.1680863
20110418_01_016_017	-0.00174	-29.062	6.390439	-0.00612	-9.69043	Roll	3.1305	-2.02E-05	-3.6734077
20110418_01_173_175	-0.01033	-0.43573	4.852443	-0.01	-8.09498	Roll	3.3061	-0.001239	-3.6947957
20110419_01_008_010	-0.12178	-0.03625	5.325	-0.00816	-8.35918	Roll	2.2044	-0.08681	-3.4436979
20110422_01_005_006	-0.02442	-0.05247	6.350545	-0.00718	-9.31198	Roll	2.8919	-0.015174	-3.3938234
20110422_02_001_006	-5.8E-05	-28.1932	5.443648	-0.01028	-8.29145	Roll	3.247	-6.8E-07	-3.3683881
20110422_02_070_076	-5.8E-05	-27.1541	7.650631	-0.00531	-10.9617	Roll	3.72	-6.8E-07	-3.7014618
20110423_01_033_033	-0.41288	-0.00457	4.040601	-0.01564	-7.30511	Roll	1.4919	-0.394667	-3.8323321
20110423_01_039_040	-0.05284	0	5.880997	-0.00853	-9.02023	Roll	3.3578	-0.052843	-3.6111095
20110423_01_049_049	-5.8E-05	-28.2464	13.63924	-0.00279	-16.9848	Roll	1.9438	-6.8E-07	-3.7174497
20110423_01_063_067	-0.00809	-0.37708	6.292815	-0.00834	-9.3952	Roll	3.994	-0.001113	-3.5964311
20110423_01_072_074	-0.01823	0	4.293836	-0.01663	-7.09255	Roll	3.281	-0.018226	-3.436268
20110423_01_078_080	-0.01152	-0.07512	4.742404	-0.0145	-7.51522	Roll	12.3743	-0.005994	-3.3953499
20110423_01_091_094	-0.00409	-0.05827	6.220036	-0.00722	-9.4092	Roll	10.8255	-0.002424	-3.6149257
20110423_01_098_102	-0.00824	-0.05957	6.274066	-0.00748	-9.29793	Roll	16.1584	-0.004836	-3.4681961
20110423_01_116_119	-0.00806	-0.08964	4.738333	-0.01388	-7.51489	Roll	15.4376	-0.003769	-3.374161
20110423_01_136_138	-0.00489	-0.1014	4.792788	-0.0113	-7.80555	Roll	19.1089	-0.002109	-3.5131239

20110425_01_011_013	-0.03877	-0.07065	4.502021	-0.01287	-7.35758	Roll	3.4341	-0.020857	-3.3853238
20110425_01_129_134	-0.00819	-0.01904	5.018329	-0.01059	-8.01329	Roll	20.3321	-0.006821	-3.4882239
20110425_01_154_157	-0.00764	-0.01235	4.419213	-0.01357	-7.3425	Roll	17.3203	-0.006774	-3.4691548
20110426_01_009_011	-0.04811	0	6.191044	-0.00695	-9.13451	Roll	2.3196	-0.048112	-3.3525895
20110426_01_180_180	-5.8E-05	-28.2466	8.06605	-0.00562	-11.4561	Roll	2.4806	-6.8E-07	-3.8247908
20110429_01_005_005	-5.8E-05	-27.8441	3.567171	-0.02119	-6.3511	Roll	4.8911	-6.8E-07	-3.4400011
20110429_01_123_124	-0.01226	-0.08091	4.436108	-0.01445	-7.49739	Roll	10.9281	-0.006108	-3.6418413
20110429_01_130_131	-0.00318	-0.4951	4.332946	-0.01606	-7.42093	Roll	9.0397	-0.000338	-3.7117763
20110429_01_152_153	-0.00809	-0.42309	4.712586	-0.0137	-7.83385	Roll	7.3434	-0.000998	-3.708537
20110429_01_156_157	-5.8E-05	-28.2466	6.002648	-0.00701	-9.58523	Roll	4.3882	-6.8E-07	-3.9821951
20110502_01_057_061	-5.8E-05	-27.6386	4.452405	-0.01404	-7.51435	Roll	1.644	-6.8E-07	-3.6293463
20110502_01_079_083	-0.06351	-0.14789	3.921165	-0.01833	-6.91159	Roll	1.5134	-0.020601	-3.6255421
20110502_01_087_092	-0.13864	-0.01584	4.138745	-0.01671	-7.19059	Roll	2.5579	-0.118936	-3.6692145
20110502_01_116_121	-0.01942	-0.20007	4.025065	-0.01812	-7.03721	Roll	3.7992	-0.004848	-3.6573327
20110502_01_171_171	-0.00898	-0.08296	3.874146	-0.02013	-6.80587	Roll	6.7385	-0.004408	-3.6130637
20110507_01_123_123	-0.04242	-0.18522	4.020704	-0.01882	-6.96703	Roll	2.6648	-0.011346	-3.6128832
20110509_01_001_001	-0.00488	-0.04437	5.912222	-0.00625	-10.038	Roll	10.0264	-0.003245	-4.4785074
20110509_01_071_072	-0.00693	-0.09767	4.863602	-0.01419	-8.00383	Roll	17.2102	-0.003066	-3.7659812
20110509_01_092_093	-0.01201	-0.09783	3.974156	-0.01444	-7.33452	Roll	9.7151	-0.005308	-3.8799261
20110509_01_101_103	-0.00703	-0.05534	6.281924	-0.00603	-9.67852	Roll	15.3737	-0.004264	-3.7584852
20110509_01_114_119	-0.01444	-0.05761	5.291647	-0.00974	-8.43299	Roll	4.888	-0.008606	-3.6220928
20110509_01_177_177	-0.01325	-0.01742	4.050735	-0.01812	-6.86324	Roll	2.9455	-0.011197	-3.4617868
20110511_01_008_008	-0.50623	-0.08794	4.710285	-0.01431	-7.40856	Roll	0.8388	-0.239722	-3.3091166
20110511_01_054_055	-0.02259	-0.09187	4.837978	-0.0141	-7.70781	Roll	7.5786	-0.010404	-3.4890288
20110511_01_067_079	-0.00823	-0.06847	4.969108	-0.01167	-7.91536	Roll	17.7452	-0.004503	-3.4808683
20110511_01_098_099	-5.8E-05	-28.2466	3.412582	-0.02375	-6.72095	Roll	4.1742	-6.8E-07	-4.0008369
20110511_01_103_103	-0.00768	-0.04144	9.33871	-0.00388	-12.9002	Roll	18.4165	-0.005233	-3.9127598
20110511_01_106_107	-0.00705	-4.26904	3.404339	-0.02337	-6.57873	Roll	5.7838	-0.00013	-3.8554966
20110511_01_121_135	-0.0095	-0.06086	5.937739	-0.00782	-9.22485	Roll	16.8032	-0.005518	-3.7259263
20110511_01_145_156	-0.00603	-0.13196	9.653399	-0.00388	-13.3069	Roll	16.8692	-0.002142	-4.0166574
20110511_01_172_172	-0.18447	-0.16611	3.350962	-0.02263	-6.44998	Roll	1.7948	-0.054262	-3.751244
20110513_01_043_043	-0.00649	-0.11003	3.699879	-0.0171	-6.73801	Roll	14.0038	-0.002645	-3.6014303
20110513_01_061_062	-0.00928	-0.07563	6.850624	-0.00718	-10.0545	Roll	17.1872	-0.004806	-3.6705095
20110513_01_080_081	-5.8E-05	-25.783	4.479234	-0.01338	-7.44554	Roll	7.531	-6.8E-07	-3.5126274
20110513_01_088_089	-0.00815	-0.04754	5.066153	-0.01015	-8.29165	Roll	3.3203	-0.005273	-3.7039328
20110513_01_101_101	-0.02155	-0.09045	4.575289	-0.01264	-7.74817	Roll	3.6304	-0.010024	-3.7026601
20110516_01_009_010	-0.05398	-0.00273	3.876172	-0.01986	-6.91107	Roll	2.5161	-0.052541	-3.7084096
20110516_01_042_044	-0.00482	-0.06144	7.084372	-0.00645	-10.4501	Roll	15.6341	-0.002788	-3.801097
20110516_01_053_055	-0.00821	-0.06165	4.586926	-0.01342	-7.47016	Roll	21.9122	-0.004737	-3.4443631
20110516_01_088_088	-0.00704	-0.09343	4.518558	-0.01579	-7.3767	Roll	6.5845	-0.003208	-3.4986802
20120330_01_018_023	-112.12	-0.03074	3.831138	-0.02306	-11.375	Curve	0.0128	-83.85638	-8.3033727
20120330_01_025_026	-147.706	-0.04526	3.657618	-0.02032	-11.7581	Curve	0.1355	-97.39969	-8.7506739
20120330_01_035_036	-8.4E-05	-13.9988	4.22436	-0.01529	-12.1968	Curve	0.0518	-2.06E-06	-8.5558258

20120330_01_124_125	-123.315	-0.09883	4.203052	-0.01687	-11.8233	Curve	0.1299	-54.21185	-8.2542616
20120404_01_001_001	-68.1779	-0.05732	4.89491	-0.01116	-13.0389	Curve	0.1375	-40.708	-8.6507388
20120411_01_099_101	-80.7233	-0.19863	4.046296	-0.0122	-14.8054	Curve	0.1419	-20.4972	-11.213774
20120412_01_095_095	-119.566	-0.00945	3.086521	-0.02515	-13.2815	Curve	0.0463	-108.9679	-10.853897
20120413_01_006_012	-119.577	-0.01746	6.835168	-0.0065	-15.2098	Curve	0.1463	-100.9816	-8.7992247
20120413_01_135_136	-55.6114	-0.12484	4.551067	-0.01017	-14.0207	Curve	0.2059	-20.70492	-9.901529
20120414_01_005_007	-12.0462	-0.28787	4.748638	-0.00975	-13.585	Curve	0.0215	-2.18869	-9.2698683
20120416_01_004_005	-1748.75	-0.08966	5.144211	-0.00876	-13.9206	Curve	0.023	-818.8614	-9.201108
20120416_02_117_119	-416.378	-0.04199	4.351892	-0.01324	-13.16	Curve	0.0748	-282.2691	-9.3352691
20120417_01_001_002	-82.2406	-0.04708	5.594768	-0.00897	-14.054	Curve	0.1338	-53.40853	-8.9312671
20120417_01_073_075	-340.193	-0.07854	3.918229	-0.01837	-12.6505	Curve	0.045	-172.555	-9.3696238
20120418_01_005_007	-89.4625	-0.0864	4.420988	-0.01238	-13.1192	Curve	0.1465	-42.86639	-9.2018635
20120418_01_129_131	-66.2347	-0.27543	4.724385	-0.00977	-13.4849	Curve	0.0411	-12.52981	-9.192464
20120419_01_011_013	-104.957	-0.07034	4.339804	-0.01431	-12.9168	Curve	0.1298	-56.60558	-9.1415679
20120419_01_137_140	-87.2977	-0.04483	4.256451	-0.01411	-13.1404	Curve	0.1866	-57.77319	-9.4304486
20120420_01_125_132	-81.5728	-0.02686	7.453629	-0.00464	-16.6914	Curve	0.1745	-63.16904	-9.572601
20120421_01_052_052	-46.0107	-0.0217	11413.18	-2.9E-06	-11422.3	Curve	0.1509	-37.35212	-9.4885324
20120421_01_105_105	-105.409	-0.11835	25.90001	-0.00134	-34.4556	Curve	0.1007	-40.83662	-8.8999208
20120421_01_114_114	-54.3238	-0.07766	5.938661	-0.00727	-14.2787	Curve	0.1924	-27.73207	-8.7506045
20120423_01_006_007	-837.753	-0.09233	4.55962	-0.01284	-12.3338	Curve	0.0282	-385.0388	-8.3111151
20120423_01_137_138	-648.017	-0.07416	4.882201	-0.01018	-13.465	Curve	0.023	-339.5418	-9.0468443
20120425_01_066_068	-968.808	-0.02508	5.054704	-0.00961	-13.6819	Curve	0.0176	-762.4683	-9.0820398
20120428_01_006_007	-400.533	-0.06705	4.663912	-0.01039	-13.1549	Curve	0.0467	-221.5319	-8.9424951
20120428_01_125_126	-444.683	-0.06089	5.209856	-0.00809	-14.0036	Curve	0.0253	-258.077	-9.1926729
20120429_01_016_020	-77.6822	-0.01482	6.888757	-0.00564	-15.7236	Curve	0.1733	-67.2525	-9.2081252
20120429_01_041_041	-83.6424	-0.06155	7.500678	-0.00599	-15.8992	Curve	0.1241	-48.28775	-8.8298096
20120429_01_050_050	-46.4658	-0.00343	6.973638	-0.006	-15.686	Curve	0.0882	-44.91132	-9.1135812
20120429_01_066_066	-581.628	-0.01829	3.842022	-0.02259	-12.045	Curve	0.0138	-487.3665	-8.9514649
20120502_01_016_016	-61.5071	-0.10496	12.04492	-0.0029	-21.0246	Curve	0.1915	-25.95623	-9.3216082
20120503_01_027_027	-336.841	0	5.409756	-0.01055	-13.9677	Curve	0.0649	-336.841	-9.089206
20120507_01_059_059	-127.878	-0.03155	7.136492	-0.0069	-15.9822	Curve	0.0482	-94.94596	-9.3153449
20120507_01_079_079	-209.902	-0.03885	3.747569	-0.02121	-12.2837	Curve	0.0161	-146.1898	-9.2276786
20120510_01_038_038	-6947.49	-0.01776	4.568852	-0.01199	-13.2526	Curve	0.0139	-5850.322	-9.1891622
20120510_01_041_041	-178.905	-0.01148	4.129101	-0.01095	-13.2804	Curve	0.1135	-159.9031	-9.5711359
20120510_01_074_074	-77.376	-0.11629	3.415647	-0.02572	-11.644	Curve	0.1381	-30.36195	-8.9714825
20120510_01_086_086	-0.16655	-3.0921	5.017415	-0.01215	-13.6022	Curve	0.0142	-0.005165	-9.1465283
20120510_01_093_093	-61.3373	-0.1156	3.863733	-0.01882	-12.4146	Curve	0.1513	-24.17236	-9.1929839
20120511_01_031_032	-178.176	-0.07069	7.03203	-0.00674	-15.6597	Curve	0.0356	-95.83727	-9.080362
20120511_01_059_059	-69.2265	-0.11888	4.230005	-0.01689	-12.6581	Curve	0.1406	-26.72881	-9.0668747
20120514_01_004_006	-81.7469	-0.01971	5.885721	-0.00826	-14.4374	Curve	0.0095	-67.59901	-9.0110435
20120514_01_035_036	-28.8976	-0.02637	4.871287	-0.00992	-13.9252	Curve	0.2699	-22.47822	-9.5058368
20120514_02_024_025	-6096.04	-0.04339	4.387457	-0.0146	-12.8485	Curve	0.011	-4083.598	-9.0420097
20120515_01_070_070	-77.0649	-0.06315	6.05492	-0.0085	-14.7868	Curve	0.1584	-43.93605	-9.2177251

20120515_01_078_078	-911.254	-0.0195	5.689067	-0.00839	-14.3954	Curve	0.0212	-755.0414	-9.157148
20120515_01_083_083	-175.825	0	4.144617	-0.01885	-12.4242	Curve	0.0294	-175.8253	-8.9692344
20120515_01_091_091	-0.31706	-2.24258	4.876554	-0.01075	-14.1408	Curve	0.0162	-0.01148	-9.7517227
20120516_01_002_002	-18.7196	-0.0773	4.323556	-0.01482	-12.5811	Curve	0.1052	-9.581596	-8.8379138
20120516_01_032_032	-92.9238	0	3.861423	-0.02081	-12.192	Curve	0.0366	-92.92378	-9.0312449
20120516_01_038_038	-42.0157	-0.07538	4.297532	-0.01342	-12.9596	Curve	0.2441	-21.8143	-9.1890888
20120516_01_046_046	-70.7322	-0.08517	4.59288	-0.01479	-13.5388	Curve	0.1755	-34.19153	-9.5614846
20120516_01_050_051	-119.892	0	4.222159	-0.01809	-12.9167	Curve	0.0873	-119.8919	-9.3721353
20120516_01_093_093	-15.7028	-0.21545	4.540768	-0.01205	-13.6977	Curve	0.1712	-3.709832	-9.6614547
20120516_01_115_115	-37.7145	-0.04659	3.953471	-0.02103	-12.1798	Curve	0.1212	-24.59219	-8.9503663
20130402_01_008_008	-0.00622	-0.09257	2.853447	-0.02335	-6.83639	Roll	6.4346	-0.002855	-4.5548866
20130404_01_018_018	-0.01264	0	2.729162	-0.0249	-6.83443	Roll	2.1967	-0.012636	-4.6829504
20130404_01_020_020	-0.00717	-0.10094	3.4116	-0.01665	-7.35888	Roll	18.2142	-0.00311	-4.4559313
20130404_01_074_075	-0.00558	-0.05961	3.146233	-0.02372	-7.07817	Roll	18.3736	-0.003272	-4.5710571
20130404_01_082_083	-0.00435	-0.40245	3.227044	-0.02072	-7.24911	Roll	9.4145	-0.000583	-4.6055655
20130404_01_103_107	-0.00181	-0.00421	3.094967	-0.01464	-7.3393	Roll	14.3272	-0.00174	-4.6553522
20130404_01_113_119	-0.00503	-0.25849	3.479294	-0.01221	-7.82216	Roll	11.4121	-0.001009	-4.7340976
20130404_01_139_145	-0.00552	-0.0962	3.014133	-0.02242	-6.94115	Roll	18.5437	-0.002469	-4.5104978
20130404_01_163_165	-0.00089	-14.9155	2.944002	-0.02878	-6.8022	Roll	4.1385	-2.16E-05	-4.5614512
20130405_01_011_013	-0.00098	-0.08327	2.709934	-0.02257	-6.6932	Roll	5.9099	-0.000481	-4.5108023
20130405_01_165_167	-0.00312	-0.0118	2.899845	-0.01776	-7.02905	Roll	13.8777	-0.002781	-4.5869475
20130406_01_019_020	-0.00918	-0.23901	2.911235	-0.01665	-7.11416	Roll	6.2246	-0.001976	-4.6369375
20130406_01_022_022	-0.00231	-0.11013	2.986331	-0.01989	-7.01378	Roll	16.7099	-0.000942	-4.548484
20130406_01_041_041	-0.00541	-0.02915	3.117237	-0.02082	-7.17881	Roll	7.8157	-0.004101	-4.627394
20130406_01_071_071	-0.00667	-0.11787	3.096493	-0.01857	-7.16772	Roll	7.6724	-0.002592	-4.579747
20130406_01_078_086	-0.00311	-0.31223	2.954299	-0.02216	-6.83449	Roll	10.3014	-0.000524	-4.4463617
20130406_01_146_152	-0.00335	-0.28242	2.931076	-0.01713	-6.9797	Roll	9.6121	-0.00062	-4.4967419
20130408_01_009_021	-0.00403	-0.12904	2.976685	-0.01575	-7.10421	Roll	18.9417	-0.001462	-4.5496821
20130409_01_010_012	-0.00416	-0.09878	2.671095	-0.0238	-6.70974	Roll	7.2204	-0.001829	-4.5827579
20130409_01_131_133	-0.00368	-0.00427	2.88538	-0.01964	-6.98094	Roll	7.8755	-0.003529	-4.593463
20130410_01_014_014	-0.00487	-0.18433	3.151071	-0.01235	-7.44873	Roll	15.1847	-0.00132	-4.6557492
20130410_01_028_031	-0.00489	-0.22094	3.21643	-0.01297	-7.50601	Roll	16.4965	-0.001129	-4.6719005
20130410_01_043_043	-8.4E-05	-13.958	3.561636	-0.01095	-7.98783	Roll	6.8739	-2.06E-06	-4.7884615
20130410_01_045_045	-0.00413	-0.16636	3.020791	-0.01523	-7.34631	Roll	15.9737	-0.001223	-4.7411016
20130410_01_087_088	-0.00458	-0.20602	2.763503	-0.02562	-6.76106	Roll	16.3585	-0.001127	-4.5968328
20130410_01_099_100	-0.00406	-0.34626	3.132023	-0.0192	-7.28126	Roll	15.7535	-0.000623	-4.6790847
20130410_01_126_127	-0.00655	-0.11555	3.29593	-0.0131	-7.51635	Roll	6.1616	-0.002583	-4.6158814
20130411_01_009_010	-0.00356	-0.07257	2.721758	-0.02032	-6.81967	Roll	6.099	-0.00189	-4.5816211
20130411_01_086_087	-0.01033	-0.16683	3.413369	-0.01592	-7.60987	Roll	5.2263	-0.003048	-4.685185
20130411_01_164_166	-0.00469	-0.00999	2.862173	-0.02167	-6.86198	Roll	5.626	-0.00425	-4.5377627
20130415_01_015_017	-0.00948	-0.04392	3.409969	-0.01555	-7.70438	Roll	5.0159	-0.006324	-4.7723579
20130415_03_033_034	-0.00238	-0.39383	3.84551	-0.01295	-8.0785	Roll	7.9091	-0.000325	-4.6893855
20130419_01_004_005	-0.01042	-0.02037	4.232443	-0.01654	-9.43829	Roll	14.0577	-0.008564	-5.8329451

20130420_08_045_048	-0.00085	-0.29356	5.571409	-0.00863	-11.3747	Roll	5.642	-0.000151	-6.2567686
20130423_01_002_003	-0.00489	-0.04022	3.372752	-0.01122	-9.7923	Roll	16.795	-0.003364	-6.7703158
20130423_01_069_069	-0.00084	-0.01783	3.227232	-0.01349	-9.71397	Roll	20.0761	-0.00071	-6.8845678
20130423_01_114_115	-8.4E-05	-12.8012	3.43859	-0.01205	-10.1214	Roll	4.9549	-2.06E-06	-7.0649682
20130423_01_125_125	-0.0088	-0.01043	7.673506	-0.003	-14.9541	Roll	3.3124	-0.007945	-7.5060233
20130423_01_127_127	-8.4E-05	-2.85768	39.16151	-0.0006	-46.3566	Roll	11.5056	-2.7E-06	-7.4304103
20130423_01_130_132	-0.00473	-0.00174	5.131251	-0.00617	-12.1178	Roll	7.271	-0.004652	-7.2899685
20130426_01_006_007	-0.00612	-0.07359	4.465683	-0.01361	-10.0076	Roll	18.1873	-0.003222	-6.0966316
20130426_01_083_084	-0.0206	-0.0099	3.867862	-0.01332	-10.0554	Roll	5.6177	-0.018691	-6.6588025
20130426_01_089_089	-0.00834	-0.04243	11.42695	-0.00261	-17.6078	Roll	10.5275	-0.005634	-6.4732435
20130426_01_091_093	-0.00676	-0.06593	6.000312	-0.00669	-12.2237	Roll	18.6897	-0.00377	-6.6069054
20130426_01_103_109	-0.00776	-0.11405	5.14648	-0.00964	-11.03	Roll	13.2158	-0.003088	-6.348202
20140405_04_023_023	-0.00509	-0.12827	6.124815	-0.00767	-12.4492	Roll	20.1649	-0.001858	-6.7701166
20140405_08_001_001	-0.00485	-0.06752	4.945503	-0.01183	-11.0761	Roll	11.1774	-0.002671	-6.6708903
20140405_11_032_034	-0.18242	-0.25569	5.724923	-0.00785	-11.9433	Roll	0.4893	-0.036926	-6.6443245
20140408_04_001_003	-0.0053	-0.01038	3.284537	-0.01727	-9.44114	Roll	14.8815	-0.004786	-6.6625082
20140408_11_024_026	-0.72953	-0.013	5.925448	-0.00813	-13.05	Roll	0.585	-0.642607	-7.5801394
20140409_03_014_017	-0.00717	-0.14176	4.58289	-0.00988	-11.6619	Roll	18.2212	-0.002418	-7.5024394
20140409_09_002_003	-0.00769	-0.06069	4.370332	-0.01472	-10.6004	Roll	8.0341	-0.004468	-6.8131319
20140409_10_001_001	-0.00454	-0.04661	4.771767	-0.01411	-10.7857	Roll	5.5711	-0.002959	-6.6264281
20140409_10_022_025	-0.00688	-0.01138	5.481604	-0.00696	-12.0436	Roll	12.2236	-0.006158	-6.9254546
20140409_10_033_033	-8.4E-05	-12.5298	10.2132	-0.00271	-17.0491	Roll	2.2058	-2.06E-06	-7.1069371
20140409_10_036_038	-0.006	-0.07503	8.501504	-0.00419	-15.1261	Roll	16.0721	-0.003122	-6.9703153
20140409_10_057_066	-0.00723	-0.09746	4.039024	-0.01666	-10.0087	Roll	16.6885	-0.003206	-6.5721349
20140409_10_081_083	-0.06014	0	3.868035	-0.01778	-9.92465	Roll	2.1812	-0.06014	-6.6679693
20140412_05_002_003	-0.00181	-0.00751	4.097259	-0.01239	-14.6233	Roll	10.4329	-0.001683	-10.993024
20140412_06_001_002	-0.00343	-0.05494	3.333205	-0.01362	-10.1208	Roll	11.1499	-0.002087	-7.2019137
20140412_07_001_001	-0.00642	-0.09079	4.467228	-0.01582	-11.3969	Roll	12.0577	-0.002984	-7.5655283
20140416_01_040_055	-0.00723	-0.05119	7.955889	-0.00494	-17.1873	Roll	16.1144	-0.00454	-9.6110927
20140416_02_001_001	-0.00755	-0.08348	4.489344	-0.01444	-13.2631	Roll	14.0177	-0.003696	-9.3622503
20140416_04_024_027	-8.4E-05	-13.9983	4.405033	-0.012	-13.7004	Roll	3.9628	-2.06E-06	-9.7829449
20140416_05_007_009	-0.00793	-0.07636	4.913052	-0.01057	-14.0092	Roll	9.9099	-0.004087	-9.5795256
20140416_05_035_037	-0.00707	-0.10342	4.806901	-0.00996	-14.0692	Roll	12.9994	-0.003013	-9.7096368
20140419_01_016_017	-0.00626	-0.11112	9.13479	-0.00328	-18.8834	Roll	18.8873	-0.002537	-10.041335
20140419_01_028_028	-0.0042	-0.02408	2392.888	-1.3E-05	-2402.76	Roll	19.7233	-0.003338	-10.175963
20140419_03_034_035	-0.00707	-0.12036	3.782407	-0.01688	-11.7642	Roll	15.9483	-0.002707	-8.5525845
20140419_03_048_048	-0.00912	-0.01825	5.19747	-0.01166	-12.9261	Roll	4.7913	-0.007645	-8.2887737
20140419_03_075_075	-8.4E-05	-13.7892	6623.442	-4.6E-06	-6631.41	Roll	2.053	-2.06E-06	-8.2747425
20140421_01_009_013	-8.4E-05	-13.9145	5.179735	-0.0091	-12.8758	Roll	2.2952	-2.06E-06	-8.1390655
20140421_01_181_181	-0.00686	0	4.110548	-0.01872	-11.7646	Roll	2.6926	-0.006855	-8.3338962
20140424_01_002_004	-8.4E-05	-13.7088	1.872243	-0.02831	-10.0843	Roll	2.7552	-2.05E-06	-8.6531907
20140424_03_046_048	-0.00132	-0.28102	3.146805	-0.01976	-10.8037	Roll	2.9738	-0.000245	-8.2026279
20140429_02_052_052	-0.0052	-0.10703	2.326111	-0.03957	-11.9242	Roll	16.5857	-0.002165	-10.314176

20140429_02_076_079	-0.01357	-0.02108	2.3488	-0.03869	-12.0096	Roll	3.9501	-0.011081	-10.371465
20140429_02_090_092	-0.00789	-0.02699	2.491659	-0.0183	-12.3704	Roll	11.9247	-0.006106	-10.282809
20140429_02_110_114	-0.00835	-0.21927	2.231666	-0.04514	-11.9401	Roll	2.3024	-0.001942	-10.467014
20140429_02_160_161	-0.00766	-0.08552	1.969622	-0.04019	-11.9376	Roll	11.8916	-0.003692	-10.581552
20140501_01_023_023	-0.0029	-0.05021	3.893846	-0.02548	-12.3277	Roll	2.9595	-0.001836	-9.274201
20140501_01_026_027	-0.01379	-0.00915	3.755013	-0.01931	-12.7791	Roll	9.7757	-0.012606	-9.6625493
20140501_01_047_052	-0.00646	-0.01433	5.098381	-0.01019	-13.9702	Roll	5.1864	-0.005622	-9.3567014
20140501_01_060_060	-0.00272	-0.00685	3.41145	-0.01627	-12.9012	Roll	2.7306	-0.002546	-9.9879347
20140501_01_062_065	-0.00515	-15.5125	5.071258	-0.01023	-14.0901	Roll	3.8209	-0.000126	-9.5030615
20140501_01_072_073	-0.01115	-0.33396	3.650282	-0.01821	-12.6768	Roll	5.499	-0.00177	-9.6159025
20140501_01_089_091	-0.00295	0	3.65408	-0.01875	-12.6535	Roll	4.6756	-0.002952	-9.604683
20140502_01_003_004	-0.00652	-0.23124	3.297324	-0.02843	-12.1607	Roll	3.9325	-0.001446	-9.6430356
20140505_01_002_002	-8.4E-05	-12.5042	3.889675	-0.01754	-13.4213	Roll	3.093	-2.06E-06	-10.139048
20140505_01_011_014	-0.15187	-0.05205	3.840209	-0.01636	-13.5215	Roll	1.2453	-0.094644	-10.244845
20140505_01_026_027	-0.0574	-0.0942	3.993825	-0.01754	-13.5189	Roll	1.6384	-0.026045	-10.148568
20140505_01_056_060	-8.4E-05	-13.9991	4.237487	-0.01426	-13.9416	Roll	2.1024	-2.06E-06	-10.25329
20140505_01_085_086	-8.4E-05	-13.9991	3.579967	-0.01856	-13.4883	Roll	0.8988	-2.06E-06	-10.496141
20140505_01_089_092	-0.00502	-0.22684	3.285283	-0.01892	-13.3047	Roll	18.2162	-0.001132	-10.568014
20140505_01_095_095	-0.087	-0.00602	4.407244	-0.01326	-14.3254	Roll	1.1058	-0.081979	-10.452609
20140505_02_021_022	-0.02579	-0.03205	3.783047	-0.02853	-12.9871	Roll	1.3219	-0.019063	-10.101254
20140505_02_050_051	-0.00777	-0.27617	3.489664	-0.02433	-13.0258	Roll	12.4973	-0.001466	-10.260396
20140505_02_053_054	-0.03149	-0.08853	3.443552	-0.02186	-13.039	Roll	3.1357	-0.014863	-10.247484
20140507_02_082_083	-0.0075	-0.11943	3.060393	-0.0246	-12.3982	Roll	15.5283	-0.002887	-9.978998
20140507_02_098_100	-0.00843	-0.0562	4.385257	-0.01528	-13.2856	Roll	17.7568	-0.005078	-9.5052935
20140507_02_115_116	-8.4E-05	-13.8996	3.96555	-0.01266	-13.244	Roll	3.8158	-2.06E-06	-9.739559
20140507_02_123_124	-0.00174	-15.8409	3.808701	-0.01836	-12.7361	Roll	2.8055	-4.26E-05	-9.5466116
20140507_02_136_136	-8.4E-05	-13.9952	3.884338	-0.01431	-13.1618	Roll	4.1851	-2.06E-06	-9.7825945
20140507_03_007_008	-0.01412	-0.37148	3.770723	-0.01952	-12.6166	Roll	1.2943	-0.002033	-9.4930704
20140508_01_005_005	-0.0672	-0.30611	3.519112	-0.02555	-13.2	Roll	0.9498	-0.011544	-10.442018
20140508_02_019_020	-0.0606	-0.02198	6.119904	-0.00769	-14.6798	Roll	3.3492	-0.049073	-9.0060855
20140508_03_019_024	-0.00745	-0.07943	3.865001	-0.02032	-13.129	Roll	18.5591	-0.003752	-9.9511462
20140509_01_048_051	-0.0157	-0.10373	5.425108	-0.00639	-16.1427	Roll	3.517	-0.006679	-11.049288
20140509_01_053_053	-0.0076	-0.14415	6.005218	-0.00744	-16.6018	Roll	13.8071	-0.002532	-11.02098
20140509_01_057_059	-0.00742	-0.11974	4.605073	-0.01176	-14.9444	Roll	11.312	-0.002852	-10.839472
20140509_01_072_073	-8.4E-05	-13.9962	3.66166	-0.02	-13.6553	Roll	2.0337	-2.06E-06	-10.635511
20140509_01_075_076	-0.00613	-0.15057	3.590628	-0.01946	-13.5664	Roll	11.2778	-0.001969	-10.590285
20140509_01_081_082	-0.05091	-0.00986	4.437831	-0.01399	-14.5326	Roll	2.2185	-0.046213	-10.659915
20140509_01_101_101	-0.00322	-0.06923	3.654708	-0.02675	-13.2666	Roll	8.8098	-0.001752	-10.43344
20140509_01_103_104	-0.00447	-0.02553	3.933283	-0.02201	-13.499	Roll	4.4792	-0.003506	-10.314858
20140509_01_106_112	-0.01029	-0.08629	3.98139	-0.02059	-13.6072	Roll	15.2905	-0.004935	-10.341548
20140512_01_003_003	-8.4E-05	-13.9962	3.407458	-0.02349	-13.2559	Roll	12.1313	-2.06E-06	-10.534808
20140512_01_027_028	-0.00778	-0.10818	3.450811	-0.02602	-13.752	Roll	18.8668	-0.003213	-11.059125
20140512_01_046_049	-0.00602	-0.10273	3.599652	-0.01984	-14.1411	Roll	19.7714	-0.002578	-11.167957

20140512_01_063_064	-0.01479	-0.00394	3.337224	-0.03131	-13.755	Roll	5.2109	-0.014225	-11.271695
20140512_01_080_083	-0.00912	-0.06501	3.865397	-0.01664	-14.4003	Roll	13.4328	-0.005123	-11.110751
20140512_01_094_095	-0.00655	-0.0167	3.489372	-0.01753	-14.2772	Roll	6.008	-0.005575	-11.332437
20140512_01_101_101	-0.01042	-0.08559	3.549203	-0.02419	-13.8265	Roll	5.8746	-0.005024	-11.010205
20140512_01_107_108	-0.00682	-0.08192	3.407434	-0.02756	-13.7684	Roll	7.6887	-0.003374	-11.146251
20140512_01_113_113	-8.4E-05	-13.3876	3.288796	-0.01682	-14.3062	Roll	1.8541	-2.05E-06	-11.511913
20140512_02_003_004	-0.00902	-0.09638	3.483486	-0.02292	-13.9331	Roll	7.161	-0.004032	-11.136553
20140512_02_008_008	-0.00486	-0.0178	3.512868	-0.02754	-13.714	Roll	4.4633	-0.004089	-11.010139
20140512_02_015_017	-0.0348	-0.00384	3.533454	-0.02342	-13.9073	Roll	2.4144	-0.033504	-11.083582
20140512_02_022_023	-0.00781	-0.10365	3.076913	-0.02837	-13.7049	Roll	5.9492	-0.003325	-11.35426
20140512_02_026_026	-0.00638	-0.3016	3.38216	-0.02363	-14.0261	Roll	7.6186	-0.001111	-11.32871
20140514_01_063_065	-0.08444	-0.01605	3.785941	-0.01904	-14.2417	Roll	4.0432	-0.072264	-11.091256
20140514_02_004_004	-8.4E-05	-13.9916	4.038867	-0.01253	-14.7038	Roll	1.2359	-2.06E-06	-11.13012
20140514_02_020_022	-0.02492	-0.0127	3.841517	-0.01938	-14.1081	Roll	2.3546	-0.022019	-10.921643
20140514_02_031_031	-0.01999	-0.10188	3.070192	-0.03173	-13.7476	Roll	4.182	-0.008613	-11.471484
20140514_02_087_089	-0.02136	-0.07965	3.724795	-0.0232	-13.7102	Roll	3.8666	-0.010749	-10.727609
20140515_02_001_003	-0.00735	-0.10821	3.564687	-0.02243	-13.6	Roll	9.0585	-0.003038	-10.725339
20140515_02_173_175	-0.01458	-0.10284	3.631201	-0.02464	-13.5608	Roll	8.1717	-0.006242	-10.69117
20140516_02_031_034	-0.0066	-0.12992	2277.261	-1.3E-05	-2287.81	Roll	14.7234	-0.002386	-10.836592
20140516_03_001_011	-0.00791	-0.04966	4.512463	-0.01159	-14.9682	Roll	19.4293	-0.005029	-10.939434
20140516_03_013_014	-0.01015	-0.03336	3.650415	-0.02129	-13.8371	Roll	3.9929	-0.007415	-10.862285
20140519_02_002_004	-0.02434	-0.07869	3.727711	-0.02342	-13.5086	Roll	7.3723	-0.012331	-10.52963
20140519_04_012_012	-0.00926	-0.1153	3.546629	-0.02654	-13.9747	Roll	16.671	-0.003658	-11.220009
20140519_04_019_021	-0.006	-0.12291	3.237868	-0.0225	-14.2085	Roll	19.5827	-0.002262	-11.599155
20140519_07_003_003	-0.01307	-0.08535	4.082315	-0.01791	-14.3724	Roll	5.9653	-0.006308	-10.939415
20140519_08_045_046	-0.02153	-0.12074	3.568519	-0.02617	-13.8966	Roll	5.4854	-0.00822	-11.115688
20140519_08_066_069	-0.08086	-1.68058	4.070325	-0.01268	-14.909	Roll	1.1719	-0.003473	-11.312456
20140519_09_001_001	-8.4E-05	-14.0007	2.342387	-0.0281	-14.0658	Roll	4.7792	-2.06E-06	-12.272005

APPENDIX B

List of IceBridge flight lines used in cross-track Excess Melt thresholding:

20100507_04_070_070
20100508_01_114_115
20100510_01_034_041
20100515_01_007_009
20100519_01_036_036
20100519_01_048_050
20100519_01_057_058
20100519_01_069_069
20110329_04_001_002
20110329_05_001_002
20110331_01_043_044
20110412_01_158_160
20110414_01_004_007
20110418_01_016_017
20110418_01_173_175
20110423_01_072_074
20110423_01_078_080
20110425_01_011_013
20110516_01_042_044
20120412_01_095_095
20120414_01_005_007
20120416_01_004_005
20120416_02_117_119
20120417_01_073_075
20120418_01_005_007
20120419_01_011_013
20120423_01_006_007
20130405_01_011_013
20130408_01_009_021
20130409_01_010_012
20130409_01_131_133
20130411_01_009_010
20130411_01_164_166
20130415_01_015_017
20130415_03_033_034
20130423_01_002_003
20140408_04_001_003
20140416_04_024_027
20140416_05_007_009
20140416_05_035_037
20140419_03_034_035
20140419_03_048_048
20140508_02_019_020
20120418_01_005_007
20120419_01_011_013